Développement d'électrolytes à base de liquides ioniques dédiés aux micro-supercondensateurs à base d'oxydes métalliques

Jensheer Shamsudeen Seenath

Université Fédérale
Toulouse Midi-Pyrénées

THÈSE

En vue de l'obtention du
DOCTORAT DE L'UNIVERSITÉ DE TOULOUSE

Délivré par l'Université Toulouse 3 - Paul Sabatier

Cotutelle internationale: Université de Montréal (UdeM)

Présentée et soutenue par

Jensheer SHAMSUDEEN SEENATH

Le 16 juin 2023

Développement de nouveaux électrolytes liquides ioniques pour microsupercondensateurs à base d'oxydes métalliques

---

Ecole doctorale : **SDM - SCIENCES DE LA MATIERE - Toulouse**

Spécialité : **Sciences et Génie des Matériaux**

Unité de recherche :
LAAS - Laboratoire d'Analyse et d'Architecture des Systèmes

Thèse dirigée par
David PECH et Prof. Dominic Rochefort

Jury

M. Said SADKI, Rapporteur
Mme Mérièm ANOUTI, Rapporteure
M. Patrice SIMON, Examinateur
M. Daniel GUAY, Examinateur
Mme Ana TAVARES, Examinatrice
M. David PECH, Directeur de thèse
M. Dominic ROCHEFORT, Co-directeur de thèse
M. Jean LE BIDEAU, Président

Résumé

Avec le développement des systèmes électroniques embarqués se pose la question de la miniaturisation des dispositifs de stockage d'énergie. De nos jours, cette fonction est principalement assurée par des micro-batteries. Ces composants possèdent cependant une faible puissance disponible, une durée de vie limitée et un domaine de fonctionnement en température restreint. Les "micro-supercondensateurs" sur puce permettraient de s'affranchir de ces limitations, mais ils ne sont aujourd'hui qu'au stade de la recherche universitaire avec des densités d'énergie bien inférieures à celles des micro-batteries. L'énergie et la puissance stockées dans un supercondensateur sont proportionnelles au carré de la fenêtre de potentiel, qui dépend elle-même de la stabilité électrochimique de l'électrolyte utilisé. L'électrolyte joue ainsi un rôle prépondérant sur les propriétés des supercondensateurs (tension, gamme de température, courant de fuite, durée de vie…).

Cette thèse vise à développer des liquides ioniques protiques et aprotiques dédiés aux micro-supercondensateurs pseudocapacitifs à base d'oxydes métalliques (RuO_2, MnO_2). Les électrolytes à base de liquides ioniques présentent des propriétés intéressantes, notamment une faible pression de vapeur saturante, une stabilité aux hautes températures, ainsi qu'une large fenêtre de potentiel. Ils contribuent ainsi à améliorer la densité d'énergie surfaciques, principal problème rencontré par les micro-supercondensateurs actuels. Les liquides ioniques étudiés ont été conçus sur la base de leurs structures et leurs propriétés physico-chimiques. Des caractérisations électrochimiques ont été réalisées avec des micro-supercondensateurs à base d'oxyde de ruthénium et d'oxyde de manganèse. De très bonnes performances ont été obtenus en utilisant des collecteurs de courant poreux à grande surface spécifique. Les électrolytes liquides constituant cependant un verrou technologique à la réalisation de micro-supercondensateurs fonctionnels compatible avec les procédés de microfabrication, des ionogels composés d'une matrice solide dans laquelle a été confinée le liquide ionique ont également été réalisés.

Mots-clés: RuO_2, MnO_2, Liquides ioniques protiques et aprotiques, Pseudocapacitance, IoT, Micro-supercondensateur poreux, Densité d'énergie, Ionogel

Abstract

The rising growth of smart and autonomous microelectronic devices in the IoT (Internet of Things) era urges the development of advanced microscale energy sources with tailor-made features and customized energy/power requirements. Micro-supercapacitors (MSCs) emerged as potential energy storage devices complementing micro-batteries to power ubiquitous sensor networks needed to foster the development of IoT. However, the low cell voltage and low energy density remain major bottleneck that prevents their application at a large scale in real devices. To mitigate this issue, several studies have been devoted to the engineering of MSC electrode materials and structural architecting of current collectors to enhance the surface area and areal energy density by considering the limited available footprint area. This, however, has associated challenges such as a complex synthesis route, poor interfacial and mechanical stability of the electrode, and electrolyte compatibility issues, among others. Another key challenge to solve for reaching high energy density values in MSCs is the limited electrochemical stability window (ESW) of the electrolytes used as energy stored is directly related to the square of the cell voltage. The electrolytes play a major role in deciding the ESW and liquid-state electrolytes commonly used are troublesome for the microfabrication process due to leakage, evaporation, and safety issues. Therefore, it's imperative to develop alternative electrolytes including solid-state electrolytes reconcilable to the target application of MSCs.

This thesis aims at developing novel ionic-liquid (IL)-based electrolytes (both protic and aprotic) suitable for pseudocapacitive metal oxide (e.g., RuO_2, MnO_2)-based micro-supercapacitors (MSCs). IL-based electrolytes exhibit key properties including low vapor pressure, high temperature stability, low melting point, etc. with a wide ESW and help improve energy density performance, overcoming the major bottleneck faced by current MSCs. During this project, ILs are rationally designed based on their physicochemical properties. The detailed structure-property and electrochemical characterization studies were done using RuO_2 and MnO_2-based MSCs. We demonstrate state-of-the-art performance by developing high surface area porous current collectors with enhanced mass loading and solid-state devices using ionogel electrolytes, enabling their feasible integration with microelectronics to power connected IoT sensor networks.

Keywords: RuO_2, MnO_2, Protic and aprotic ionic liquids, Pseudocapacitance, IoT, Porous micro-supercapacitor, Energy density, Ionogel

Table of contents

List of tables

List of figures

List of abbreviations

1,3-dimethylimidazolium (C1mim)
1-butyl pyrrolidinium
(Pyr$_{4H}$)
1-butyl-3-methylimidazolium
(BMIM^{+})
1-Butyl-3-methylimidazolium
(C4mim)
1-ethyl-3-methylimidazolium
(C2mim)
(EMIM)
1-hexyl-3-methylimidazolium
(C6mim)
1-methyl pyrrolidinium
(Pyr$_{1H}$)
1-methyl-1-propylpyrrolidinium
bis(fluorosulfonyl)imide
(Pyr13FSI)
1-octyl-3-methylimidazolium
(C8mim)
1-pentyl pyrrolidinium
(Pyr$_{5H}$)
1-propyl pyrrolidinium
(Pyr3H)
2-methyl pyridinium
(2-MePy)
acetonitrile
(ACN)
aprotic ionic liquids
(AILs)
area enlargement factor
(AEF)
bis(fluoro sulfonyl)imide
(FSI)
bis(trifluoromethane sulfonyl)imide
(TFSI or NTf2)
butyl-trimethyl ammonium
(BTMA)
characteristic frequency
(f_0)
conductive polymers
(CPs)
conductivity
(σ)
Cyclic voltammetry
(CV)
dicyanamide
(DCA)
Dynamic Hydrogen Bubble Template
(DHBT)
electrochemical capacitors
(ECs)
electrochemical double-layer capacitors
(EDLC)
Electrochemical energy storage
(EES)
electrochemical impedance spectroscopy
(EIS)
electrochemical stability window
(ESW)
Energy Dispersive X-ray Analysis
(EDAX)
equivalent series resistance
(ESR)
Farad
(F)
galvanostatic charge-discharge
(GCD)
gel polymer electrolytes
(GPEs)
hexafluorophosphate
(PF6^{-})
Internet of Things
(IoT)
ionic-liquid
(IL)
linear sweep voltammetry
(LSV)
micro-batteries
(MBs)
Micro-supercapacitors
(MSCs)
N-butyl-N-methyl pyrrolidinium

(PYR_{14}^{+})
N-butyl-N-methylpyrrolidinium
(bmpyr)
N-butylpyridinium
(bpy)
N-diethyl-N-methyl(2-methoxyethyl)ammonium
($DEME^{+}$)
N-methoxyethyl-N methylpyrrolidinium
($PYR1_{(201)}^{+}$)
N-methyl-N-propyl-pyrrolidinium
(PYR_{13}^{+})
open circuit potential
(OCP)
outer charge
(q_o)
poly(vinylidene fluoride)
(PVDF)
polycarbonate
(PC)
polyethylene oxide
(PEO)
Polyoxometalate
(POM)
polyvinyl-alcohol
(PVA)
protic ionic liquids
(PILs)
Pseudocapacitors
(PC)
Ruthenium dioxide
(RuO_2)
ruthenium nitrosyl sulfate
$[Ru(NO)]_2(SO_4)_3$
saturated calomel electrode
(SCE)
scanning electron microscope
(SEM)
Silicotungstic acid
(SiWa)
sodium bis(fluorosulfonyl)imide
(NaFSI)
sodium bis(trifluorosulfonyl)imide
(NaTFSI)
solid polymer electrolytes
(SPEs)
specific capacitance
(C_s)
Supercapacitors
(SCs)
tetraethyl ammonium
(TEA)
tetraethylammonium
Et_4N
tetraethylammonium tetrafluoroborate
($TEABF_4$)
time constant
(τ_0)
total capacitance
(C_T)
total charge
(q_t)
transition metal oxides
(TMOs)
triethylammonium
(TEAH)
triethylammonium bis(trifluoromethanesulfonyl)imide
(TEAH-TFSI)
trifluoroacetate
(tfa^{-})
trifluoromethanesulfonate
$(TfO)^{-}$
trifluromethanesulfonate
(Tf)
Vogel-Fulcher-Tammann
(VFT)
X-ray diffraction
(XRD)
X-ray Photoelectron Spectroscopy
(XPS)

Acknowledgments

First and foremost, I would like to thank my supervisors, Dr. David Pech and Prof. Dominic Rochefort, for their immense support and guidance throughout this cotutelle thesis journey. Their wealth of experience and knowledge in their respective fields has greatly helped me in improving my skills and expertise in electrochemical energy storage systems, for which I am extremely grateful.

I would like to express my sincere gratitude to thesis committee members at UdeM, Prof. Daniel Guay (INRS, Canada), and Prof. Mickäel Dollé (University of Montreal, Canada) for their insightful comments and suggestions during the predoc, seminar, and committee meetings. I would also like to thank the sponsor, Dr. Damien Connétable (CIRIMAT) for the annual Ph.D. interview meetings, as well as Prof. Eric Benoist and Dr. Joël Douin of l'école doctorale Science de la matière at UPS, Toulouse.

I express my gratitude to Prof. Said Sadki and Prof. Mérièm Anouti for agreeing to be rapporteurs and taking time to review my thesis manuscript. I would also like to thank the jury members, Prof. Patrice Simon, Prof. Ana Tavares, Prof. Jean Le Bideau, and Dr. Alain Estève. I truly enjoyed the discussion and the critical comments and feedback from the jury during the defense were very valuable and I believe that would greatly help in improving the quality of my research work.

I would like to thank Dr. David Bourrier (research engineer at LAAS) for his assistance and guidance with the clean room microfabrication process and safety protocols. I appreciate Dr. Éric Dionne at UdeM for helping me with EQCM and DSC measurements, as well as for all of the wonderful conversations, suggestions, and discussions. I would also like to thank Christophe Chabanier & Catalin Harnagea at INRS for their help with XPS and EDAX measurements.

I would like to thank my colleagues at both LAAS and UdeM for creating a conducive and friendly atmosphere to do research. I thank my wonderful former and current LAAS 3D CAP team members, including Botayna, Sai, Lotfi, Sakeb, Hoang, Jean-Yves, and Ankita, for their help and collaboration, as well as for all the inspiring and intellectually stimulating discussions we had on a variety of topics, memorable trips, and sharing a great friendship. I also like to thank all the friendly and kind group members at LEEA, UdeM: Éric, Simon, Yanyu, Alizée, Hassina, Thomas, Aude, and A-Jay for their help and support. In addition, I want to thank Christophe, Camille, Amir, Mylène, and Aurélie for being very friendly and open-minded, as well as for sharing the great office space C115. We always had something to talk about, and I sincerely thank you for helping me with many things, including improving my French.

In addition, I would like to thank the members of LAAS HR and administration (Amandine, Mélodie, Hélène, Stella, Marie-Agnès, and Nathalie) for all their great assistance with the administrative procedures, mission orders, etc.

I would like to acknowledge the generous funding from various funding agencies to help realize this project. Particularly, the European Research Council (ERC, Consolidator Grant, ERC-2017-CoG, Project 771793 3DCAP) and the financial support of the Natural Science and Engineering Council of Canada (NSERC, Project RGPIN-2019-05970). I also like to thank the LAAS-CNRS technology platform, a member of the Renatech network and CQMF-QCAM (Quebec Center for Advanced Materials).

Last but not least, I want to thank my family for their unconditional love, unwavering support, and constant encouragement to help me achieve my goals.

Chapter 1 Introduction & Background

1.1 General Introduction

The rapid progression of smart and autonomous microelectronic devices in the Internet of Things (IoT) era urges the development of advanced microscale energy sources with tailor-made features and customized energy/power requirements [1], [2], [3]. These miniaturized energy storage devices have to be designed to operate for longer periods with less maintenance required. Micro-supercapacitors (MSCs) have come to the foreground as potential energy storage devices to power ubiquitous sensor networks needed to foster the development of IoT [4], [5]. Compared to micro-batteries, MSCs exhibit outstanding power density and long cycle life. However, the low cell voltage and low energy density remain major bottleneck that prevents their application at a large scale in real devices. To mitigate this issue, several studies have been devoted to the engineering of MSC electrode materials and structural architecting of current collectors within the limited available footprint [6]. This approach could offer opportunities to enhance the electrochemically active surface and mass loading of active materials with fast ion diffusion kinetics, leading to high areal energy density performance [7]. Although several efforts have been put forth in this direction, the complex synthesis route, deleterious interfacial and mechanical stability of the electrode, electrolyte compatibility issues, etc. remain an arduous challenge [8].

The low cell voltage is another major issue preventing from achieving high energy density values in MSCs is the limited electrochemical stability window (ESW) of the electrolytes used as energy stored is directly related to the square of the cell voltage [9]. In addition, liquid-state electrolytes currently employed are inappropriate for the microfabrication route as it is prone to evaporation, leakage, and potential safety issues. Hence, a lot of research attention has been given

to developing alternative electrolytes including solid-state electrolytes able to afford large operational windows and help promote the application of on-chip MSCs.

Given the importance of the electrolytes and their impact on the energy density performance in electrochemical energy storage devices, this thesis focuses on the rational design and application of novel ionic-liquid (IL)-based electrolytes for MSCs. The conventional electrolytes such as aqueous-based electrolytes commonly employed for MSCs have the drawbacks of a narrow operational window and poor encapsulation (or ion confinement) due to evaporation and can perform only in the room temperature domain [10], [11]. On the other hand, Ionic-liquids as conducting salts own distinctive merits including low melting point, negligible vapor pressure, and ability to provide a wide electrochemical stability window [12], [13], [14]. By carefully designing the anion and cation groups, it would be possible to harness these properties of ionic liquids to achieve improved charge storage and energy density performance in MSCs [15].

As MSC electrode materials, we chose state-of-the-art pseudocapacitive metal oxides such as RuO_2, and MnO_2 as they can offer enhanced charge storage performance through surface-confined faradaic reactions. The ionic liquid electrolytes are carefully designed according to the electrode material characteristics and their charge storage mechanism. For RuO_2-based electrodes, protons (H^+) ions are inevitable to promote surface charge transfer and redox reactions. Hence, protic ionic liquids (PILs) are designed based on their physicochemical properties. Whereas for MnO_2 electrodes, sodium (Na^+) ions are responsible to bring about efficient charge storage. Therefore, aprotic ionic liquids containing selected Na salts are used for this electrode.

Chapter 1 provides a bibliographic summary starting with a brief introduction and background about energy storage, supercapacitors, and their fundamentals. Next, micro-supercapacitors are introduced in the context of the internet of things and their recent progress and

developments. Afterward, the information on the electrode materials and various electrolyte categories is provided in greater detail. This is followed by information on various material and electrochemical characterization tools to realize this project. In the end, the key objectives of this thesis are presented.

In Chapter 2, we show the pseudocapacitive charge storage of interdigitated RuO_2 MSCs using various protic ionic liquid electrolytes with enlarged cell voltage and their structure-property studies. We also show the results of enhanced proton transport kinetics and optimum charge storage obtained for RuO_2 MSCs while proton conducting additives are included in the PIL. Next, a real MSC device was realized by the use of RuO_2 deposited on interdigitated porous Au current collectors having a high area enlargement factor (AEF) in combination with triethylammonium bis(trifluoromethanesulfonyl)imide (TEAH-TFSI)-based PIL. To demonstrate the potential integration in real on-chip device applications, ionogel-based all-solid-state MSC is developed. The excellent MSC charge storage characteristics such as a higher energy density performance are provided in detail and comparison with state-of-the-art MSC devices.

In Chapter 3, we show the results obtained with a specific group of PILs for RuO_2 MSCs. We chose pyrrolidinium-based cations containing varying alkyl chain lengths and anion groups. The electrochemical results obtained with both flat and porous interdigitated current collector substrates are illustrated. To envision the practical application of RuO_2 MSCs and their subsequent integration with microelectronic devices, ionogel-based solid-state electrolytes were developed.

In Chapter 4, we explored other potential pseudocapacitive electrodes that belong to the metal oxide family for developing MSCs. The active materials investigated are $RuO_xN_yS_z$ and MnO_2 and the suitable aprotic ionic liquids were designed with appropriate ion-conducting salts.

A detailed understanding of the structure-property studies and electrochemical characterization results is given in full detail.

References

[1] N. A. Kyeremateng, T. Brousse, D. Pech, Nat Nanotechnol 2017, 12, 7.

[2] A. Raj, D. Steingart, J. Electrochem. Soc. 2018, 165, B3130.

[3] C. Lethien, J. Le Bideau, T. Brousse, Energ Environ Sci 2019, 12, 96.

[4] C. Shen, S. Xu, Y. Xie, M. Sanghadasa, X. Wang, L. Lin, J. Microelectromech Syst. 2017, 26, 949.

[5] F. Bu, W. W. Zhou, Y. H. Xu, Y. Du, C. Guan, W. Huang, Npj Flexible Electronics 2020, 4, 31.

[6] L. Liu, H. P. Zhao, Y. Lei, Infomat 2019, 1, 74.

[7] P. Zhang, S. Yang, H. Xie, Y. Li, F. Wang, M. Gao, K. Guo, R. Wang, X. Lu, ACS Nano 2022.

[8] Y. Li, S. Xiao, T. Qiu, X. Lang, H. Tan, Y. Wang, Y. Li, Energy Storage Mater 2022, 45, 741.

[9] C. Zhong, Y. Deng, W. Hu, J. Qiao, L. Zhang, J. Zhang, Chem Soc Rev 2015, 44, 7484.

[10] A. Tyagi, K. M. Tripathi, R. K. Gupta, J. Mater. Chem. A 2015, 3, 22507.

[11] N. S. Liu, Y. H. Gao, Small 2017, 13, 1701989.

[12] M. Armand, F. Endres, D. R. MacFarlane, H. Ohno, B. Scrosati, Nat Mater 2009, 8, 621.

[13] J. Le Bideau, L. Viau, A. Vioux, Chem Soc Rev 2011, 40, 907.

[14] X. H. Wang, M. Salari, D. E. Jiang, J. C. Varela, B. Anasori, D. J. Wesolowski, S. Dai, M. W. Grinstaff, Y. Gogotsi, Nat Rev Mater 2020, 5, 787.

[15] T. T. Ye, L. H. Li, Y. Zhang, Adv Funct Mater 2020, 30, 2000077.

1.2 Electrochemical energy storage (EES)

Electrochemical energy storage (EES) technologies play a pivotal role in powering the portable, electronic devices which are imperative to our day-to-day lives. Therefore, high-performing efficient energy-storage systems are urgently required to power hybrid/electric vehicles and various electronic gadgets, also to store energy from intermittent sources such as wind and sun. Although batteries are commonly used for EES, electrochemical capacitors (ECs), also known as supercapacitors exhibit charge-storage properties that can complement batteries, and their usage has increased greatly over the past decade. The charge storage process differs fundamentally in SCs and batteries with different underlying mechanisms. While battery materials can store large amounts of energy (~200 W h kg^{-1}) through diffusion-limited redox reactions occurring in the bulk of the material, which results in slow charging (on the order of hours), capacitive materials store lesser energy (~5 W h kg^{-1}) very rapidly (on the order of seconds) by electrical double layer formation or surface controlled faradaic process. The Ragone plot presented in **Fig. 1.1** depicts the very recent status of specific power versus energy performance of several energy-storage systems. Over the years, energy storage research has been aiming toward pushing ECs and battery performance to the top right part, i.e., the boundary between ECs based on redox-active pseudocapacitive materials and high-rate batteries. In the region marked by the star, the high-energy-density challenge for SCs meets the high-power one for Li-ion batteries. The power and cycle life limitations of batteries stem from the charge-storage mechanism, which involves the transformation of chemical bonds via electrochemical redox reactions (occur on a longer time scale) in the bulk of active materials leading to phase and volume changes. Contrary to batteries, ECs can harvest higher power, resulting in an operation time of tens of seconds to minutes. ECs store the charge via fast, surface-confined processes, which can be electrostatic or faradic in nature. [1], [2], [3] Surface confined energy storage is attributed to only minor, if any, volume change of the

electrode during charge-discharge resulting in a longer cycle life span. These key features together with their power densities, render them potentially useful in applications ranging from small devices for power electronics (power buffer, memory-saving alternating current filtering) to larger modules for automotive applications. [4] Sometimes, coupled with power delivery, energy harvesting can be envisioned, such as braking energy in trams and buses (recharging the EC device via a starter-alternator during vehicle braking steps), which requires high power delivery (discharge time in seconds). Such applications are not feasible with conventional batteries owing to limited power density as well as the low charging rate. ECs are also employed in grid energy storage for power quality and smoothing, power-saving units, and frequency regulation, for which the final device weight can reach several tonnes. Their application also spans the electrical pitch control system of wind turbines and many others.

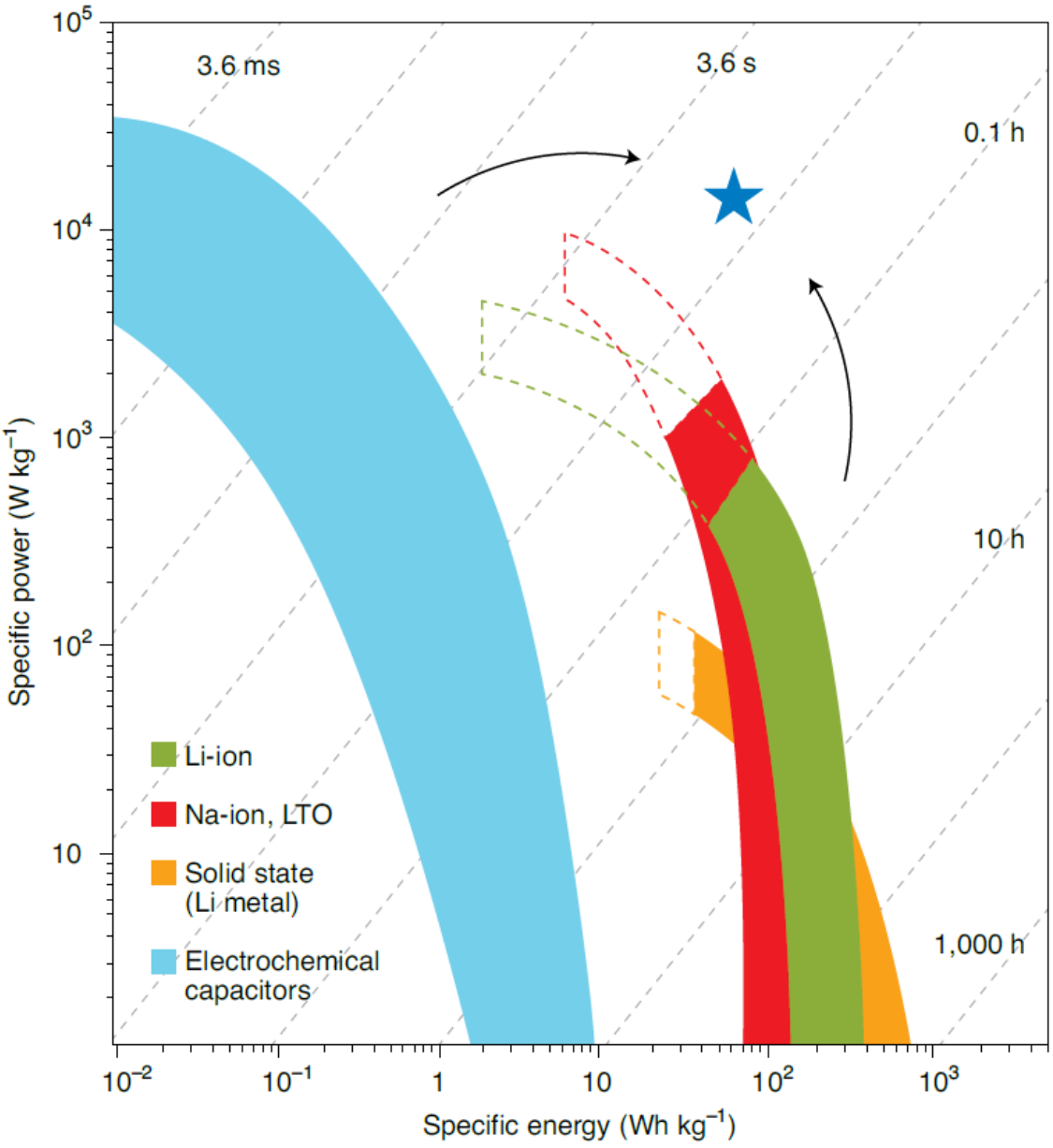

Figure 1.1: Ragone plot showing the specific power vs. energy density of energy storage devices. [4]

1.3 Supercapacitors (SCs)

According to the energy storage mechanism and the nature of electrodes, electrochemical supercapacitors can be classified as electrochemical double-layer capacitors (EDLC), pseudocapacitors, and hybrid capacitors.

1.3.1 Electrochemical Double layer Capacitors (EDLCs)

The electrochemical double-layer capacitor (EDLC) is a well-studied form of SCs where the capacitance originate from the adsorption of anions and cations at the interface between electrode (mostly for porous carbon materials) and electrolyte (**Figure 1.2 a**). The capacitance of the EDLCs depends mostly on the specific surface area and pore-size distribution of the electrode material. The Helmholtz model is the simplest model to describe this process as double-layer capacitance using the equation for a parallel plate capacitor

$$C = \frac{\varepsilon A}{d} \tag{1.1}$$

where C is the double-layer capacitance, ε is the permittivity of the dielectric separating the charges, A is the surface area of the electrode, and d is the distance between the electrode and electrolyte ions. Typically, carbon-based materials such as activated carbon, carbon nanotubes (CNTs), graphene, and carbide-derived carbons show EDLC-type behavior owing to their high specific surface area and good electronic conductivity. [5] The charge/discharge process is purely non-Faradaic; thus, responds immediately to potential changes. The electrochemical signatures of EDLC-based material are shown in **Figure 1.2 b, c.** Cyclic voltammetry (CV) curves are rectangular-box-type in nature, while the galvanostatic charge-discharge (GCD) profile shows a symmetric triangular pattern. The lower energy density values (especially volumetric energy density) are a major bottleneck for the practical implementation of carbon-based SC. Hence, research on EDLCs is focused on the synthesis condition to enhance the specific surface area, surface energy, electrical conductivity, and pore size distribution of the electrode materials.

1.3.2 Pseudocapacitors

The term “pseudocapacitance” was first introduced by Conway to describe the electrochemical signatures of materials that are similar to those of EDLCs, but with different

charge storage mechanisms. [6] In pseudocapacitors, electrochemical reactions are faradic as the energy storage occurs via fast and reversible redox processes at the electrode surface. These reactions happen at an ultra-high rate with similar electrochemical signatures (quasi-rectangular CVs and quasi-triangular GCD curves). [7] The similarities in their electrochemical signatures can be ascribed to the relationship between potential and the amount of charge developed at the electrode/electrolyte interface or within the inner surface due to adsorption/desorption processes. In general, conductive polymers (CPs), some transition metal oxides (TMOs), and their composites are well-known pseudocapacitive electrode materials. [8] The charge storage in pseudocapacitive materials can involve either i) at or near surface-redox reactions; or ii) intercalation-type reactions, which are briefly summarized in the following part.

In surface-redox pseudocapacitors, redox reactions are confined to the electrode surface. As shown in **Figure 1.2 d–f**, the CV and the GCD profiles show a linear dependency in charge storage, which suggests pseudocapacitors store charge via the surface faradic and double-layer mechanism. The materials exhibiting such innate electrochemical features are termed intrinsic pseudocapacitive materials. Various surface-redox pseudocapacitive materials such as transition metal oxides (TMOs) have been investigated since the 1970s. Owing to multiple redox/valence states, TMOs manifest fast and reversible redox reactions at the electrode surface, which makes them potentially store much higher energy than EDLCs.Trasatti and Buzzanca first reported the pseudocapacitance of RuO_2, which is an intrinsic pseudocapacitive material due to the fast and reversible proton-coupled electron transfer mechanism realized by multiple Ru valence states. [9] Likewise, other transition metal oxides such as MnO_2 and Fe_3O_4 are also exhibiting intrinsic (redox) pseudocapacitance. The charge storage mechanism and electrochemical signatures of redox pseudocapacitors are displayed in **Figure 1.2 e,f** with MnO_2 as an example.

The intercalation pseudocapacitor charge storage mechanism is defined by Dunn and Simon, which is common in the nonaqueous electrolyte system. [10], [11]Typically, some layered 2D materials such as TiO_2, Nb_2O_5, and MoO_3 undergo fast and reversible Faradaic charge transfer due to the intercalation of electrolyte ions into the tunnels or layers with no crystallographic phase change with rates approaching or even surpassing the traditional surface redox pseudocapacitive materials. [12], [13] The electrochemical features of the intercalation pseudocapacitance are: the current is linearly proportional to the sweep rate, capacity does not vary significantly with charging time, and peak potentials do not shift considerably with sweep rate (**Figure 1.2 g–i**).

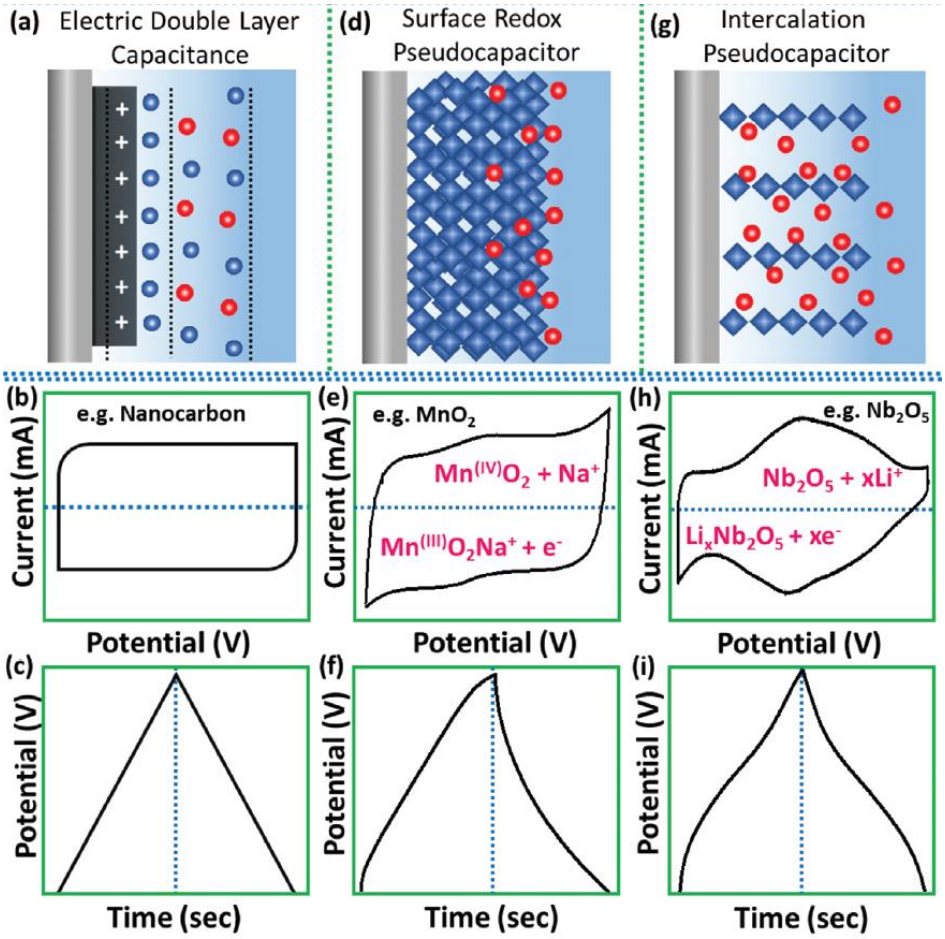

Figure 1.2: The schematic representation of different energy storage mechanisms and corresponding electrochemical signatures (representative shapes of CV and GCD curves): a–c) electrical double layer capacitance, d–f) surface redox capacitance, g–i) intercalation capacitance. [14]

1.3.3 Ruthenium dioxide (RuO_2) active material

Among various transition metal oxides (TMOs), RuO_2 has been widely considered for supercapacitor applications owing to its high conductivity, capacitance, and cycle life. [15] RuO_2 has also been used widely as positive electrode material for Li-ion batteries. [16] The excellent electrocatalytic activity of RuO_2 has also drawn great attention for energy conversion applications. [15] Ruthenium is a less abundant element in the platinum group metals, able to manifest variable oxidation states. The stable solid phase anhydrous oxide of ruthenium has a rutile structure of RuO_2, although it is found to exist in different forms based on water hydration levels. [15] The resistivity of RuO_2 is reported to be around 35 μΩ·cm under ordinary conditions showing high conductivity compared to other transition metal oxides. The superior charge transport properties stem from the delocalized metal-metal states of RuO_2. [17] The work function of RuO_2 is even greater than that of metallic Ru (5.1 eV for RuO_2 and 4.1 eV for Ru) and the molecular orbital (MO) theory and the X-ray photoelectron spectroscopy studies have successfully explained the high isotropic charge transport characteristics of RuO_2, i.e., the existence of a partially filled electronic band just at the Fermi level. [18], [19] The electrochemical features including electrochemical stability over a wide potential range, high reversible oxidation states, long life cycle, and tunable metallic conductivity explain the development of RuO_2 widely for supercapacitor applications. [15], [20] However, some issues remain open like the self-aggregating propensity of the pristine form of RuO_2 and the enhanced charge storage performance by optimal water hydration levels.

Trasatti and Buzzanca accurately theorized that RuO_2 is a hydrous oxide, which can undergo protonation in mildly acidic aqueous solutions. [21] The mechanism of electron charge

transfer in hydrated RuO_2 is mediated by the facile transport of H^+ through the hydrous boundaries of RuO_2 as the Ru valence changes from Ru^{4+} to Ru^{3+} to Ru^{2+} (**Figure 1.3**). Without abundant hydrous boundaries throughout the nanoporous RuO_2 network, proton diffusion becomes sluggish and redox is restricted to the outermost surface, resulting in low charge storage. Hydrated RuO_2 exhibits electrochemical signatures similar to a capacitor, such as multicycle repeatability and box-like voltammograms, despite the faradaic charge-storage mechanism. These features make $RuO_2 \cdot xH_2O$ a unique redox pseudocapacitive material. [22], [23] Although there were efforts to commercialize this material, the high cost of Ru has largely restricted the use of these devices in various applications. Concerning micro-energy storage devices such as micro-supercapacitors, the use of RuO_2 has more relevance as negligible amounts of active materials (typical mass loadings of <0.1 mg cm^{-2}) are required. Besides, replacing the aqueous electrolytes with novel ionic-liquid-based electrolytes compatible with RuO_2 can deliver higher energy density by expanding the voltage window.

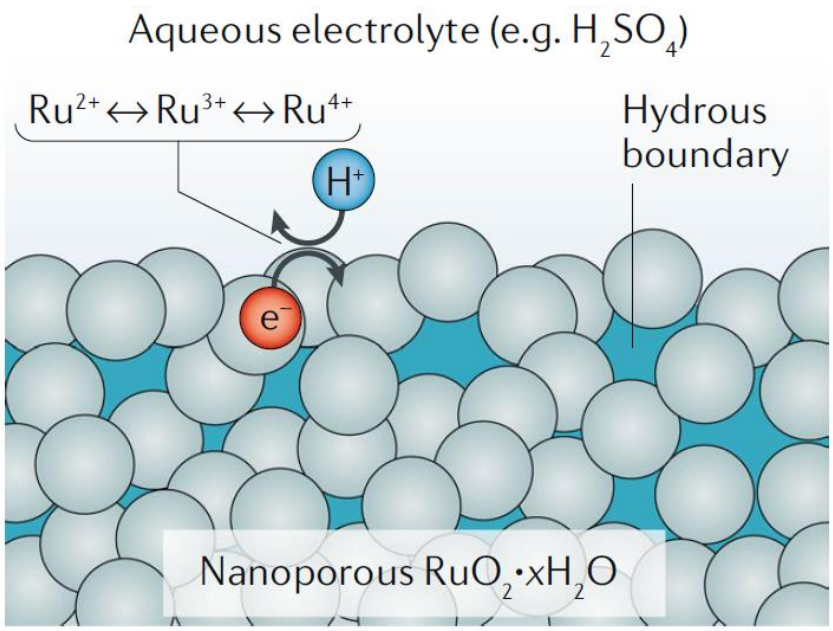

Figure 1.3: The electron charge transfer in hydrated RuO_2. [24]

Ruthenium oxide surface can be charged either by applying suitable electrode potential or by tuning the medium pH as shown in the Pourbaix diagram (**Figure 1.4**). The Pourbaix diagram shown here depicts the behaviour of RuO_2 in aqueous phase and doesn't reflect the material in non-aqueous systems. Trassati *et al.* investigated the variation of pH on RuO_2 charge storage by cyclic voltammetry and developed a model accounting for two types of active sites- namely, inner and outer electrode surfaces were proposed to explain the difference in charge storage mechanism as a function of pH. [25] The outer surfaces are more easily accessible to the electrolyte ions than the inner surfaces which remain partially screened. The protons exchange occurs via the Grotthus mechanism, which is more favored in acidic electrolytes than in alkaline electrolytes due to differences in surface polarity. This is largely the reason why RuO_2-based supercapacitors are operated in aqueous acid-based electrolytes.

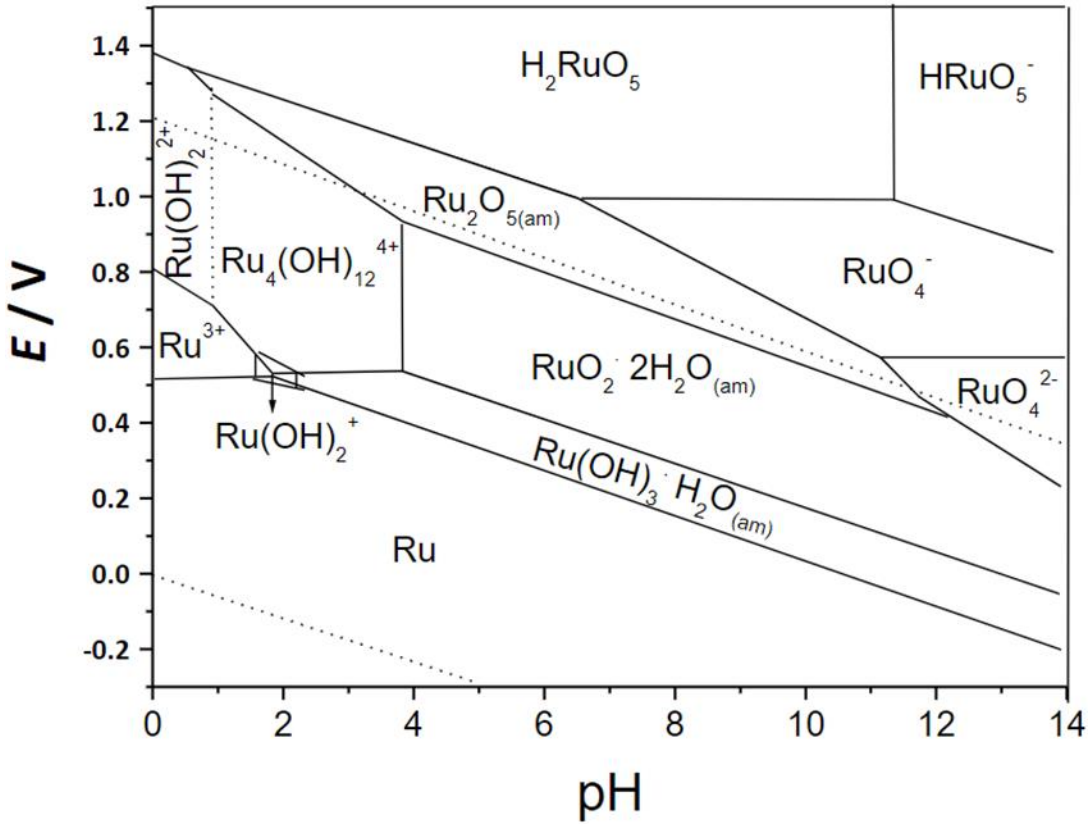

Figure 1.4: Pourbaix diagram of ruthenium indicating different thermodynamically stable phases with varying pH and applied potential vs. SHE. The broken lines correspond to the Hydrogen evolution reaction (bottom) and Oxygen evolution reaction (top) respectively. [26]

1.3.4 Principle parameters of Supercapacitors

A summary of various parameters used for the evaluation of SC performance is provided in the following section. The electrochemical performance of SCs can be well understood using the following key fundamental studies: 1) specific capacitance (using charge stored and voltage window); 2) energy density (determined by specific capacitance and cell voltage of device); 2) power density (from energy density and charge-discharge rate, determined by ions and electron conductivity); 3) long term cycling stability. Other parameters including cost, safety, self-discharge, and temperature dependence are also imperative for practical application. The general relationship between these parameters, the physicochemical properties of each component in a cell, and its effect on SCs performance are shown in **Figure 1.5**.

Capacitance: Capacitance is the material's ability to store electric charge upon applying a voltage across the electrodes, with units of Farad (F).

In a two-electrode SC device, each electrode/electrolyte interfaces represent a capacitor, so it can be treated as two capacitors in series. Hence, the total capacitance (C_T) can be expressed as:

$$\frac{1}{C_T} = \frac{1}{C_p} + \frac{1}{C_n} \tag{1.2}$$

where C_p and C_n are the capacitances of the positive and negative electrodes, respectively. For symmetric SC, since $C_p = C_n$, the total capacitance (C_T) would be half of either electrode's capacitance. In asymmetric SC, C_T is determined by the electrode with the smaller capacitance. Commonly, specific capacitance (Cs), is used to evaluate the electrode capacitance, which can be obtained using the capacitance divided by mass/area/volume of the electrode for gravimetric, areal,

and volumetric capacitance, respectively. Using the Cs value, a reliable comparison can be made between different electrode materials.

Energy density and power density: The stored energy E (Wh), also called the energy density, in a supercapacitor can be obtained from C_T and maximum cell voltage V, which is given below.

$$E = \frac{1}{2} C_T V^2 \tag{1.3}$$

The maximum power density P (W) can be derived using the following equation:

$$P = \frac{1}{4R} V^2 \tag{1.4}$$

where R is the equivalent series resistance (ESR) of the SC.

The energy and power densities normalized by the weight, area, or volume of the device or the electrode provide a basis for comparison between various SC devices in literature as well as from the application prospects. While performance standardized by weight or volume is frequently reported in conventional (macro) SCs, areal performance is crucial for MSCs. Apparently from energy and power density equations, V, C_T, and R represent important variables determining the performance of SCs. An expanded cell voltage window, high C_T, and low ESR are critical for enhancing energy density and power density performance. Since energy and power density is directly proportional to the square of the voltage window, an increase in cell voltage can greatly boost the energy density and power density of a SC as compared to increasing the capacitance or reducing the resistance.

Equivalent series resistance (ESR): In general, ESR is the sum of resistances including the intrinsic resistance of the electrode material, the ionic resistance of the electrolyte, and the contact resistance between the current collector and the electrode. It is an important parameter for determining the SC's power density, a high ESR limits the charging/discharging rate, leading to a low power density. Thus, for some pulse power applications, the ESR value of a SC has more significance than the capacitance value. Normally, the resistances of the bulk electrolyte solution and the electrolyte inside the electrode pores tend to dominate the ESR, especially when nonaqueous electrolytes such as organic, ionic liquid (IL), and solid-state electrolytes are employed in the SCs. Therefore, to achieve superior power density performance, it is important to choose electrolytes with high ionic conductivity. However, there is often a trade-off between the electrolyte's ionic conductivity and the operating potential window. Therefore, to achieve both high energy and power densities for SCs, it is essential to develop electrolytes with a wide operating voltage and a small ESR (or high ion conductivity).

Cycling stability: The cycling stability of SCs is one of the important parameters for evaluating the overall device performance. Generally, long-term galvanostatic charge-discharge (GCD) cycles are conducted to study SC stability. EDLCs normally exhibit high cycling stabilities compared to pseudocapacitors due to continuous redox reactions affecting the electrochemical reversibility and material stability. [27] As a whole, the cycle-life of SCs depends on several factors such as the cell type, the electrode material, the electrolyte, the charge/discharge rate, the operating voltage, and the temperature.

Thermal stability: Thermal stability of SCs is very important for the proper functioning of SCs under adverse environmental conditions. There are reports SCs can operate in a wide temperature range of -30 to 70 °C. [28] Expanding the working temperature range of SCs can further expand the

scope of the SCs. For instance, most space avionics applications require power delivery at temperatures as low as -55 °C. Fuel cell vehicles, on the other hand, may require a higher working temperature. The working temperature can also affect several properties of SCs including the energy and power densities, ESR, cycle life, and self-discharge rate. The performance of temperature-dependent SCs is strongly dependent on the nature of the electrolyte, e.g. the concentration, the type of conducting salt, and the solvent.

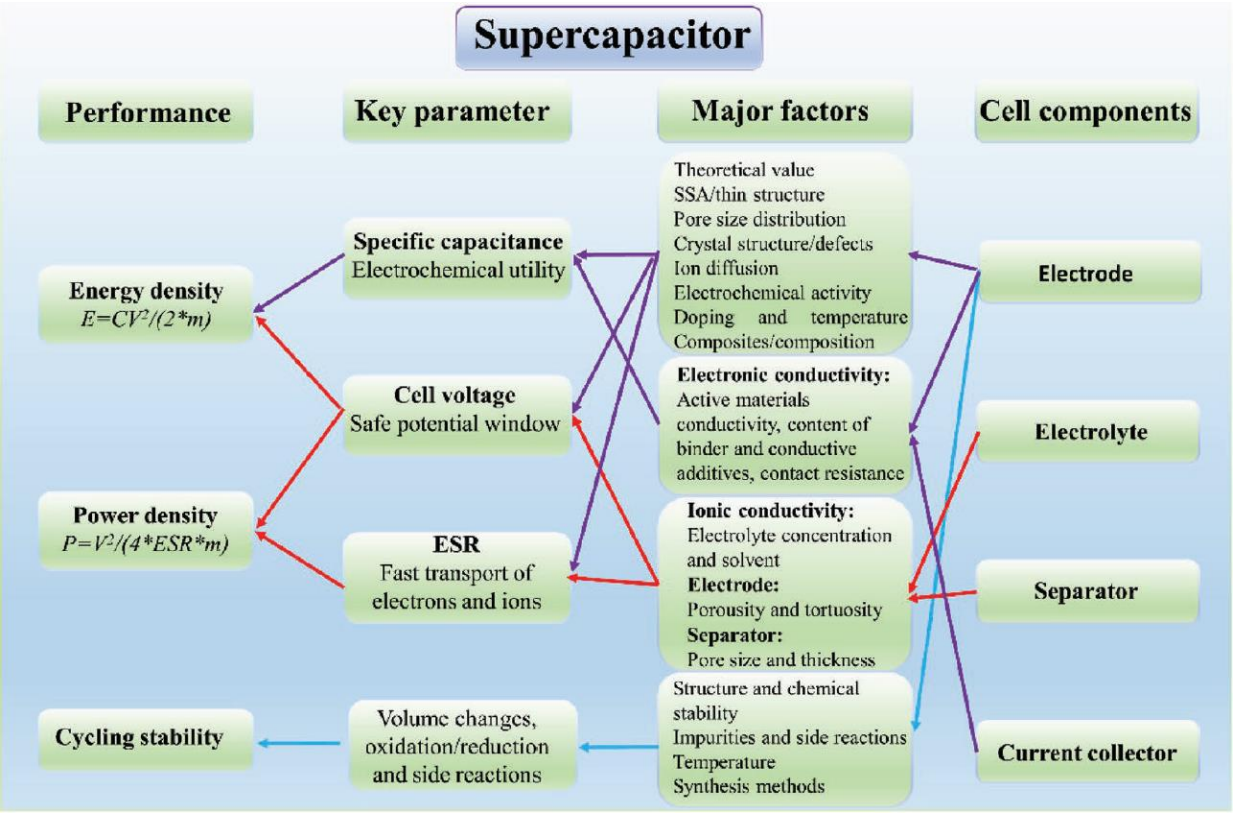

Figure 1.5: Relationship between the SC performance, cell design, and physicochemical properties of each component. [29]

1.4 Micro-Supercapacitors (MSCs)

1.4.1 Context: Internet of Things (IoT)

The industry of the internet of things (IoT), which receive and transfer data over wireless networks, promises to bring about a paradigm shift in the digital world and is expected to develop

further in the future **(Figure 1.6 a)**. [30] The three integral components of IoT networks that are quickly transforming the way people live an advanced lifestyle are i) miniaturized sensors and data analysis tools, ii) a wireless data transfer unit, and iii) a power source. [31], [32], [33] A larger number of microelectronic devices distributed in any place usually need to work without maintenance, so a long-life and high-reliability energy supply with microscale energy-storage devices is necessary. [34] Typically, these networks control hundreds of autonomous microsensors deployed over an area of interest, which independently collect, process, and wirelessly transmit physical local data to a central gateway. It has applications ranging from health (individual management and continuous monitoring of patients), environmental (fire prevention, air, and water quality measurements) or industrial and infrastructure monitoring (buildings, bridges, roads, and even museums), drug delivery (in vivo application) to transportation, wearable personal electronics, and various radiofrequency identification systems. [35], [36], [37] A critical requirement of these applications is energy autonomy. Although power can be extracted by harvesting energy from renewable sources (light, wind, mechanical vibrations, etc.) [35], this requires an energy-storage component to compensate for their intermittency and ensure energetic self-sufficiency over prolonged periods. It is possible only with a large assembly of compact, efficient, miniaturized energy-storage devices for energy harvesting or delivery with high power capabilities.

1.4.2 State-of-the-Art of MSCs

Micro-supercapacitors have been targeted as key enablers for the sustainable and autonomous operation of electronic devices for applications such as wearable gadgets and wireless sensor networks. Although micro-batteries (MBs) can store high energy (1 mW h cm^{-2}) and ensure slow energy delivery, their complex fabrication route, short cycle life (typically <1000 cycles) and fail to deliver the peak power needed for data acquisition and transfer remains a major shortcoming. Also, the device's specific capacity (normalized by weight or volume) decreases with

decreasing size, because of the increasing ratio of passive (e.g., packaging) to active components. To address these challenges, research on the development of micro-supercapacitors (MSCs) has aroused greater interest as they can be integrated directly on Si wafers or printed on flexible substrates with almost unlimited lifetime. [38] It's a rapidly expanding field with high expectations in the design of high-energy and high-power micro-devices to foster the development of the IoT. There are several techniques available to realize MSC and the process normally depends on the substrate used. [38] The power and energy densities of MSCs depend not only on the characteristics of the electrode materials used but also on the structural design and configuration of the components to form a device that can meet the performance requirements. Primarily there are two designs available for MSCs, they are either stacked or interdigitated planar configurations (**Figure 1.6 b**). Due to the inactive gap between the two electrodes in a planar interdigitated configuration, the areal capacitance per electrode polarity being 4 times the total areal capacitance of the device (footprint area). But their in-plane configuration grants the capabilities of easy integration with planar circuits and feasible flexibility when incorporated in flexible and wearable electronics. Whereas a parallel plate or stacked configuration increases the device thickness and is not very desirable for practical on-chip application of MSCs. Moreover, dense stacking of active materials can affect electrolyte wettability, sluggish electrochemical reaction kinetics, and tortuous ion migration pathways, at the expense of power density, rate capability, and lifespan. The MSCs normally have low energy density compared to MBs (<0.1 mW h cm^{-2}). Therefore, a potential solution would be to develop MSCs based on pseudocapacitive charge storage with fast faradaic redox reaction kinetics. The gravimetric performance is insignificant for practical application and the reliable metrics followed are either areal or volumetric energy and power densities derived from capacitance normalized using area or volume by accounting for the electrode thickness (**Figure 1.6 c**). [30] In addition, preparing mechanically stable electrodes with strong adhesion to

the substrate withstanding multiple deformation cycles is challenging for the development of flexible and wearable electronics.

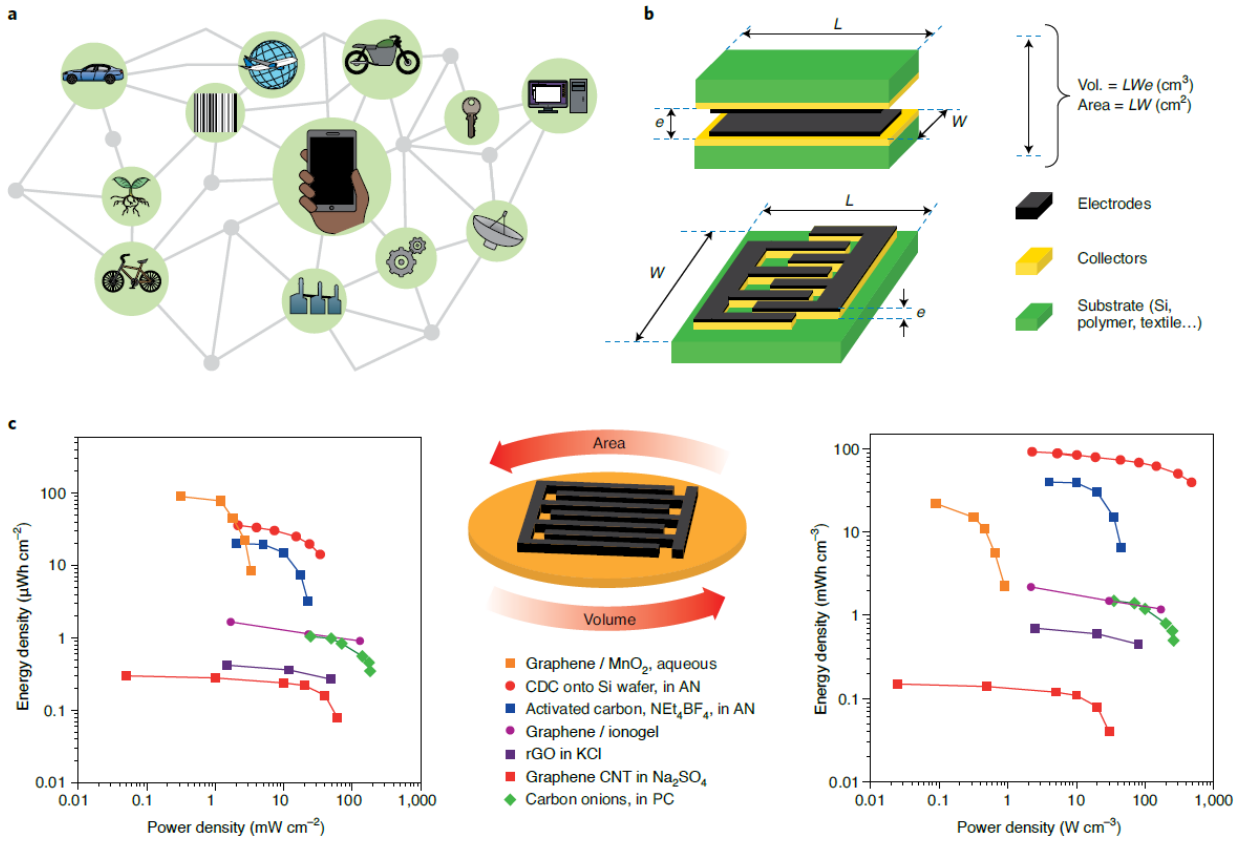

Figure 1.6: Micro-supercapacitors-based technologies. a) Sketch of a connected network of sensors used for the IoT; b) Calculations of the areal and volumetric capacitance of micro-devices with planar (top) or interdigitated (bottom) electrode configuration; c) Example of Ragone plots showing the performance of MSC devices normalized per surface area (left) and volume (right). AN, acetonitrile; CNT, carbon nanotube; rGO, reduced graphene oxide. [4]

The direct integration of MSCs on Si wafers is challenging since fabrication techniques compatible with the semiconductor industry have to be adopted. Dry processing (atomic layer deposition or magnetron sputtering) is preferred over wet routes (such as electrophoretic or electrochemical deposition, screen printing, or serigraphy), but the limited electrode thickness achieved by these techniques results in low areal capacitance. [38] An important breakthrough was achieved by preparing on-chip MSCs by chlorination of TiC films (~5 μm thick) deposited on Si wafer by magnetron sputtering. [39] The partial chlorination of TiC led to the formation of

mechanically stable porous carbon electrodes strongly adhering to the Si surface. Electrode areal capacitance beyond 400 mF cm^{-2} was achieved in an acid electrolyte, making these micro-devices among the best reported for carbon-based MSCs. A limitation of the MSC technology based on nanoporous carbon electrodes is their compatibility issues with the deposition of inorganic solid-state electrolytes owing to the electrode porosity, although solid-state-like electrolytes (gels or ionogels) can be used. [40] Further improvement of the areal capacitance can be achieved by developing a 3D Si surface and preparing structures with a high area enhancement factor (that is, the projected area per footprint area). [30] Unfortunately, the vacuum deposition of pseudocapacitive materials is more challenging and limited by material choice, resulting in capacitance and energy density values falling short of practical needs. [30] Electrochemical deposition is a facile technique to prepare on-chip pseudocapacitive MSCs, but the choice of materials and energy density performance remains a bottleneck.

The mechanical properties including the contact between the electrode material and current-collector play a vital role in the performance and longevity of the cells. Hence, techniques like electrochemical plating are preferred to have improved interfacial contact. The use of carbon-based materials often shows moderate areal capacitance owing to limited electrode thickness, however, electrodeposition of pseudocapacitive materials such as metal oxides or conducting polymers can render greater performance in aqueous electrolytes. Nevertheless, aqueous electrolytes put constraints on cell voltage (< ~1.6 V) and energy density. Developing aqueous-based gel electrolytes can potentially resolve electrolyte leakage problems and eliminate the need for hermetically sealed packaging. [41] However, to meet future industry demands, high-voltage solid-state electrolytes need to replace the polyvinyl-alcohol (PVA) based aqueous gel electrolytes with a limited voltage window (~ 1 V). Ionic-liquid-based gel electrolytes (ionogels) can mitigate some of these challenges by offering operating voltage windows up to 3 V. [42] Advancement of 3D

MSCs using 3D architecting of electrode structure can further boost the charge storage performance. [20], [43], [44] Besides, developing hybrid MSC combining capacitive and high-rate battery materials with proper charge balancing can make MSCs a potential competitor for micro-batteries for applications in embedded sensors for battery monitoring, energy harvesting, wearable electronics, etc.

1.4.3 Electrode deposition techniques

There are two categories primarily available to realize the construction of micro-supercapacitors. The first category **(Figure 1.7 a)** consists of the transfer or loading of electrode material in powder form onto the micro-supercapacitor through different printing techniques or via electrophoresis. Some of the techniques including inkjet printing [45], screen printing [46], spray coating [47], and electrophoretic deposition [48], have been utilized to real realize micro-supercapacitors based on carbonaceous materials. A mixture of active material, binder, and/or conductive additives is dissolved in a solvent to make a stable colloidal suspension or a viscous paste before being locally deposited onto metallic current collectors that were patterned beforehand on the insulating substrate.

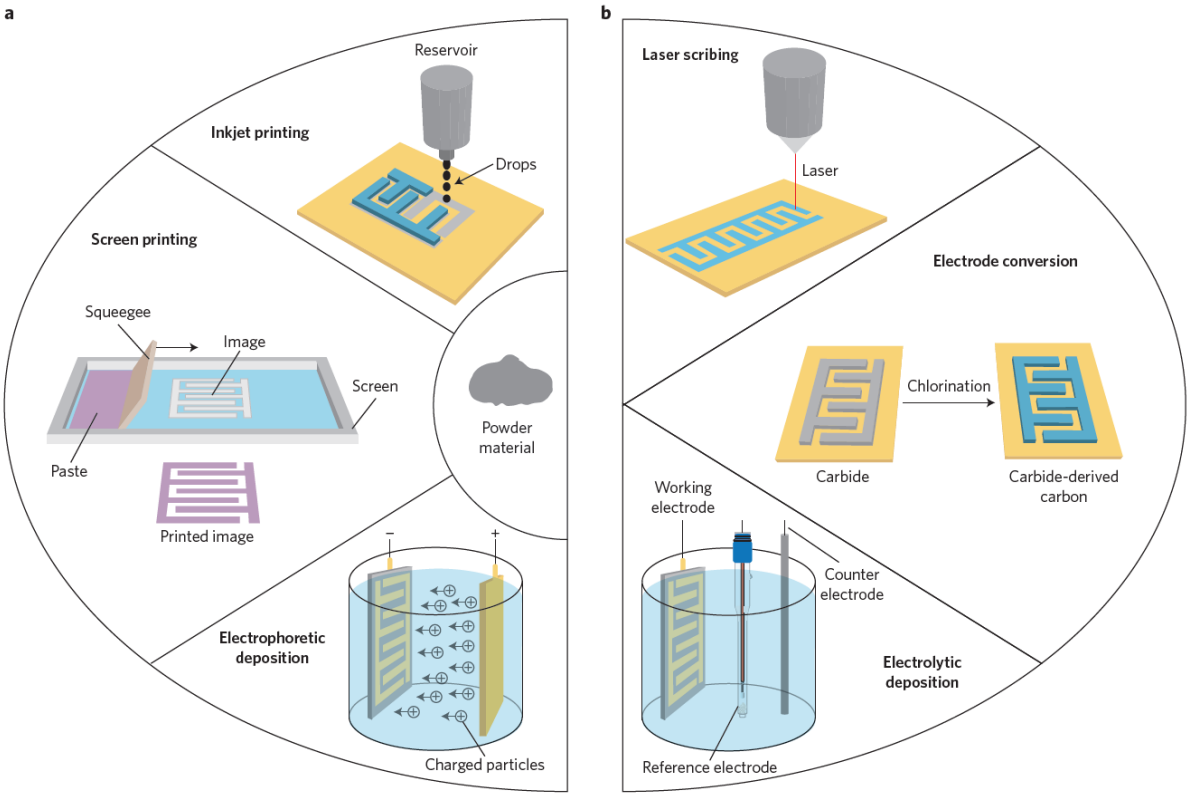

Figure 1.7: Representative microfabrication processes employed for the realization of planar on-chip micro-supercapacitors. a) Technologies based on the integration of the electrode material within the microdevices starting from an existing powder: a viscous paste or a colloidal suspension is created and locally deposited onto patterned current collectors via inkjet printing, screen printing, or electrophoretic deposition. b) Technologies based on in situ synthesis of the active material: the electrode material is formed by laser irradiation, chemical conversion, or electrolytic deposition during the manufacture of the microdevice. [49]

In the second category as shown in **Figure 1.7 b**, the electrode material is produced directly (from solution or by the chemical transformation of a pre-coated material) during the microdevice manufacturing itself [50], [51], [52], [53]. For instance, in laser scribing using focused laser beams, graphene patterns are generated from a graphite oxide thin film through a concurrent reduction and scribing process, which can act as a binder-free electrode without any current collectors [54], [55], [56]. The micro-supercapacitor electrodes are also realized by direct photoresist patterning and etching of precursor materials (e.g., carbide-derived carbons) [57], [58], [59]. Instead, the electrode material can be integrated onto patterned current collector substrates utilizing

electrolytic deposition or electrochemical polymerization, commonly used for pseudo-capacitive materials such as conducting polymers and transition metal oxides [60], [61], [62], [63], [64], [65]. This is an efficient approach considering the scaling up of device fabrication i.e., numerous components can be realized in a single step within a single wafer in a cost-effective manner. Importantly the approaches mentioned here lead to self-supported electrodes with excellent adhesion to the current collector and the substrate devoid of any inactive components, such as conductive additives, binders, or charging agents.

1.5 Electrolytes for SCs

Electrolytes (liquid or solid-state) are one of the principal components of supercapacitors (SCs), delivering ionic conductivity and allowing charge compensation in each electrode during charge-discharge cycles, and determining the overall performance of electrochemical energy storage. The electrolyte plays a fundamental role in the EDL formation (in EDLCs) and the reversible redox process for charge storage (in PCs), and some PC materials requires certain species to be present in the electrolyte (e.g., H^+ for RuO_2) to promote surface controlled faradaic reactions. The effects of electrolyte properties on the performance of supercapacitors are depicted in **Figure 1.8**. The electrolyte nature, including the ion type and size, the concentration and solvent used, their interaction, the interaction between the electrolyte and the electrode materials, and their electrochemical stability window (ESW) altogether play a critical role in the charge storage of EDLCs and PCs, their energy and power densities as well as the lifetime of SCs. For instance, the ionic conductivity of the electrolyte affects the ESR of the SCs, which affects the power density and ESW determines the operating voltage of the SCs, thereby energy densities. Therefore, the electrolytes manifesting wider ESW and higher ionic conductivity are the potential choice for the high performance of supercapacitors. Furthermore, the interactions between the ion and the

solvent as well as between the electrolyte and the electrode material can affect the lifetime and self-discharge of SCs. The other important parameters including internal resistance, rate performance, operating temperature, and toxicity need to be carefully treated considering the practical use of supercapacitors.

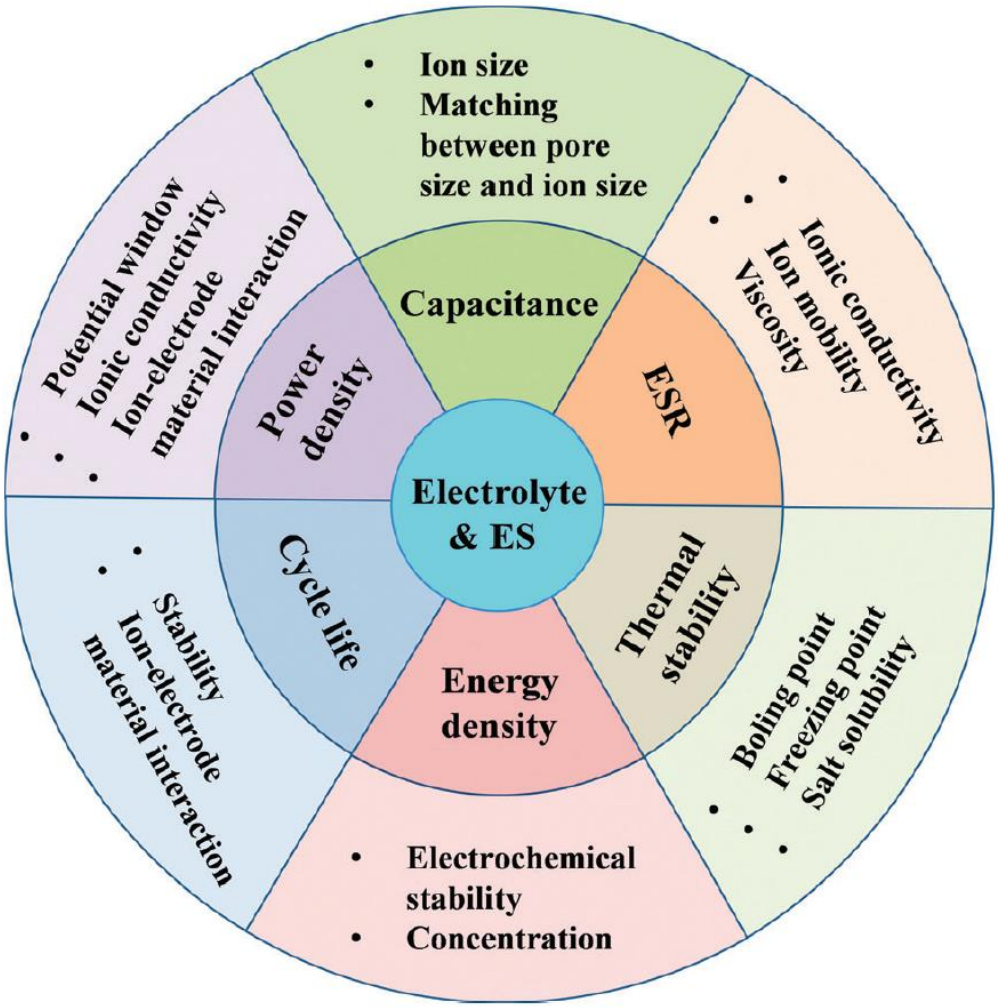

Figure 1.8: Effects of the electrolyte on the ES performance. [66]

The general classification of electrolytes is shown in the diagram in **Figure 1.9**. Based on the nature of the electrolyte, they can be classified as liquid electrolytes and solid/quasi-solid-state electrolytes. In general, liquid electrolytes can be further classified into aqueous electrolytes,

organic electrolytes, and ionic liquids (ILs). On the other hand, solid or quasi-solid-state electrolytes can be divided into organic solid electrolytes and inorganic solid-state electrolytes. All these electrolytes have their own merits and demerits, there hasn't been a perfect choice of electrolyte developed to meet all the requirements. For instance, aqueous electrolytes exhibit high conductivity and capacitance, yet their operating working voltage is limited due to the narrow decomposition potential of water (1.23 V). Despite the higher voltage windows of organic and IL electrolytes, they normally show lower ionic conductivities. Solid-state electrolytes can mitigate the potential leakage issue of liquid electrolytes, but they also suffer from poor conductivity. To overcome these drawbacks, extensive efforts have been made to develop novel electrolyte materials to improve overall energy storage performance. These include developing new and high-performing electrolytes that can operate in wide potential windows with higher ionic conductivity, and lower viscosity, and work with broad working temperatures. This will allow exploiting the positive effects of given electrolytes on the performance including high capacitance, energy and power density, thermal stability, and low self-discharge. Also, it is important to have a fundamental understanding of the choice of the electrolyte on the SC performance through advanced modeling and simulation techniques. Herein, the following subsections will be focused on a brief review of common types of electrolytes for SCs such as aqueous, organic, ionic liquids, and solid or quasi-solid-state electrolytes.

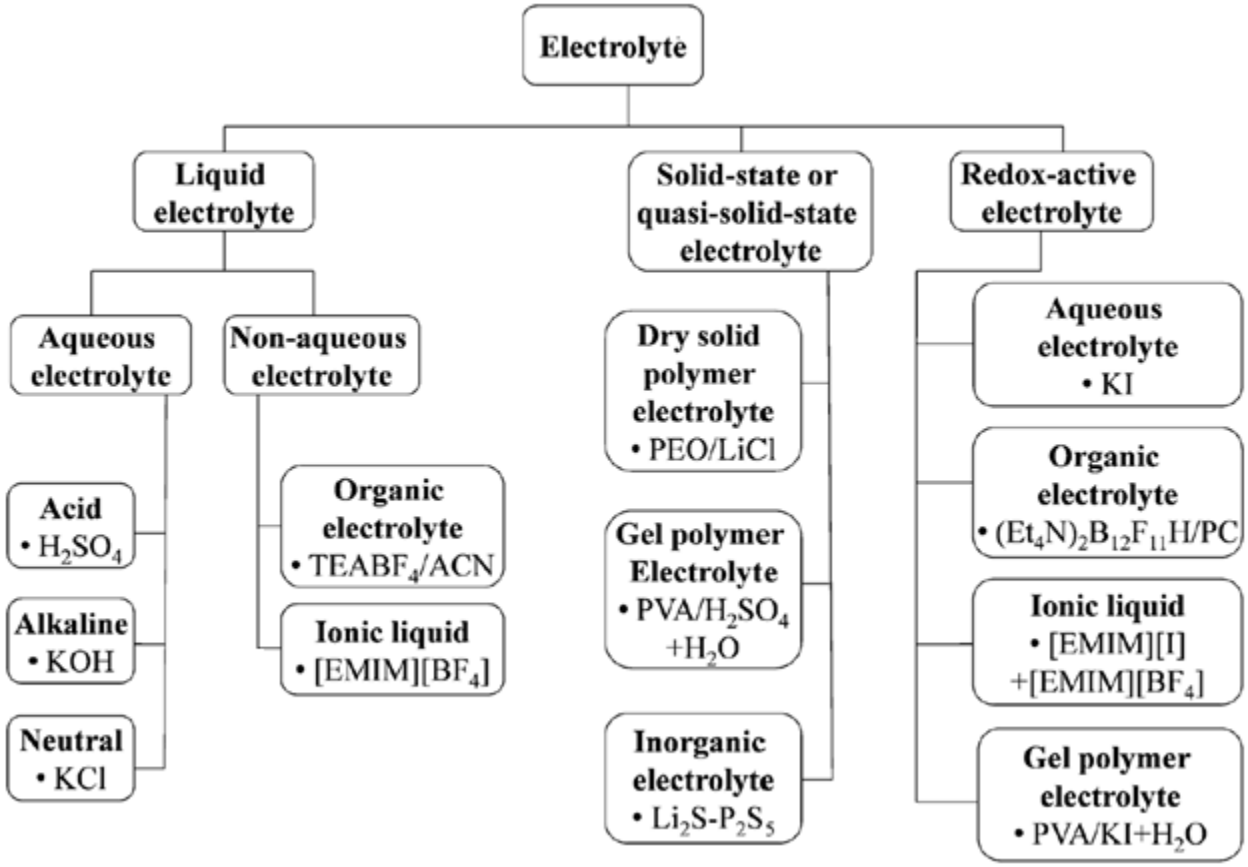

Figure 1.9: Classification of electrolytes for electrochemical supercapacitors. [66] (TEA: tetraethyl ammonium; EMIM: 1-ethyl-3-methylimidazolium; ACN: acetonitrile; PEO: polyethylene oxide; PVA: polyvinyl alcohol; Et_4N: tetraethylammonium; PC: polycarbonate).

1.5.1 Aqueous and Organic Electrolytes

Aqueous Electrolytes: Aqueous electrolytes are widely used in electrochemical devices because they are inexpensive, safe and easy to handle, and exhibit high capacitance, and conductivity, which is at least one order of magnitude higher than that of organic and IL electrolytes, but the thermodynamic limitation of water electrolysis beyond 1.23 V (under standard conditions) limits the operating voltage leading to lower the energy density. However, their low ESR values can render better power delivery performance for SCs. The size of the bare and hydrated ions and the mobility of the ions not only influence the ionic conductivity but also the overall specific

capacitance. Also, the ESPW of electrolytes and the corrosive degree should be considered. Generally, aqueous electrolytes can be subdivided into acid, alkaline, and neutral solutions with H_2SO_4, KOH, and Na_2SO_4 as representative examples and the frequently used electrolytes. The maximum capacitance of SCs with EDLC materials such as activated carbon in aqueous electrolytes has been reported in the range from 100 to 300 Fg^{-1}. [5] In pseudocapacitors, it has been widely reported that using acid electrolyte the specific capacitance can be greatly improved due to the fast-redox reactions by exchanging the protons at the electrode surface. As discussed before, the main disadvantage of aqueous electrolytes is their relatively narrow ESW, restricted by the decomposition of water. For example, under standard conditions with a 1M concentration of the electrolyte, hydrogen evolution occurs at a negative electrode potential of around 0 V vs. SHE, and oxygen evolution at a positive electrode potential of around 1.23 V, leading to the SC with a cell voltage of ca. 1.23 V. [66]The gas evolution at higher potential can lead to the degradation of the SC cells, which imposes safety concern and performance drop. To avoid this, the cell voltage of aqueous electrolyte-based SCs is normally restricted to about 1.0 V. Besides, the operating temperature range of SCs with aqueous electrolytes has also to be limited to the freezing point and the boiling point of water.

Organic Electrolytes: Organic electrolytes currently dominate the commercial market in combination with EDLC electrodes, primarily due to their high ESW (2.5 to 2.8 V). This can significantly enhance both the energy and power densities of EDLCs compared with aqueous electrolytes. Nevertheless, they are usually associated with high cost, lower ionic conductivity, high flammability, volatility, and toxicity issues. [66] Besides, organic electrolytes have a larger solvated ion size leading to lower capacitance in SCs. To have ionic conductivity it is necessary to dissolve conducting salts in organic solvents to formulate the organic electrolyte. For instance, the typical organic electrolyte for SCs is tetraethylammonium tetrafluoroborate ($TEABF_4$) dissolved

in acetonitrile (ACN) or propylene carbonate (PC). With this electrolyte, it is possible to store a maximum capacitance, maximum energy, and power densities around 150 Fg^{-1}, 25 W h kg^{-1}, and 25 kW kg^{-1}, respectively by using highly porous interconnected carbon nanosheet-based SCs operating at 2.7 V. [67] If the carbon pore size of the electrode material could be adapted to the electrolyte ion size, the capacitance, and the energy density would increase significantly. The other commonly used solutes for organic electrolytes are tetraalkylammonium salts of anions that are electrochemically stable, such as BF_4^-, $PF_6^-$and AsF_6^-. The concentration of the electrolyte is usually determined by the final conductivity of electrolytes and the operating temperature range. It's noteworthy that the ESW of organic electrolytes is dependent on several other factors including the type of conducting salts (cations and anions), solvents, and impurities, especially trace amounts of moisture can have harmful effects on ESW. In some reports, organic electrolyte-based SCs are charged beyond their normal ESW, where unwanted side reactions/redox reactions may happen for the electrode materials or electrolytes, which can cause self-discharge and gas evolution due to potential electrolyte degradation and electrochemical oxidation. [68] Moreover, their intrinsic volatile nature is a shortcoming compared to other electrolyte systems considering long-term performance and safety. In addition to the organic cations, organic salts based on the inorganic cations, such as Li^+, Na^+, and Mg^{2+} have also attracted lots of attention. In particular, organic electrolytes based on lithium salts have been widely used in pseudocapacitors and hybrid SCs due to the small ionic size of Li^+ but with a bigger solvation shell, which is largely inspired by lithium-ion batteries. [69]

1.5.2 Ionic Liquid Electrolytes

Ionic liquids (ILs) are room-temperature molten organic salts (solvent-free electrolytes), that are liquid at low temperatures. composed of ions (cations and anions) with melting points below 100 ºC. ILs are usually comprised of asymmetric organic cations and inorganic or organic

anions with a smaller lattice energy exhibiting high entropy for melting due to many conformations that the large alkyl chains can adopt, leading to a low melting point. [70] The key properties of ILs include high thermal, chemical, and electrochemical stability, nonvolatility, etc. The very low vapor pressure of ILs even at an elevated temperature reduces the risk of flammability. Due to their limitless structural variations and unique properties, ILs are employed in a wide range of applications including alternative electrolytes for energy storage devices such as SCs. [71], [72], [73] The physical and chemical properties of ILs can be tailored for task-specific applications owing to a large variety of cation-anion combinations. This property is very attractive for the applications of ILs as electrolytes in SCs since the IL electrolytes can be optimized or customized to meet certain requirements of SCs such as the operative cell voltage, the working temperature range, ESR (related to the ionic conductivity), etc. Based on their composition, ILs can be classified into aprotic, protic, and zwitterionic types (Figure 10). The ILs used in SCs only account for a small fraction of the large family of ILs. In reported literature, the commonly employed ILs in SCs are based on imidazolium, pyrrolidinium, ammonium, sulfonium, phosphonium cations, etc. and the typical anions are tetrafluoroborate (BF_4^-), hexafluorophosphate (PF_6^-), bis(trifluoromethane sulfonyl)imide (TFSI or NTf_2), bis(fluoro sulfonyl)imide (FSI), dicyanamide (DCA), etc. There is a trade-off between the ionic conductivity, melting point, viscosity, and ESPW of ILs. In general, the imidazolium-based ILs offer higher ionic conductivity while the pyrrolidinium-based ILs have larger ESPW. Unlike organic electrolytes, SCs using IL electrolytes could offer higher operating cell voltages above 3 V with no safety issues even when operating at high temperatures. Nevertheless, high viscosity, low ionic conductivity, and high-cost limit their practical use in SCs. Both conductivity and viscosity drawbacks of IL-based electrolytes particularly at low temperatures can significantly increase the ESR of SCs, which can hinder the rate and power density even though the loss in power density can be compensated by the high energy density

performance. Moreover, the capacitance of IL-based SCs is often lower than that of both aqueous and organic electrolyte-based SCs largely at high charge-discharge or scan rates, possibly due to high viscosity affecting the charge storage kinetics. To overcome these shortcomings, efforts have been put forth to rationally select the IL composition and cell design by both experimental and theoretical studies, giving fundamental insights into ion dynamics at the interface of IL and electrode as well as through molecular mechanisms. [74], [75], [76], [77] Hence, the research direction on IL-based SCs is mainly focused on the following aspects: (1) fundamental understanding of the EDL structure and its effect on the capacitance; (2) improvement of the properties related to electrochemical performances of ILs (e.g., ionic conductivity, viscosity, and ESPW) by modifying the cations or anions of ILs; (3) utilizing a mixture of ILs or addition of organic solvents to enhance the overall performance. It's noteworthy that mostly carbon-based materials are primarily used for such studies and reports on the behavior of ionic-liquids using metal oxide-based electrodes are scarce especially when the interface becomes more complex as charge storage is dominated by the kinetics of redox reactions.

1.5.3 Types and Physicochemical Properties of Ionic Liquids

Based on the composition, ILs can be classified as aprotic, protic, and zwitterionic **Figure 1.10**. Aprotic ILs are suitable for lithium-ion batteries and supercapacitors (mostly with EDLCs) while the protic ILs are employed for fuel cell applications and also in energy storage applications. Compared to aprotic ionic liquids, protic ionic liquids are cheaper, easier to synthesis, and usually are less viscous. [78] Zwitterion ILs are more suitable for electrochemical devices with the addition of salt as well as in ionic liquid-based membrane systems. [70] Aprotic ILs can be prepared by the reaction of the metathesis of halide salt with group 1 metal ammonium salt of the desired anion. [79] Protic ILs are originated by the transfer of a proton from a Brönsted acid to a Brönsted base (usually an amine). [80], [81] Whereas, Zwitterionic ILs can be prepared from a typical ion pair of

imidazolium IL and sulfonates, dicyanide, or carboxylate mostly used for proton exchange membrane applications. [79]

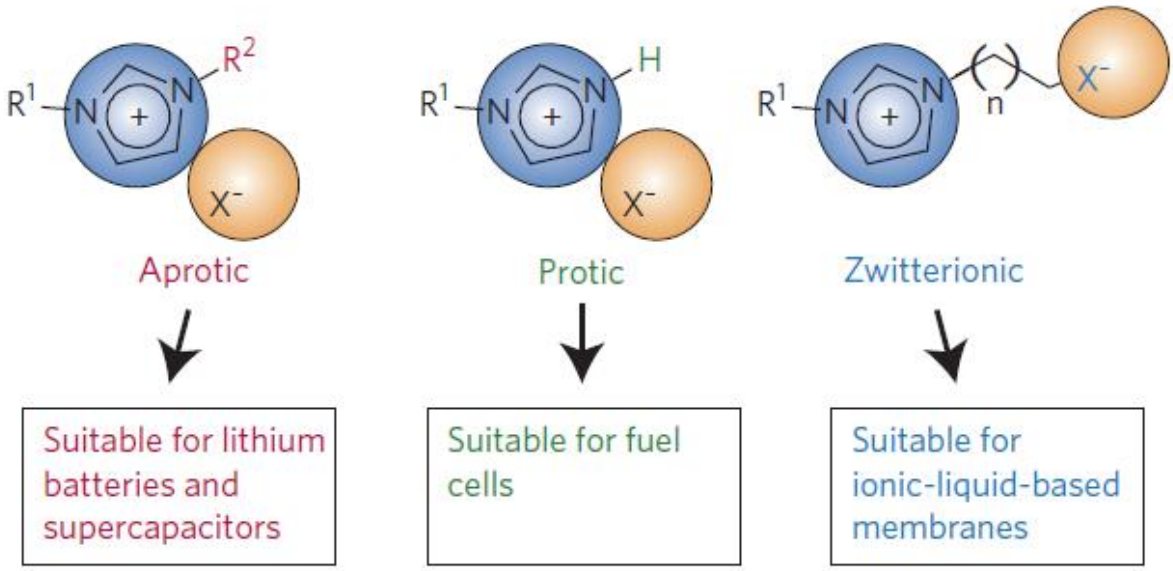

Figure 1.10: Types of ionic liquids used for different applications: aprotic, protic, and zwitterionic. [70]

A combination of different cations and anions gives rise to flexibility in material design and variation of their properties for specific applications. The common cations are imidazolium, pyrrolidinium quaternary ammonium, among others. The common anions cover a broad range of inorganic (e.g. halides (Cl^-, Br^-, I^-), polyatomic inorganics (PF_6^-, BF_4^-), and polyoxometallates), or more typically from organic anions such as NO_3^-, $TFSI^-$, and FSI^- (**Figure 1.11)**.

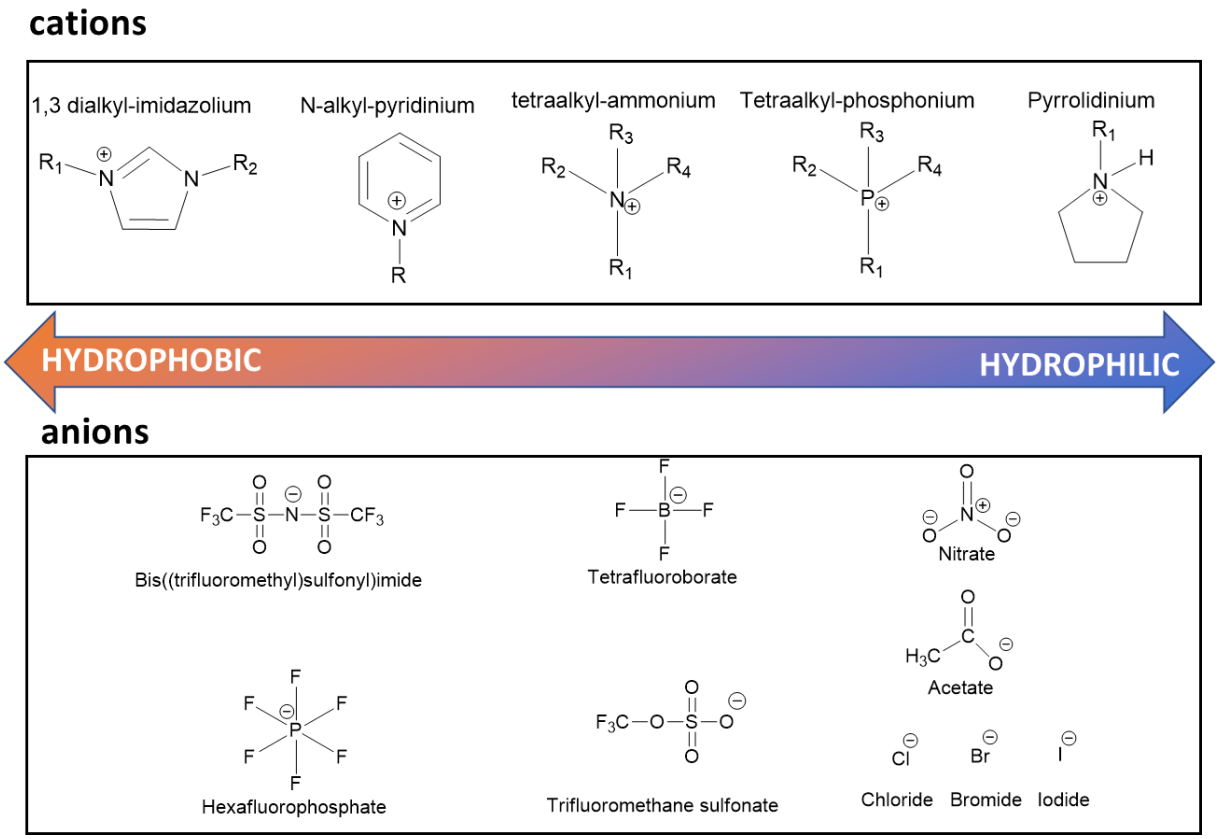

Figure 1.11: Commonly used cations, and anions of ILs described in the literature.

The conductivity and ESW of ILs are paramount in determining the performance of SCs, which greatly depends on the type of cation and anion groups. **Figure 1.12** depicts the ionic conductivity and ESW of various ILs, where EMI-based ILs show the highest ionic conductivity reaching 10^{-2} S cm^{-1} at RT, but their ESW falls short of tetraalkylammonium or pyrrolidinium-based ILs due to the acidic proton of the imidazolium ring which can react, and limit the cathodic stability potential. This could be the main limitation in the practical use of imidazolium-based ILs for high-voltage batteries and supercapacitors. Although aliphatic quaternary ammonium and pyrrolidinium salts display the widest ESW, even exceeding 5V, their conductivity is generally lower than that of EMI-based ILs. The challenge is to design ILs that feature a wide ESW together with high conductivity in a wide temperature range by tailoring the chemistry of the ions.

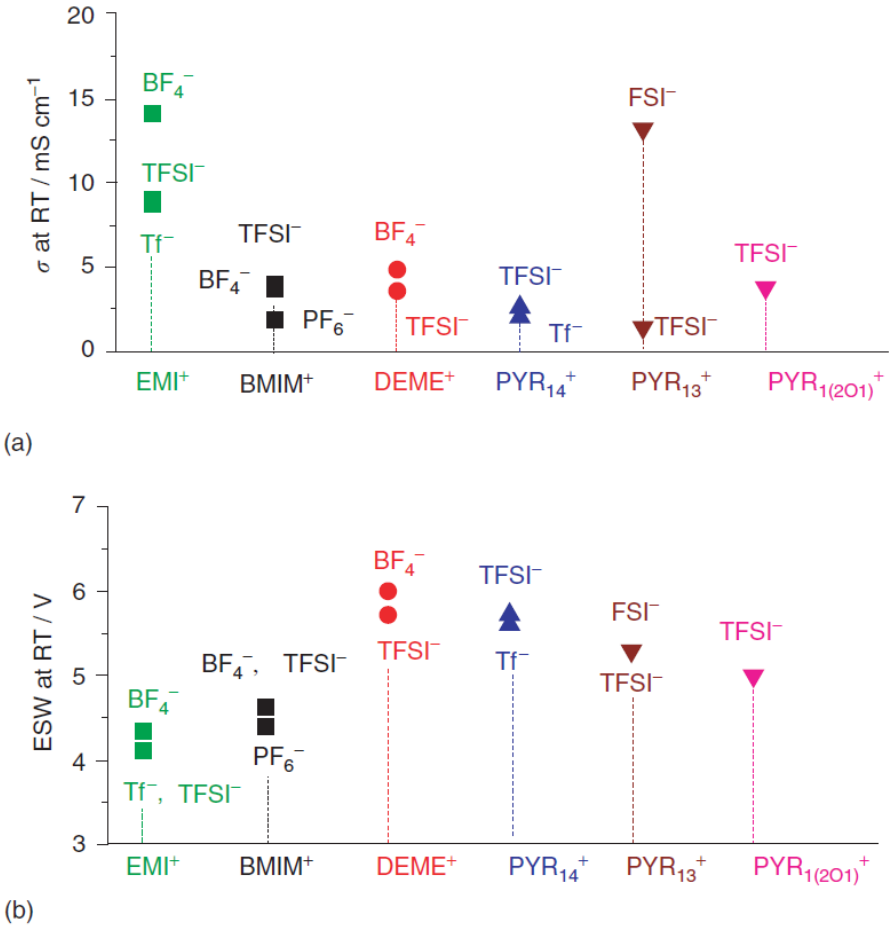

Figure 1.12: (a) Conductivity and (b) electrochemical stability window (ESW) data at room temperature of ILs based on 1-ethyl-3-methylimidazolium (EMI^+), 1-butyl-3-methylimidazolium ($BMIM^+$), N-diethyl-N-methyl(2-methoxyethyl)ammonium ($DEME^+$), N-butyl-N-methyl pyrrolidinium ($PYR14^+$), N-methyl-N-propyl-pyrrolidinium ($PYR13^+$), and N-methoxyethyl-N methylpyrrolidinium ($PYR_{1(201)}^+$) cations with different anions.

The versatility of ILs in terms of physicochemical properties (conductivity, hydrophobicity, melting point, viscosity, solubility, and chemical and thermal stabilities) can be varied by changing the substituent group or the cation or the combined anion. Watanabe et.al. described the ionicity of ILs, illustrating the structural change of cations or anions in ILs will result in a change in ionicity, controlled by the molecular forces (inter-ionic forces) and the nature of the IL nature. [82] The key factors affecting the properties of ILs are coulombic interactions, which increase the cohesion energy. For instance, if the ion pairs (the interaction between cations and anions) of ILs are sufficiently long-lived without any dissolution, they turned out to be neutral in

the electric field, which will not contribute to the ionic conductivity. The ionic conductivity strongly depends on the balance between anion–cation interactions and their respective volume, which greatly influence their application as electrolytes. Importantly, the coulombic interaction between anions and cations plays a major role in determining the quality of ILs. **Figure 1.13** depicts the general topology of ILs (good vs. poor) according to cation-anion interactions. Good IL electrolytes are certainly in the region where the interaction forces are weak (center region) vs. the poor ILs with stronger interaction forces. The molecular liquids or ionic crystals are formed as a result of these stronger interaction forces.

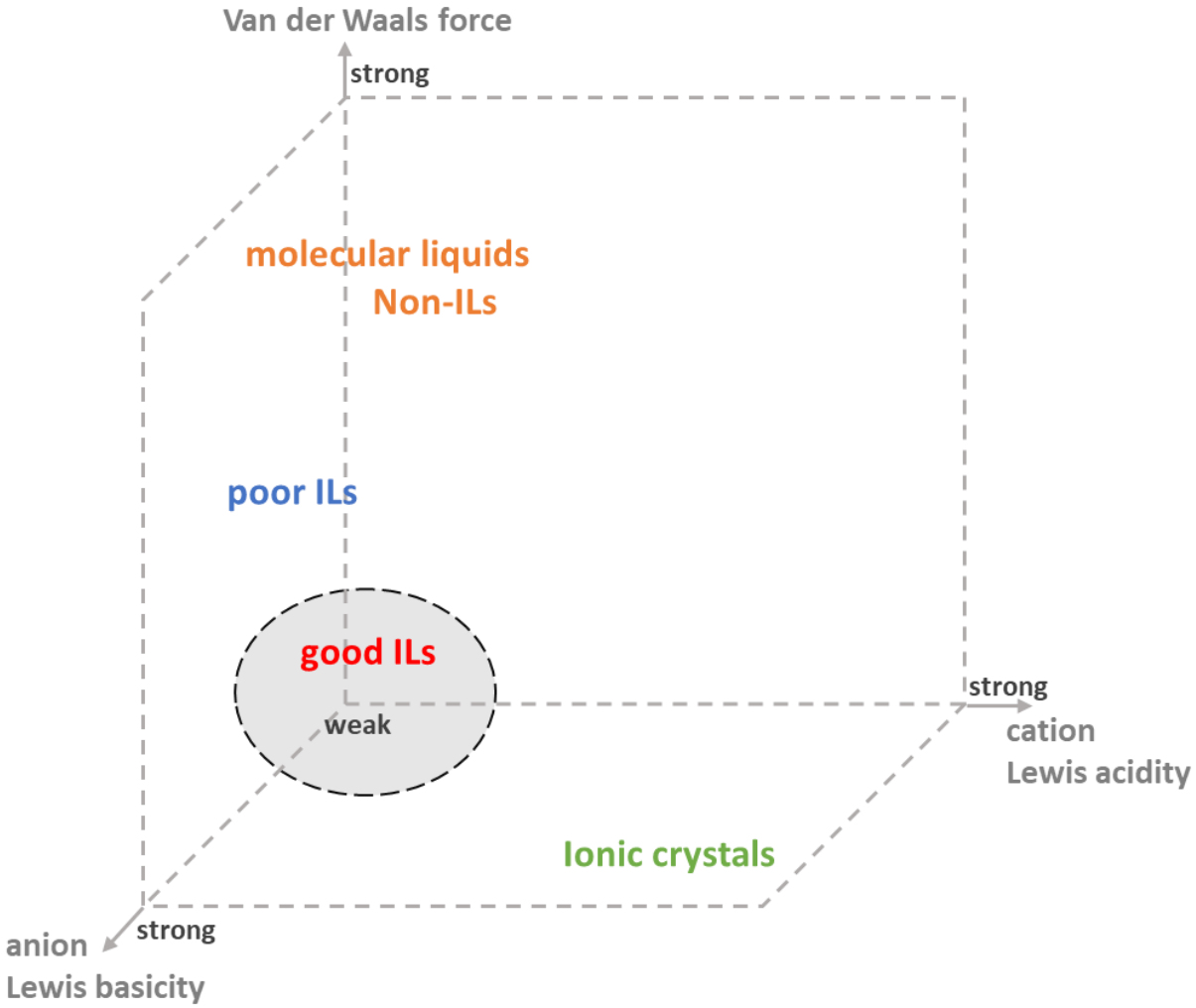

Figure 1.13: Quality of ILs depending on the interaction between cations and anions of ILs.

In general, the salt consists of cations, and anions are classified into one of four different groups according to their strength of interaction (**Figure 1.14**). Type-I salt is a combination of a strong Lewis-acidic cation with a strong Lewis-basic anion, Type -II is a weak Lewis-acidic cation with a strongly Lewis-basic anion. Type-III- is a combination of a strongly Lewis-acidic cation with a weakly Lewis-basic anion, and Type IV is a weakly Lewis-acidic cation with a weakly Lewis-basic anion. In Type I, the strong cation-anion interaction results in ionic crystals that cannot be dissociated into ions at room temperature unless they are solvated with amphiphilic solvents like water, which is generally not the case with typical ILs. Salts consisting of strong Lewis acidic cations (Type II) or strong Lewis basic anions (Type III) give rise to poorer IL ionicity than in the case of Type IV. Depending on their ionicity, Type-IV is considered to be good ILs, while Type-II and III are treated as poor ILs.

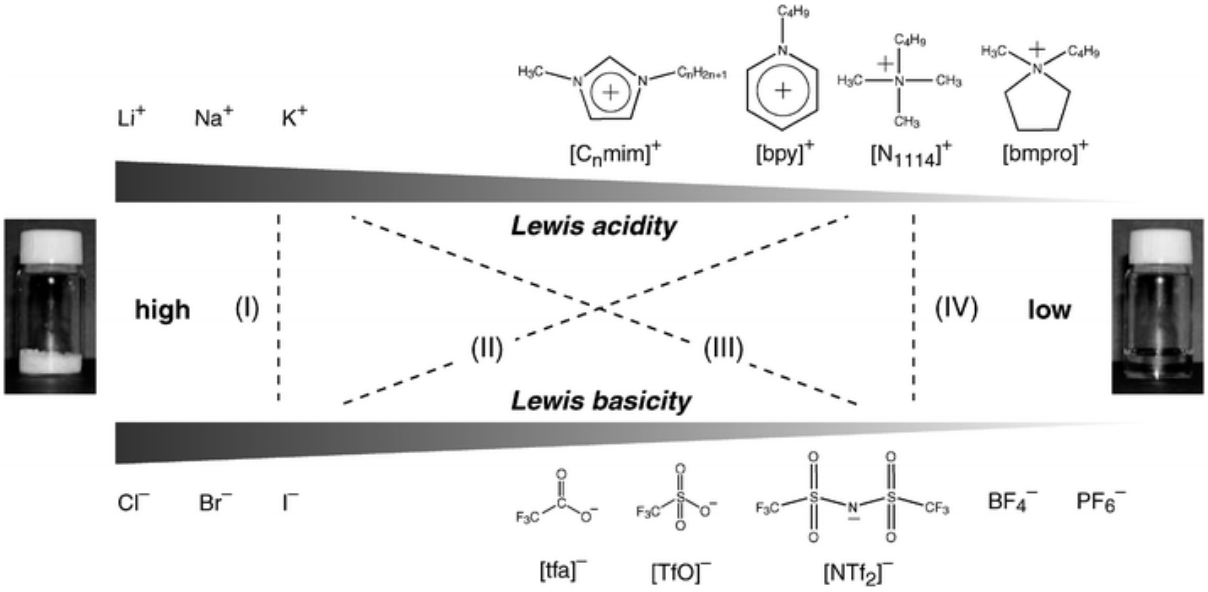

Figure 1.14: Various combinations of salts consisting of cations and anions, arranged in order of Lewis acidity for cations and Lewis basicity for anions. [$C_n$mim]: 1-alkyl-3-methylimidazolium, [bpy]: N-butylpyridinium, [bmpyr]: N-butyl-N-methylpyrrolidinium, [N_{1114}]: trimethyl-butylammonium, [tfa]: trifluoroacetate, [TfO]: trifluoromethanesulfonate, [NTf2]: bis(trifluoromethanesulfonyl)amide. [82]

1.5.4 Gel Electrolytes

With the growing interest in portable, wearable, and flexible electronic devices, solid-state electrolyte-based electrochemical energy storage devices have had a profound interest in recent years. The solid-state electrolytes are mostly polymer-based and are leakage free with no need for a separator which greatly simplifies the packaging and fabricating processes of SCs. They are subdivided into solid polymer electrolytes (SPEs), gel polymer electrolytes (GPEs), and polyelectrolytes (**Figure 1.15**). The GPEs are also known as quasi-solid-state electrolytes due to the presence of a liquid phase consisting of a polymer host (e.g., PVA) and an aqueous electrolyte (e.g., H_2SO_4), a conducting salt dissolved in a solvent or an IL. In this case, the polymer serves as a matrix, which can be swollen by the solvent, and the ions transport in the solvent instead of in the polymer phase. [40] The SPE is devoid of any solvents and they are composed of a polymer (e.g., PEO) and a salt (e.g., LiCl), where the ionic conductivity is mediated by the transportation of salt ions through the polymer. In a polyelectrolyte, the ionic conductivity is contributed by the charged polymer chains. All these types of solid-state electrolytes have their own merits and demerits. For instance, GPE has the highest ionic conductivity among these three and is widely employed for solid-state SCs, and studies on SPE-based SCs are scarce. However, depending on compositional difference, GPE may suffer from relatively poor mechanical strength and a narrow working temperature range particularly when water is used as the solvent medium. The poor mechanical strength of GPE may result in internal short circuits, which may lead to safety issues. Despite having low ionic conductivity, SPEs normally carry relatively high mechanical stability in comparison to GPE. The common disadvantage of solid-state electrolytes includes limited contact surface area between electrolytes and electrode materials especially when nano-porous active materials are used. This could lead to an increase in the ESR and can negatively affect the performance of SCs. There are often some trade-offs between ionic conductivity and mechanical

stability. Hence, it is important to develop solid-state electrolytes meeting the key requirements of high-performance SCs including high ionic conductivity, and chemical, mechanical, thermal, and electrochemical stability.

Ionogels are a new class of hybrid materials that contain ionic liquids in a solid structure. [42] The chemical composition and type of ionogel determine the properties of ionogel. Ionic liquid confinement will mitigate the leakage issue while maintaining the high ionic conductivity. Ionogels, in brief, combine the advantages of conductivity, nonvolatility, and transparency, making them more suitable for use in a variety of energy-related applications, including solid electrolytes for batteries, electrochemical capacitors, and actuators. [83], [84], [85] Due to its excellent adaptability, lightweight, and flexibility in areas ranging from clinical science to robotics, the use of ionogel in flexible electronic devices has also piqued the interest of researchers. [86] Ionogels can be classified into various categories (inorganic, organic, and organic–inorganic ionogel), and varied production methods must be taken into account. Nonetheless, ionogel's ionic conductivity may be of concern, as it only achieved 30% to 50% of pure ionic liquid conductivity, which may limit its practical application, and several efforts have been made to address this challenge. The fundamental issue is that when ionic conductivity improves, ionogel's mechanical strength suffers. As a result, creating ionogel with high conductivity and mechanical strength is still a difficult task.

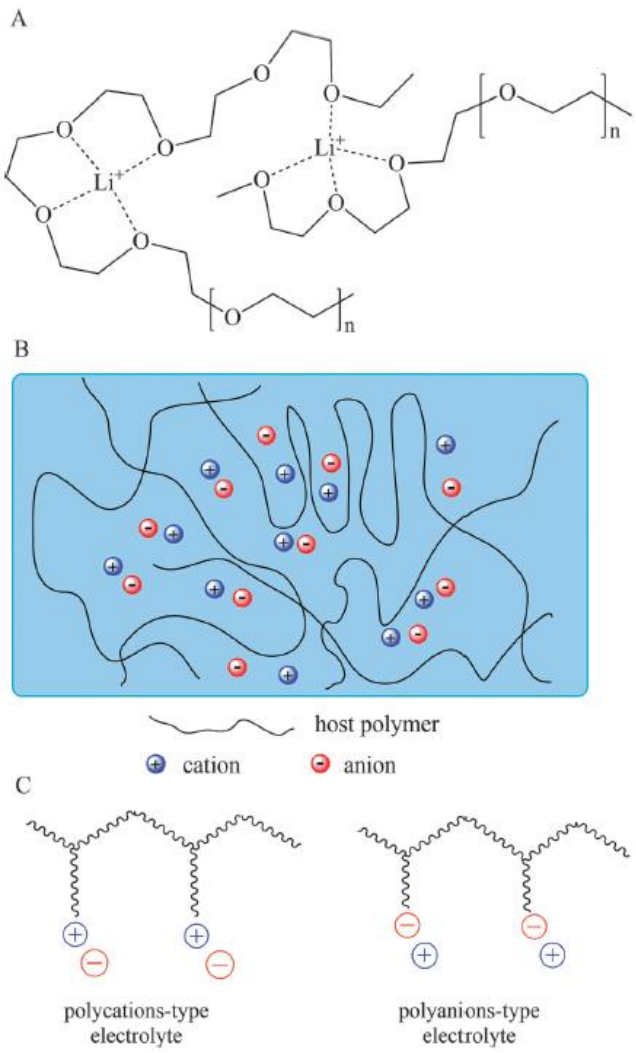

Figure 1.15: Various Schematic diagrams of (a) a dry solid-state polymer electrolyte (e.g., PEO/Li^+), (b) a gel polymer electrolyte, and (c) a polyelectrolyte. [66]

1.6 Characterization techniques

Characterization techniques help us to understand the properties (i.e., physical, chemical, morphological, electrochemical, etc.) of materials. In this part, we present a detailed description of various characterization techniques used to characterize nanomaterials and electrolytes. In addition, various electrochemical characterization methods employed to study charge storage in supercapacitors are given.

1.6.1 Material Characterization techniques

Materials Characterization is a significant step in understanding and probing material's physical, chemical, and microstructural properties. In this chapter, various characterization techniques used to study our materials are provided. This includes scanning electron microscope (SEM), transmission electron microscope (TEM), Energy Dispersive X-ray Analysis (EDAX), X-ray diffraction (XRD), and X-ray Photoelectron Spectroscopy (XPS).

1.6.1.1 Scanning and transmission electron microscopes

A scanning electron microscope (SEM) is a type of electron microscope used to visualize the surface topography and morphology of materials. The image of the sample is realized by scanning the sample with a focused electron beam and collecting the information when electrons interact with atoms on the material surface. Focused high-energy electrons are used for creating an image by detecting the backscattered or secondary electrons from the surface of the sample. The electron signals are collected by a detector and depending on the number of collected electrons, electron images are generated with varying intensity. [87] SEM does not have a limitation on the sample thickness and helps to provide information on the sample topology and surface structural features. Owing to a great depth of field (a few micrometers to several millimeters) and difference in contrast when more secondary electrons are emitted at a sharp edge of a feature can provide 3D shape information of the sample. [88] For insulating materials, such a surface-dominant interaction can cause surface charge accumulations. To overcome this, strategies such as conformal conducting coating (e.g., a few nanometers of carbon or gold) and low voltage (~0.3–5 keV) are applied such that the emitted electron current can balance the beam current. A modern SEM allows the observation and characterization of materials at the micro- to nano-scale. The main components

of a typical SEM include electron lenses, a sample stage, an electron gun, detectors, and a display. **Figure 1.16** provides a schematic diagram of an SEM, including the electron source (also called electron gun or electron emitter), condenser lenses, scan coils, and detectors. A high vacuum is required to operate an SEM. In this thesis, Hitachi S-4800 field emission electron microscope was used to study the surface morphology and measure the film thickness of the electrodes.

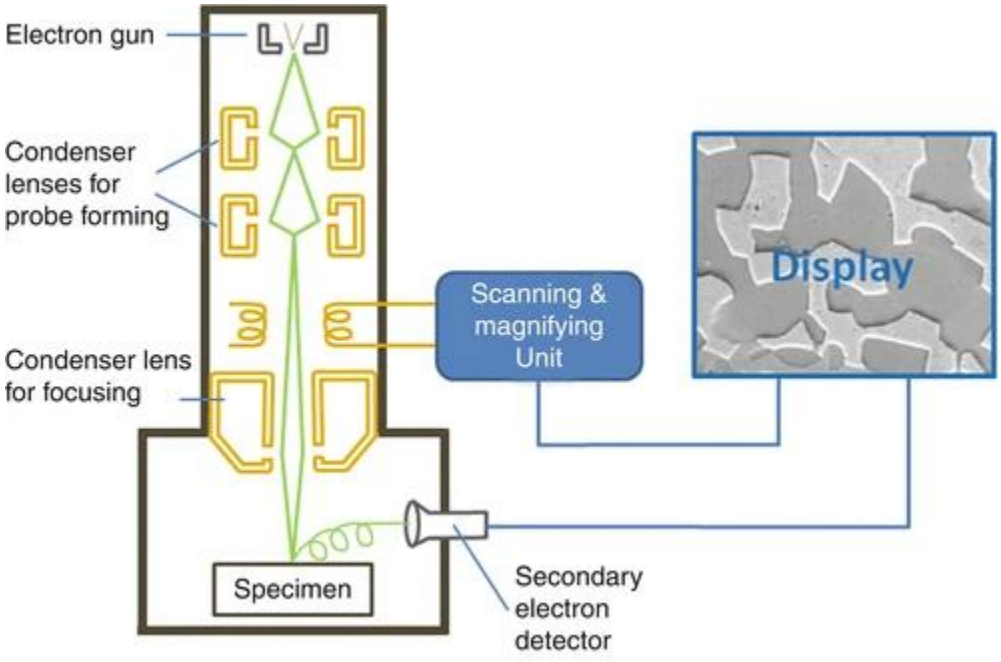

Figure 1.16: Schematic diagram of SEM, including major components. [87]

Compared to SEM, a transmission electron microscope (TEM) can provide a higher image resolution of 0.5–2 Å by utilizing electron beams of high accelerating voltage (60–400 keV) which is transmitted through the sample, focused by a series of electromagnetic lenses, and projected onto a screen or camera to generate sample images. A TEM can provide important information about the sample including the size and shape (based on bright-field (BF) TEM images), atomic arrangement, crystal structure, and orientation (high-angle annular dark field (HAADF) images based on STEM or diffraction patterns). For obtaining optimized resolution using thin samples (typically less than 200 nm), it's vital to use a thin film or a suspension on a grid to allow the

penetration of electrons. Necessary precautions should be taken for samples such as organic materials that can easily be damaged due to the high voltage applied. [89] In addition, a high-resolution TEM (HRTEM) explicitly uses transmitted and scattered electrons to construct an interference image of high-enough resolution to detect the arrangement of atoms in crystalline structures. Note that TEM normally gives only a 2D projection of a material and it is hard to distinguish the vertical structure of a material, such as identifying the atoms distributed above or beneath a certain plane.

Transmission electron microscopy (TEM) imaging was carried out using a JEOL 2100F microscope equipped with a Schottky field emission gun (FEG) operated at 200 kV and a Gatan RIO16IS CMOS camera.

1.6.1.2 Energy Dispersive X-ray Analysis (EDAX)

The energy-dispersive X-ray analysis is a useful technique to map the chemical composition of the sample. [90] The EDAX relies on the sample containing the element's unique atomic structure and its corresponding X-ray emission spectrum. When an electron is removed from the inner shell of an atom, a hole is generated which is then compensated by an electron coming from the outer shell. This process is accompanied by the emission of X-ray radiation with energy equal to the difference in energy between the two levels. Through EDAX measurement, the emitted X-ray radiations are detected.

1.6.1.3 X-ray diffraction (XRD)

X-ray diffraction (XRD) is a non-destructive technique providing crystallographic information about materials (structures, phases, preferred crystal orientation, etc.) using coherent scattering of X-rays by materials. The X-ray diffractometer works on the principle of Bragg's law of diffraction. [91] The monochromatic X-rays experience scattering from a crystalline solid and

the scattered beams interfere constructively or destructively leading to a diffraction pattern. The scattered waves undergo constructive interference when the path difference is an integral multiple of nλ, where λ is the wavelength of the incident X-ray beam. The path difference between the waves scattered at an angle 'θ' from crystal from two planes with inter-planar distance 'd' is 2d sinθ.

The crystallographic structures were analyzed by grazing incidence X-ray diffraction (GI-XRD) measurements on a Bruker D8 advanced X-ray diffractometer with Cu K_α radiation (1.54184 Å) operating at 40 kV and 40 mA.

1.6.1.4 X-ray Photoelectron Spectroscopy (XPS)

X-ray Photoelectron Spectroscopy is a surface-sensitive characterization technique providing information on elemental composition, empirical formula, and chemical and electronic state of elements present on the surface of a material. [92] The working principle of XPS is based on the photoelectric effect where electrons are emitted when light is incident on an atom. A typical XPS spectrum represents a plot of the number of electrons detected per unit of time versus their corresponding binding energy that gives a direct identification of elements present in or on the surface of the material. Importantly, the XPS peaks show a signature of the characteristic electronic configuration of the electrons within the atoms (1s, 2s, 2p, 3s, etc.). The XPS peak intensity gives information about the number of elements present within a given irradiated area and their corresponding atomic percentage can be calculated by dividing each raw XPS signal intensity by a "relative sensitivity factor" (RSF) and normalized over all of the elements detected.

In this work, the XPS spectra were obtained using a Thermo Scientific spectrometer operating with a monochromatic Al Kα X-ray source (1486.6 eV).

1.6.2 Electrolyte Characterization Tools

In this part, an introduction to important electrolyte characterization techniques such as Conductivity meter, Viscosity measurement, and Karl Fischer Titration along with useful information that can be derived from these techniques is provided.

1.6.2.1 Conductivity meter

Conductivity is a material's ability to pass an electric current and a conductivity meter is used to measure the conductivity in solutions. Electrolytes are substances that contain conductive salts dissolved in a solvent and can generate free ions. Ionic liquids have an advantage over traditional organic solvents in that their conductivity is inherent and they do not require the addition of a supporting electrolyte. The conductivity of a pure ionic liquid is determined by the mobility of the ions, which is affected by ion size, ion association, and viscosity in particular. [93] In fact, the change in conductivity with composition in ionic liquids is almost entirely due to changes in viscosity. [94] Low ion mobility and average conductivities are caused by the large size and high viscosity of the constituent ions. In electrochemical experiments, electrolyte conductivity is of vital importance. The key factors impacting conductivity measurement are temperature, the concentration of ions, and the nature of ions present.

In a conductivity meter, the conductance of the electrolyte solution can be determined by applying an alternating electrical current to the two electrodes present in the probe. While this electrical current is applied to the solution, the cations move to the negative electrode and the anions to the positive electrode side. This ionic migration is what defines a solution to be conductive or not. To obtain conductivity measurement, the cell constant and the conductance of the material have to be multiplied. Measured conductivity is typically measured in milliSiemens (mS) or microSiemens (µS). For most of the electrolytes, the temperature dependence of ionic

conductivity can be represented using an Arrhenius plot. On the other hand, Vogel-Fulcher-Tammann (VFT) equation is invoked when strongly temperature-dependent variation is observed in the supercooled regime, upon approaching the glass transition. [95] In this regime, the viscosity of certain electrolytes can increase by many orders of magnitude within a relatively narrow temperature interval.

Herein, the ionic conductivity of all the electrolytes studied was measured with a Jenway microvolume 120 mm reach glass conductivity probe (model 027815), made of two platinized platinum plates.

1.6.2.2 Viscosity measurement

The viscosity of a fluid is a measure of its resistance to deformation at a given rate. A viscometer measures dynamic viscosity and relative viscosity from samples with a volume as little as 100 µL by observing the rolling time of a ball in a capillary filled with sample liquid. Combined with density measurements, the result can be expressed as dynamic viscosity (mPa.s) and kinematic viscosity (mm^2/s).

The density and viscosity measurements of PILs were conducted simultaneously with an Anton-Paar DMA 5000 M and Lovis 2000ME, which use an oscillating U-tube principle for density and a rolling ball (falling sphere method) viscometer.

Conductivity and viscosity values can be used to provide information about the ionicity of ILs. A Walden plot of log(molar conductivity, Λ) versus log(reciprocal viscosity, η^{-1}), is a qualitative measure of the ionicity of the electrolyte. [80], [96] **Figure 1.17** shows a Walden plot of a series of the aprotic ILs reported in the literature. The straight reference line represents the Walden rule, Λ η = constant, where the ions are fully dissociated and have equal mobility. Any deviations from

the ideal line in the Walden plot, Angell *et al.* have classified specific ILs as either ‘‘good’’ ILs, ‘‘poor’’ ILs, or non-ionic (molecular) liquids. [97]

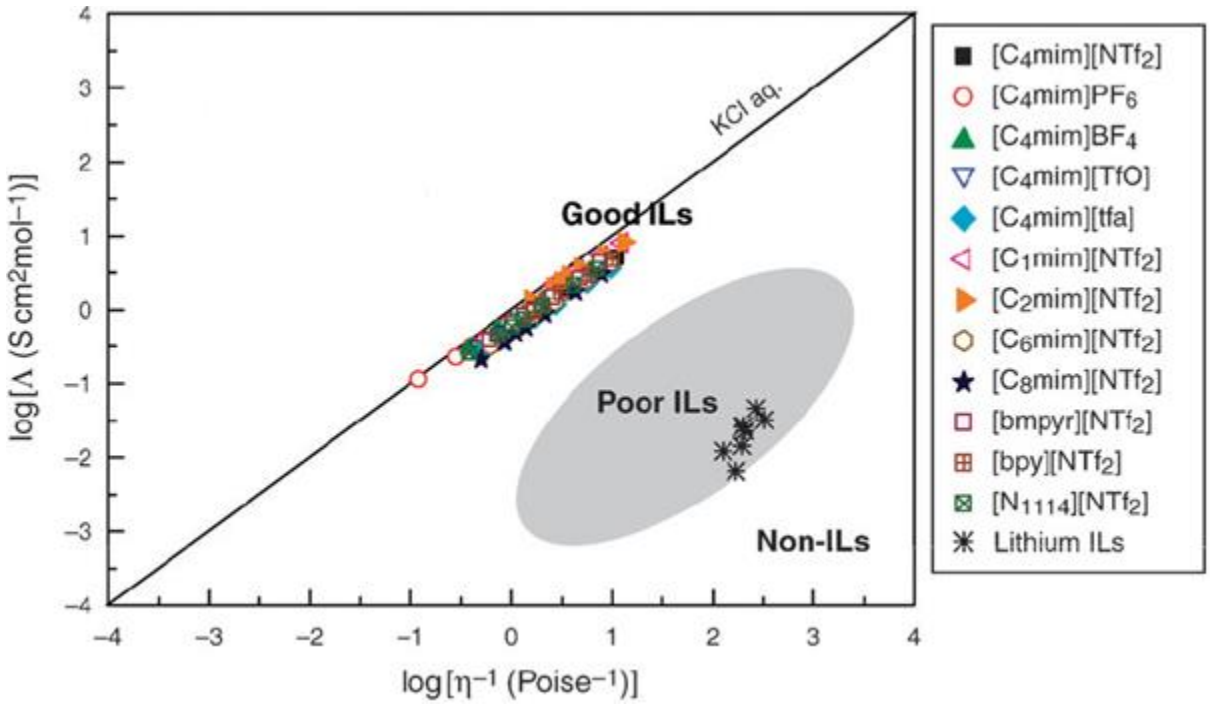

Figure 1.17: Walden plot of log(molar conductivity, Λ) against log(reciprocal viscosity η^{-1}), which includes the classification for ILs proposed by Angell *et al.* [97] (C_1mim: 1,3-dimethylimidazolium; C_2mim: 1-ethyl-3-methylimidazolium; C_4mim: 1-Butyl-3-methylimidazolium; C_6mim: 1-hexyl-3-methylimidazolium; C_8mim: 1-octyl-3-methylimidazolium; bmpyr: 1-Butyl-1-methylpyrrolidinium; bpy: N-Butylpyridinium; N_{1114}: Butyltrimethylammonium; TfO: trifluoromethanesulfonate; tfa: trifluoroacetic acid; NTf_2: bis(trifluoromethanesulfonyl)imide).

1.6.2.3 Karl Fischer Titration

Karl Fischer titration is a classic titration method that uses volumetric or coulometric titration to determine trace amounts of water present in a given analyte. This method for quantitative chemical analysis was developed by the German chemist Karl Fischer in the year 1935. Today, the titration is done with an automated Karl Fischer titrator. The principle of Karl Fischer titration is based on the oxidation reaction between iodine and sulfur dioxide. Water reacts with iodine and

sulfur dioxide to form sulfur trioxide and hydrogen iodide. The reaction continues until all the water is consumed. The chemical equation for the same is shown below.

$$H_2O + SO_2 + I_2 \longrightarrow SO_3 + 2HI$$

The main compartment of the titration cell is composed of the anode solution and the analyte. The anode solution contains alcohol (ROH), a base (B), SO_2, and KI. Typical alcohols include ethanol, diethylene glycol monoethyl ether, or Methanol (absolute), sometimes known as Karl Fischer reagent. A common base that's used is imidazole.

The titration cell contains a smaller compartment with a cathode immersed in the anode solution of the main compartment along with an ion-permeable membrane separating the two compartments. When current is passed through the circuit, the Pt anode generates I_2 from the KI. The overall reaction of the oxidation of SO_2 by I_2 is given below. One mole of I_2 is consumed for each mole of H_2O, i.e., 2 moles of electrons are consumed per mole of water.

$$2I^- \longrightarrow I_2 + 2e^-$$

$$B\ I_2 + B\ SO_2 + B + H_2O \longrightarrow 2BH^+\ I^- + BSO_3$$

$$BSO_3 + ROH \longrightarrow BHRSO_4$$

The endpoint is determined most commonly by a bipotentiometric titration method, and for that, a second pair of Pt electrodes are inserted in the anode solution. The detector circuit controls a constant current between the two detector electrodes during titration. Before reaching the equivalence point, the solution contains I^- with a trace amount of I_2. At the equivalence point, excess I_2 appears and a sharp voltage drop marks the endpoint. The amount of charge required to generate I_2 and reach the endpoint can be used to calculate the amount of water in the sample.

1.6.3 Electrochemical characterization techniques

In this part, an introduction to different electrochemical characterization techniques used for the evaluation of the electrochemical performance of a SC and the information that can be extracted from these techniques is provided. The key techniques used are: Cyclic voltammetry (CV), galvanostatic charge-discharge (GCD), and electrochemical impedance spectroscopy (EIS), and these techniques can help us to measure fundamental parameters (voltage, current, and time) for SC. Additionally, other SC performance metrics including capacitance, equivalent series resistance (ESR), operating voltage, time constant, energy, and power performance can be derived from those parameters.

1.6.3.1 Cyclic Voltammetry

Cyclic voltammetry (CV) is a popular electrochemical analysis technique employed to investigate the reduction and oxidation processes of molecular species. [98] CV is used to determine the electrochemical properties including electrochemical stability window, capacitance, energy density, cycling stability, and kinetic information of electrochemical energy storage systems by applying different potential scan rates.

The basic principle of CV is to measure the current response of the working electrode by applying a linear voltage ramp between two voltage limits.

$$E(t) = E_0 + vt \tag{1.5}$$

where E (t) is the real-time potential (V), E_0 is the starting potential (V), v and t are the scan rate (V s^{-1}), and scan time (s), respectively.

A CV plot can show the capacitive behavior of the electrode plus any potential oxidation and reduction peaks. Hence, the potential at which the redox reactions take place can be determined

from this technique. [99]. A typical cyclic voltammogram for a double layer and electrochemically reversible and surface-controlled redox process is shown in **Figure 1.18**.

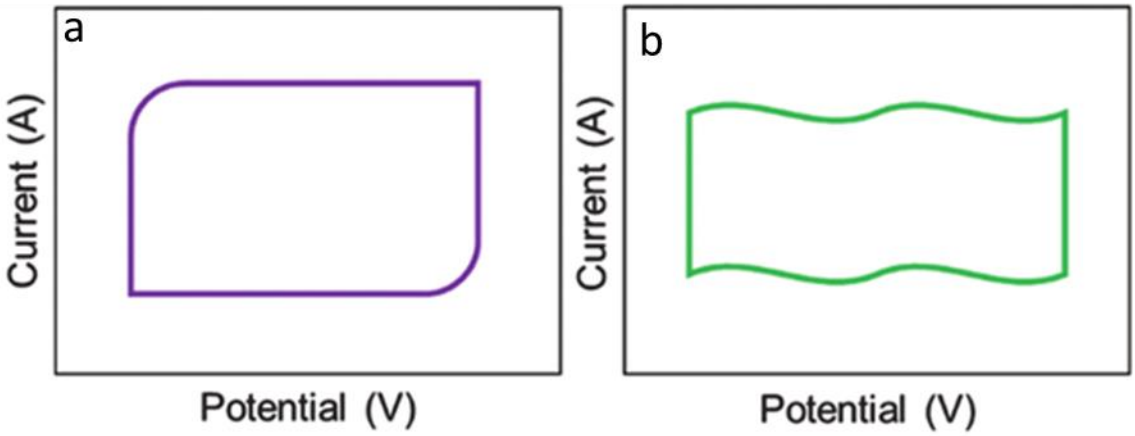

Figure 1.18: Typical CV curves for an ideal supercapacitor (a) and a pseudocapacitor showing broad peaks due to faradaic reactions (b).

Using a CV plot, an electrochemical operating stability window by successive adjustment of the reversal potential in a three-electrode system, and the reversibility of the charge and discharge processes can also be studied simultaneously. [100] To obtain the capacitance value, first discharge capacity Q (C) is calculated by integrating discharge current I (A) *vs.* discharge time t (s) and then divide using the potential window as given below.

$$C = \frac{\int_0^t i\, dt}{\Delta E} \qquad (1.6)$$

where *i* and ΔE denote the current (A) and the potential window (V), respectively.

In addition, the cycling stability of the supercapacitor device can be studied using CV by monitoring the variation in the capacitance up on cycling. Cyclic voltammetry is also a useful technique to elucidate the kinetic information of the device by applying varying scan rates.

1.6.3.2 Chronoamperometry

Chronoamperometry or galvanostatic charge-discharge (GCD) is a widely used electrochemical characterization technique under direct current for supercapacitors and batteries with the direct implication from lab scale to practical industry application. During GCD cycling, a constant current is applied and the voltage is measured. Using GCD, valuable information such as capacitance, resistance, and cyclability can be elucidated. Choosing appropriate constant current values is critical to producing consistent and comparable data from a GCD test. A typical GCD plot of an EDLC is shown in **Figure 1.19**. The capacitance can be calculated from the Equation below:

$$C = \frac{I}{\Delta E/\Delta t} \tag{1.7}$$

where I denote the applied current and $\Delta E/\Delta t$ is the slope of the curve. Importantly, this equation applies to only to EDLCs and ideal pseodocapacitors, and any deviation from straightline shouldnot be considered (energy should be measured instead). Moreover, to determine the ESR value of the supercapacitor, a voltage drop (inset of **Figure 1.19**) can be used. The GCD is the best way to evaluate the power density performance and study the electrochemical cycling life as it mimics the real operational condition of supercapacitors.

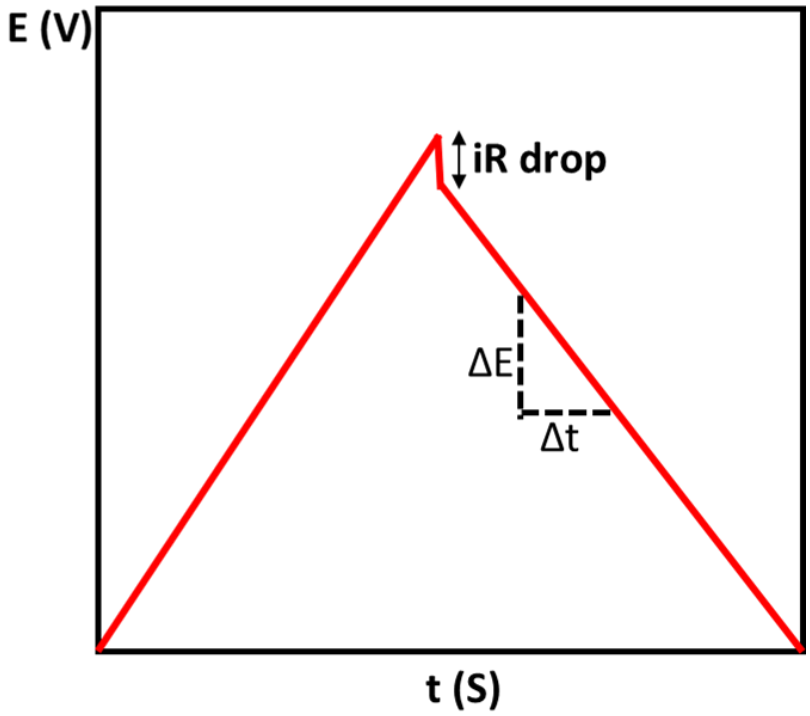

Figure 1.19: Galvanostatic charge-discharge (GCD) curve showing voltage variation versus time while applying constant current through a supercapacitor cell. The inset shows the voltage drop.

1.6.3.3 Electrochemical Impedance Spectroscopy

Electrochemical Impedance Spectroscopy (EIS) is a common technique for the electrochemical characterization of SCs. The EIS helps to measure the impedance of a power cell as a function of frequency by applying the alternating current (AC). Once an AC potential is applied to the system, the amplitude and phase angle of the output current are collected over a wide frequency range (~mHz to ~1 MHz). The resulting AC potential over the current ratio is measured in-phase (real impedance component) and out-of-phase (imaginary impedance component). The impedance behavior can be represented in the form of a Nyquist plot and a Bode plot. The Nyquist plot shows imaginary versus real impedance at different frequencies, and a Bode plot shows absolute impedance versus frequency. Nyquist plots should be represented in an absolute one-to-one ratio, where the X- and Y-axes form a square plot. The EIS studies can be

used to determine the equivalent series and charge transfer resistances, mass transport, and charge storage mechanisms in SCs. In addition, EIS can also be utilized to estimate the capacitance, energy, and power performance of SCs. [99]

Unlike EDLCs, pseudocapacitors exhibit a semi-circle in the high-frequency region of the Nyquist plot indicating the resistance of charge-transfer processes at the electrode/electrolyte interface **(Figure 1.20)**. The high-frequency region of the Nyquist plot helps us to determine the equivalent series resistance (ESR) and the charge transfer resistance of the device using the values of the real axis intercept and its distance to the mid-frequency region of the semi-circle. [101], [102] The mid-frequency region in the Nyquist plot often contains a Warburg element with a phase angle of ~45° showing solid-state diffusion processes and the curve gradually becomes vertical with a phase angle close to 90°. The low-frequency region displays the slow diffusion processes and their direct connection with the capacitive behavior of the device. [103]

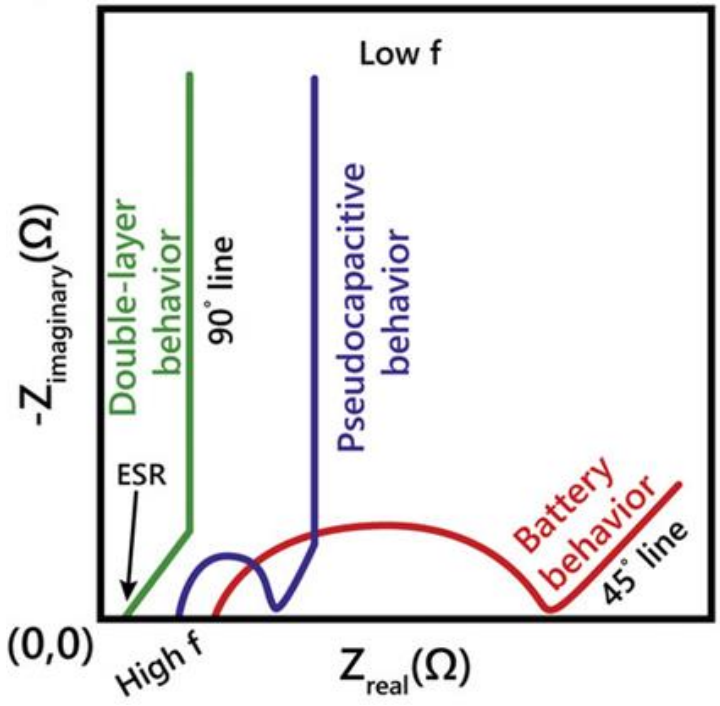

Figure 1.20: Typical Nyquist plot representations for an EDLC (green curve), pseudocapacitive materials (blue), and battery (red). ESR, 45°, and 90° lines are marked. [104]

The information on the relaxation time constant can be derived from the Bode plot. The relaxation time constant (τ_0) is the minimum time required to discharge all the energy from the device with an efficiency greater than 50%. It can be obtained from the characteristic frequency (f_0) at the phase angle of −45° ($\tau_0 = 1/f_0$). [105] The shorter relaxation time constant implies the better rate performance of the device.

1.7 Thesis Objectives

This thesis aims toward developing novel ionic-liquid (IL)-based electrolytes (both protic and aprotic) suitable for metal oxide (e.g., RuO_2, MnO_2)-based micro-supercapacitors (MSCs). Alternative to commonly used aqueous electrolytes for energy storage, ionic-liquid-based electrolytes manifest key properties including low vapor pressure, low m.p., etc. with a wide stability window and improved energy density performance, overcoming the major bottleneck faced by current SCs. The first key objectives were to design IL electrolytes rationally based on their physicochemical properties and a detailed understanding of their structure-property relation to be used as potential electrolytes in MSCs. The emphasis is then devoted to achieving benchmark energy storage performance including a detailed study on parameters including voltage range, capacitance, leakage current, etc. Given the growing future demands for flexible and portable electronic devices, developing efficient solid-state MSC devices is of greater importance. Hence, we dedicated our efforts to exploring ionogels as solid-state electrolytes derived from ILs for developing functional MSCs, which are compatible with microfabrication processes.

In Chapter 2, we show the use of various protic ionic liquid electrolytes for RuO_2 MSCs. Alternative to aqueous electrolytes that can efficiently work only around the room temperature

domain, Protic ionic liquids (PILs) can show extended electrochemical stability window (ESW) and can hence achieve a higher energy density for RuO_2 MSCs through pseudocapacitive charge storage. [106], [107], [108], [109]

$$RuO_2 + \delta H^+ + \delta e^- \leftrightarrow RuO_{2-\delta}(OH)_\delta$$

The PIL's viscosity and lower conductivity and its effect on MSC energy storage and rate performance are studied in detail. An enhanced charge storage kinetics of RuO_2 MSCs using PILs were achieved through proton conducting additives. Later, ionogel-based all-solid-state 3D MSC is realized that can potentially integrate with on-chip electronic devices meeting high energy and power expectations of future internet of things (IoT) technology.

In Chapter 3, Pyrrolidinium-based PILs containing varying alkyl substitution and anion groups are explored for RuO_2 MSCs. The electrochemical studies were performed extensively on both flat and porous substrates containing RuO_2 deposits. Given the practical application, ionogel electrolyte is developed using these electrolytes, and performance optimization is carried out at different state-of-charge and voltage ranges.

In Chapter 4, suitable IL electrolytes were envisaged for alternative pseudocapacitive metal-oxide electrodes such as $RuO_xN_yS_z$ and MnO_2. Proton-conducting additive-doped ILs and Na salt-containing ILs were explored for $RuO_xN_yS_z$ and MnO_2 MSC electrodes, respectively. A thorough understanding of the material and electrochemical characterization results, as well as performance optimization strategies, is detailed.

1.8 References

[1] V. Augustyn, P. Simon, B. Dunn, Energ Environ Sci 2014, 7, 1597.

[2] F. Wang, X. Wu, X. Yuan, Z. Liu, Y. Zhang, L. Fu, Y. Zhu, Q. Zhou, Y. Wu, W. Huang, Chem Soc Rev 2017, 46, 6816.

[3] Y. Wang, Y. Song, Y. Xia, Chem Soc Rev 2016, 45, 5925.

[4] P. Simon, Y. Gogotsi, Nat Mater 2020, 19, 1151.

[5] L. L. Zhang, X. S. Zhao, Chem Soc Rev 2009, 38, 2520.

[6] B. E. Conway, E. Gileadi, Trans. Faraday Soc. 1962, 58, 2493.

[7] T. Brousse, D. Bélanger, J. W. Long, J. Electrochem. Soc 2015, 162, A5185.

[8] L. Fu, Q. Qu, R. Holze, V. V. Kondratiev, Y. Wu, J. Mater. Chem. A 2019, 7, 14937.

[9] D. Galizzioli, F. Tantardini, S. Trasatti, J. Appl. Electrochem. 1974, 4, 57.

[10] V. Augustyn, J. Come, M. A. Lowe, J. W. Kim, P. L. Taberna, S. H. Tolbert, H. D. Abruna, P. Simon, B. Dunn, Nat Mater 2013, 12, 518.

[11] T. Brezesinski, J. Wang, S. H. Tolbert, B. Dunn, Nat Mater 2010, 9, 146.

[12] J. W. Kim, V. Augustyn, B. Dunn, Adv. Energy Mater 2012, 2, 141.

[13] H. S. Kim, J. B. Cook, H. Lin, J. S. Ko, S. H. Tolbert, V. Ozolins, B. Dunn, Nat Mater 2017, 16, 454.

[14] N. R. Chodankar, H. D. Pham, A. K. Nanjundan, J. F. S. Fernando, K. Jayaramulu, D. Golberg, Y. K. Han, D. P. Dubal, Small 2020, 16, e2002806.

[15] J. P. Zheng, P. J. Cygan, T. R. Jow, J. Electrochem. Soc. 2019, 142, 2699.

[16] P. Balaya, H. Li, L. Kienle, J. Maier, Adv Funct Mater 2003, 13, 621.

[17] W. D. Ryden, A. W. Lawson, C. C. Sartain, Phys Rev B 1970, 1, 1494.

[18] J. Riga, C. Tenret-Noël, J. J. Pireaux, R. Caudano, J. J. Verbist, Y. Gobillon, Phys. Scr. 1977, 16, 351.

[19] D. B. Rogers, R. D. Shannon, A. W. Sleight, J. L. Gillson, Inorg. Chem. 1969, 8, 841.

[20] A. Ferris, S. Garbarino, D. Guay, D. Pech, Adv Mater 2015, 27, 6625.

[21] S. Trasatti, G. Buzzanca, J. electroanal. chem. interfacial electrochem. 1971, 29, A1.

[22] S. Hadz¯i-Jordanov, H. Angerstein-Kozlowska, M. Vukovič, B. E. Conway, J. Electrochem. Soc 2019, 125, 1471.

[23] B. E. Conway, W. G. Pell, J Solid State Electr 2003, 7, 637.

[24] C. Choi, D. S. Ashby, D. M. Butts, R. H. DeBlock, Q. Wei, J. Lau, B. Dunn, Nat Rev Mater 2019, 5, 5.

[25] S. Ardizzone, G. Fregonara, S. Trasatti, Electrochim Acta 1990, 35, 263.

[26] I. Povar, O. Spinu, J. Electrochem. Sci. Eng. 2016, 6, 145.

[27] P. Simon, Y. Gogotsi, Nat Mater 2008, 7, 845.

[28] R. Lin, P.-L. Taberna, S. Fantini, V. Presser, C. R. Pérez, F. Malbosc, N. L. Rupesinghe, K. B. K. Teo, Y. Gogotsi, P. Simon, The J. Phys. Chem. Lett. 2011, 2, 2396.

[29] J. Yan, S. Li, B. Lan, Y. Wu, P. S. Lee, Adv Funct Mater 2019, 30, 1902564.

[30] C. Lethien, J. Le Bideau, T. Brousse, Energ Environ Sci 2019, 12, 96.

[31] S. M. Niu, N. Matsuhisa, L. Beker, J. X. Li, S. H. Wang, J. C. Wang, Y. W. Jiang, X. Z. Yan, Y. J. Yun, W. Burnetts, A. S. Y. Poon, J. B. H. Tok, X. D. Chen, Z. N. Bao, Nature Electronics 2019, 2, 361.

[32] S. Zeadally, F. K. Shaikh, A. Talpur, Q. Z. Sheng, Renew Sust Energ Rev 2020, 128, 109901.

[33] F. Wen, T. Y. Y. He, H. C. Liu, H. Y. Chen, T. Zhang, C. K. Lee, Nano Energy 2020, 78, 105155.

[34] A. Raj, D. Steingart, J. Electrochem. Soc. 2018, 165, B3130.

[35] Z. L. Wang, Adv Mater 2012, 24, 280.

[36] J. G. Koomey, H. Scott Matthews, E. Williams, Annu Rev Environ Resour 2013, 38, 311.

[37] A. Whitmore, A. Agarwal, L. Da Xu, Inf Syst Front 2014, 17, 261.

[38] N. A. Kyeremateng, T. Brousse, D. Pech, Nature Nanotechnology 2017, 12, 7.

[39] P. Huang, C. Lethien, S. Pinaud, K. Brousse, R. Laloo, V. Turq, M. Respaud, A. Demortiere, B. Daffos, P. L. Taberna, B. Chaudret, Y. Gogotsi, P. Simon, Science 2016, 351, 691.

[40] X. L. Cheng, J. Pan, Y. Zhao, M. Liao, H. S. Peng, Adv Energy Mater. 2018, 8, 1702184.

[41] H. Dai, G. Zhang, D. Rawach, C. Fu, C. Wang, X. Liu, M. Dubois, C. Lai, S. Sun, Energy Storage Mater 2020.

[42] J. Le Bideau, L. Viau, A. Vioux, Chem Soc Rev 2011, 40, 907.

[43] A. Ferris, D. Bourrier, S. Garbarino, D. Guay, D. Pech, Small 2019, 15, e1901224.

[44] M. F. El-Kady, M. Ihns, M. Li, J. Y. Hwang, M. F. Mousavi, L. Chaney, A. T. Lech, R. B. Kaner, Proc Natl Acad Sci U S A 2015, 112, 4233.

[45] D. Pech, M. Brunet, P. L. Taberna, P. Simon, N. Fabre, F. Mesnilgrente, V. Conedera, H. Durou, J Power Sources 2010, 195, 1266.

[46] S. K. Xu, Y. Dall'Agnese, G. D. Wei, C. Zhang, Y. Gogotsi, W. Han, Nano Energy 2018, 50, 479.

[47] Z. Xiong, X. Yun, L. Qiu, Y. Sun, B. Tang, Z. He, J. Xiao, D. Chung, T. W. Ng, H. Yan, R. Zhang, X. Wang, D. Li, Adv Mater 2019, 31, e1804434.

[48] D. Pech, M. Brunet, H. Durou, P. Huang, V. Mochalin, Y. Gogotsi, P. L. Taberna, P. Simon, Nat Nanotechnol 2010, 5, 651.

[49] N. A. Kyeremateng, T. Brousse, D. Pech, Nat Nanotechnol 2017, 12, 7.

[50] J. Lin, Z. Peng, Y. Liu, F. Ruiz-Zepeda, R. Ye, E. L. Samuel, M. J. Yacaman, B. I. Yakobson, J. M. Tour, Nat Commun 2014, 5, 5714.

[51] J. B. In, B. Hsia, J.-H. Yoo, S. Hyun, C. Carraro, R. Maboudian, C. P. Grigoropoulos, Carbon 2015, 83, 144.

[52] M. Yuan, Z. P. Wang, Y. F. Rao, Y. Wang, B. Gao, J. B. Yu, H. Li, X. P. Chen, Carbon 2023, 202, 296.

[53] H. Liu, Z. Sun, Y. Chen, W. Zhang, X. Chen, C. P. Wong, ACS Nano 2022, 16, 10088.

[54] M. F. El-Kady, R. B. Kaner, Nat Commun 2013, 4, 1475.

[55] M. F. El-Kady, V. Strong, S. Dubin, R. B. Kaner, Science 2012, 335, 1326.

[56] W. Gao, N. Singh, L. Song, Z. Liu, A. L. Reddy, L. Ci, R. Vajtai, Q. Zhang, B. Wei, P. M. Ajayan, Nat Nanotechnol 2011, 6, 496.

[57] J. Chmiola, C. Largeot, P. L. Taberna, P. Simon, Y. Gogotsi, Science 2010, 328, 480.

[58] S. Wang, B. Hsia, C. Carraro, R. Maboudian, J. Mater. Chem. A 2014, 2, 7997.

[59] Z. Liu, S. Liu, R. Dong, S. Yang, H. Lu, A. Narita, X. Feng, K. Mullen, Small 2017, 13.

[60] J. H. Sung, S. J. Kim, K. H. Lee, J. Power Sources 2003, 124, 343.

[61] Q. C. He, J. J. Ye, Z. Y. Peng, Y. Y. Guo, L. C. Tan, Y. W. Chen, J. Power Sources 2021, 506, 230176.

[62] Z. Xia, V. Mishukova, S. Sollami Delekta, J. Sun, J. S. Sanchez, J. Li, V. Palermo, Nanoscale 2021, 13, 3285.

[63] X. Wang, B. D. Myers, J. Yan, G. Shekhawat, V. Dravid, P. S. Lee, Nanoscale 2013, 5, 4119.

[64] N. Kurra, M. K. Hota, H. N. Alshareef, Nano Energy 2015, 13, 500.

[65] Z. S. Wu, K. Parvez, S. Li, S. Yang, Z. Liu, S. Liu, X. Feng, K. Mullen, Adv Mater 2015, 27, 4054.

[66] C. Zhong, Y. Deng, W. Hu, J. Qiao, L. Zhang, J. Zhang, Chem Soc Rev 2015, 44, 7484.

[67] M. Sevilla, A. B. Fuertes, ACS Nano 2014, 8, 5069.

[68] S. Muroi, D. Iida, T. Tsuchikawa, N. Yabuuchi, R. Horikoshi, N. Hosono, D. Komatsu, S. Komaba, Electrochemistry 2015, 83, 609.

[69] P. X. Han, G. J. Xu, X. Q. Han, J. W. Zhao, X. H. Zhou, G. L. Cui, Adv. Energy Mater. 2018, 8, 1801243.

[70] M. Armand, F. Endres, D. R. MacFarlane, H. Ohno, B. Scrosati, Nat Mater 2009, 8, 621.

[71] T. Welton, Chem Rev 1999, 99, 2071.

[72] J. P. Hallett, T. Welton, Chem Rev 2011, 111, 3508.

[73] F. Endres, S. Zein El Abedin, Phys Chem Chem Phys 2006, 8, 2101.

[74] J. Chmiola, G. Yushin, Y. Gogotsi, C. Portet, P. Simon, P. L. Taberna, Science 2006, 313, 1760.

[75] C. Merlet, B. Rotenberg, P. A. Madden, P. L. Taberna, P. Simon, Y. Gogotsi, M. Salanne, Nat Mater 2012, 11, 306.

[76] M. V. Fedorov, A. A. Kornyshev, Chem Rev 2014, 114, 2978.

[77] P. Simon, Y. Gogotsi, Acc Chem Res 2013, 46, 1094.

[78] T. Stettner, A. Balducci, Energy Storage Mater 2021, 40, 402.

[79] Y. S. Ye, J. Rick, B. J. Hwang, J. Mater. Chem. A 2013, 1, 2719.

[80] M. Yoshizawa, W. Xu, C. A. Angell, J Am Chem Soc 2003, 125, 15411.

[81] J. P. Belieres, C. A. Angell, J Phys Chem B 2007, 111, 4926.

[82] K. Ueno, H. Tokuda, M. Watanabe, Phys Chem Chem Phys 2010, 12, 1649.

[83] B. Asbani, C. Douard, T. Brousse, J. Le Bideau, Energy Storage Mater 2019, 21, 439.

[84] N. Chen, H. Q. Zhang, L. Li, R. J. Chen, S. J. Guo, Adv. Energy Mater. 2018, 8, 1702675.

[85] D. M. Correia, L. C. Fernandes, P. M. Martins, C. Garcia-Astrain, C. M. Costa, J. Reguera, S. Lanceros-Mendez, Adv Funct Mater 2020, 30, 1909736.

[86] S. R. Madhvapathy, Y. J. Ma, M. Patel, S. Krishnan, C. Wei, Y. J. Li, S. Xu, X. Feng, Y. G. Huang, J. A. Rogers, Adv Funct Mater 2018, 28, 1802083.

[87] C. Ni, in *Encyclopedia of Tribology*, (Eds: Q. J. Wang, Y.-W. Chung), Springer US, Boston, MA 2013, 2977.

[88] Z. Lyu, L. Yao, W. Chen, F. C. Kalutantirige, Q. Chen, Chem Rev 2023.

[89] Q. Chen, C. Dwyer, G. Sheng, C. Zhu, X. Li, C. Zheng, Y. Zhu, Adv Mater 2020, 32, e1907619.

[90] D. Shindo, T. Oikawa, in *Analytical Electron Microscopy for Materials Science*, (Eds: D. Shindo, T. Oikawa), Springer Japan, Tokyo 2002, 81.

[91] A. A. Bunaciu, E. G. Udristioiu, H. Y. Aboul-Enein, Crit Rev Anal Chem 2015, 45, 289.

[92] C. S. Fadley, J. Electron Spectrosc. Relat. Phenom. 2010, 178, 2.

[93] X. H. Wang, M. Salari, D. E. Jiang, J. C. Varela, B. Anasori, D. J. Wesolowski, S. Dai, M. W. Grinstaff, Y. Gogotsi, Nat Rev Mater 2020, 5, 787.

[94] A. M. O'Mahony, D. S. Silvester, L. Aldous, C. Hardacre, R. G. Compton, J. Chem. Eng. Data 2008, 53, 2884.

[95] L. S. Garca-Coln, L. F. del Castillo, P. Goldstein, Phys Rev B Condens Matter 1989, 40, 7040.

[96] C. A. Angell, N. Byrne, J. P. Belieres, Acc Chem Res 2007, 40, 1228.

[97] W. Xu, E. I. Cooper, C. A. Angell, The J. Phys. Chem. B. 2003, 107, 6170.

[98] N. Elgrishi, K. J. Rountree, B. D. McCarthy, E. S. Rountree, T. T. Eisenhart, J. L. Dempsey, J. Chem. Educ. 2018, 95, 197.

[99] S. L. Zhang, N. Pan, Adv. Energy Mater. 2015, 5, 1401401.

[100] B. E. Conway, V. Birss, J. Wojtowicz, J Power Sources 1997, 66, 1.

[101] P. L. Taberna, P. Simon, J. F. Fauvarque, J. Electrochem. Soc. 2003, 150, A292.

[102] A. R. C. Bredar, A. L. Chown, A. R. Burton, B. H. Farnum, ACS Appl. Energy Mater. 2020, 3, 66.

[103] V. Vivier, M. E. Orazem, Chem Rev 2022, 122, 11131.

[104] T. S. Mathis, N. Kurra, X. H. Wang, D. Pinto, P. Simon, Y. Gogotsi, Adv. Energy Mater. 2019, 9, 1902007.

[105] J. R. Miller, R. A. Outlaw, B. C. Holloway, Science 2010, 329, 1637.

[106] D. Rochefort, A. L. Pont, Electrochem Commun 2006, 8, 1539.

[107] L. Mayrand-Provencher, D. Rochefort, J Phys Chem C 2009, 113, 1632.

[108] L. Mayrand-Provencher, S. Lin, D. Lazzerini, D. Rochefort, J Power Sources 2010, 195, 5114.

[109] J. S. Seenath, D. Pech, D. Rochefort, J Power Sources 2022, 548, 232040.

Chapter 2 RuO_2 Micro SCs using Protic Ionic Liquids

2.1 Microfabrication

The basic architecture of a miniaturized supercapacitor consists of a positive and a negative along with an ionic conducting electrolyte. To realize on-chip micro-supercapacitors having a planar configuration and footprint area under 1 cm^2 for application in microelectronics, various strategies have been investigated so far. The key challenge is to obtain micro-size patterned electrodes devoid of any short-circuiting issues [1]. This has to be addressed through the fabrication method compatible with the ones used in the semiconductor industry for the facile co-integration with other electronic components. Importantly, the fabrication method will also determine the resolution of the pattern (minimum distance between the adjacent electrodes for an interdigitated configuration, which can range from 500 μm down to 5 μm) [1].

2.1.1 Current Collector patterning

The current collector is one of the significant and indispensable constituents of an energy storage device, which acts as a necessary support for the electrode materials and plays an important role as a linker between the external circuit and the electrode. In addition to playing a vital role in collecting and conducting electrons, the current collectors can also influence the rate performance of supercapacitors depending on the compatibility with the electrode material and its conductivity properties [2]. Depending on the surface and mechanical properties of the current collectors used, the active material can be loaded either by coating, pressing, or other forms of deposition methods.

Several approaches have been developed to fabricate planar MSCs devices with interdigitated patterns. In this work, we followed the photolithography technique to develop the

interdigitated structure of planar MSCs, followed by depositing the appropriate electrode materials and choosing the right combination of electrolytes.

Photolithography is a well-known technology widely used to fabricate micro-nanodevices owing to its compatibility with conventional semiconductor manufacturing technologies offering high-resolution patterns [3]. To generate micro-supercapacitor interdigitated current collectors, a Ti(100 nm)/Au(300 nm) thin layer was first patterned onto an oxidized silicon wafer using conventional photolithography and lift-off techniques **(Figure 2.1)**. In short, a layer of positive photoresist was spin-coated on the wafer and exposed to the UV light through a designed photomask containing the interdigitated pattern and treated under a developer solution. Afterward, the substrate was subjected to etching treatment in a KI + I_2 solution (etching of gold layer) and then in 5 % hydrofluoric acid buffer solution (etching of titanium layer). Finally, the photoresist was removed by the treatment with acetone.

Using photolithography technology, a highly conductive current collector pattern can be realized, and this makes the resulting MSC device with low equivalent internal series resistance. The active material can be directly electrodeposited on this current collector substrates. After that, MSC device can be obtained by dropping the appropriate electrolyte candidate. In a nutshell, photolithography technology can produce high-performance MSCs devices while ensuring the high accuracy of various electrode patterns.

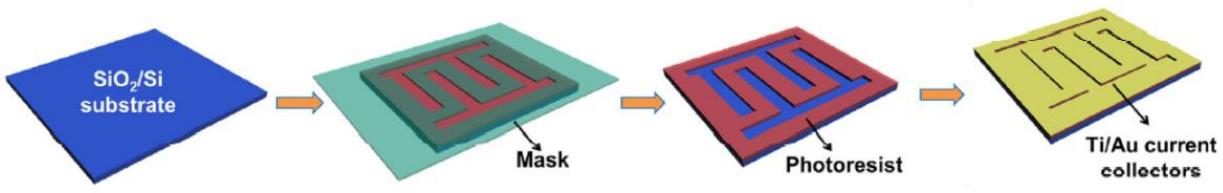

Figure 2.1: Schematic illustration of the fabrication process for on-chip MSCs [4].

2.1.2 Electrodeposition of RuO_2

In order to deposit the active material on the current collector, an interdigitated Ti(100 nm)/Au(300 nm) thin layer supported silicon wafer was electrochemically pretreated by cycling between -0.3 and +1.7 V versus saturated calomel electrode (SCE) in 1 M H_2SO_4 at a scan rate of 100 mV s^{-1} until a stable voltammogram was obtained. The typical dimensions of the interdigitated electrodes are provided in **Table 2.1**. The total geometrical active surface area of the electrodes is 0.25 cm^2. Electrodeposition of hydrous RuO_2 onto the interdigitated porous Au was done by cycling the electrodes between -0.3 and +0.95 V versus SCE at 50 mV s^{-1} for 300 cycles in a solution of 0.01 M $RuCl_3.xH_2O$ in 0.2 M KCl-HCl buffer medium. The electrode was then annealed at 150 °C for 1 h.

Dimensions	
Finger width (µm)	500
Finger length (µm)	4000
Interspace (µm)	500
Surface area (cm^2)	0.25

Table 2.1: Dimensions of the interdigitated micro-supercapacitor electrodes.

To characterize the electrochemically deposited hydrous ruthenium oxide on interdigitated flat Au substrates **(Figure 2.2)**, we took help from different morphological and structural characterization techniques.

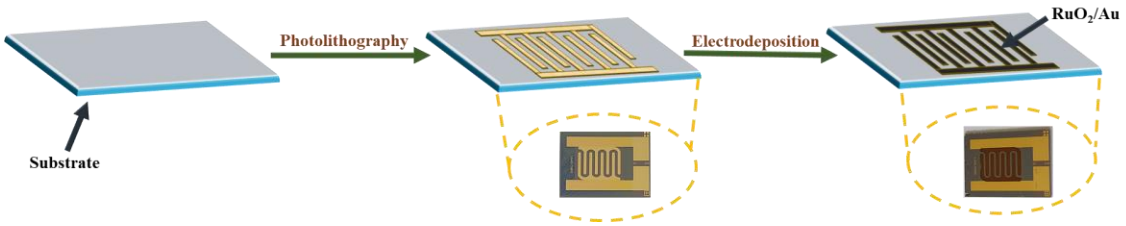

Figure 2.2: Schematic of realizing interdigitated Au substrates and the deposition of RuO_2 with photographs of the device.

The successful deposition of the active material has been confirmed using scanning electron microscopy (SEM) and Energy-dispersive X-ray spectroscopy (EDS) elemental mapping **(Figure 2.3)**. The uniform deposition along with a clean interspace between the fingers is inevitable for the prevention of short-circuiting issues during the actual operation of the device. It is noteworthy that the electrodeposition technique is a viable and scalable route concerning the commercial microfabrication process.

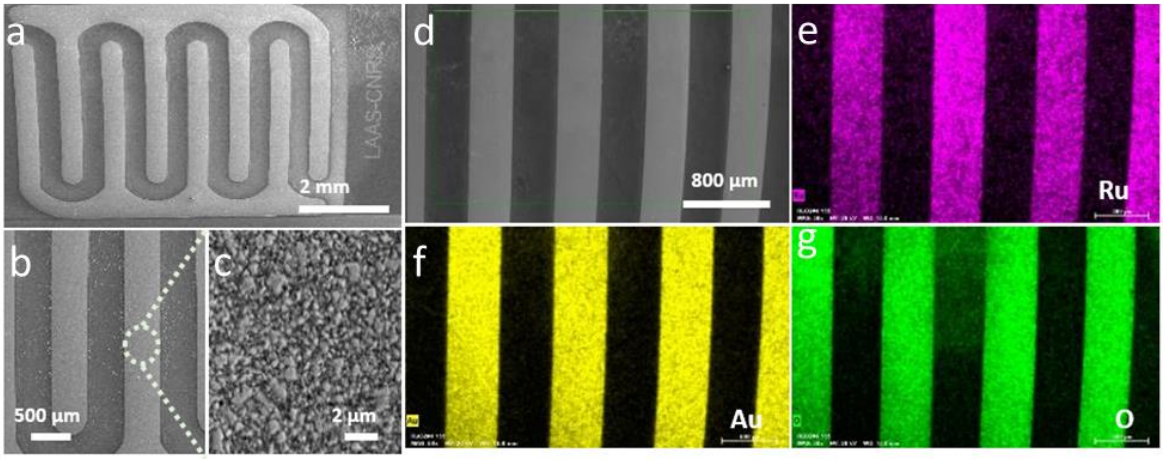

Figure 2.3: SEM images at different magnifications (a-d). EDS elemental mapping of RuO_2 deposited on interdigitated flat Au current collector (e-g).

2.2 Protic Ionic Liquids (PILs)

Protic ionic liquids, a subclass of ionic liquids and a potential non-aqueous electrolyte alternative able to exchange H^+ with RuO_2, hence promoting surface redox reactions while affording a wider ESW [5]. Rochefort *et al.* first successfully demonstrated the presence on occurrence of pseudocapacitance in RuO_2 using PILs and the capacitance reported is comparable to the aqueous electrolyte [6]. Lindberg *et al.* recently showed that proton availability influences the electrochemical response in MnO_2 electrode, where only the acidic proton of PILs can induce reversible redox reactions while protons attached to aprotic ionic liquids (AILs), e.g., in hydroxy groups fail to bring about any faradaic contribution [7]. Recent reports are suggesting that PILs can be also used in combination with conducting polymers and transition metal nitride-based electrodes [8]. It is known that compared to aqueous electrolytes, PILs display higher viscosity with slower H^+ transfer and it remains to be determined if this is a limiting issue in MSCs. Moreover, as they share the same properties as aprotic ILs, PILs can help to overcome other major challenges associated with currently used electrolytes such as evaporation and encapsulation issues of aqueous-based and flammability of common organic electrolytes [9].

The structure of the PILs investigated in our current study on RuO_2 MSCs is shown in **Figure 2.4**. The choice of these electrolyte candidates is based on their physicochemical properties with a range of commonly available structures that are easier to synthesize and remain stable under normal operational conditions [10, 11]. It is important to mention that few of these selected structures of PILs are already reported for conventional supercapacitors using metal-oxide electrodes or their aprotic analogs are used for EDLC-based electrodes [6, 12, 13, 14]. The key properties of PILs that are desirable for energy storage include high ionicity (large Δ pKa between the constituents), high ionic conductivity/lower viscosity, and wide stability windows. For instance, while pyrrolidinium or alkyl ammonium-based PILs can provide a wide stability window, the PIL composed of a

pyridine-based cation and trifluoroacetic acid anion can render high ionicity due to their large pKa difference [11, 12, 14, 15].

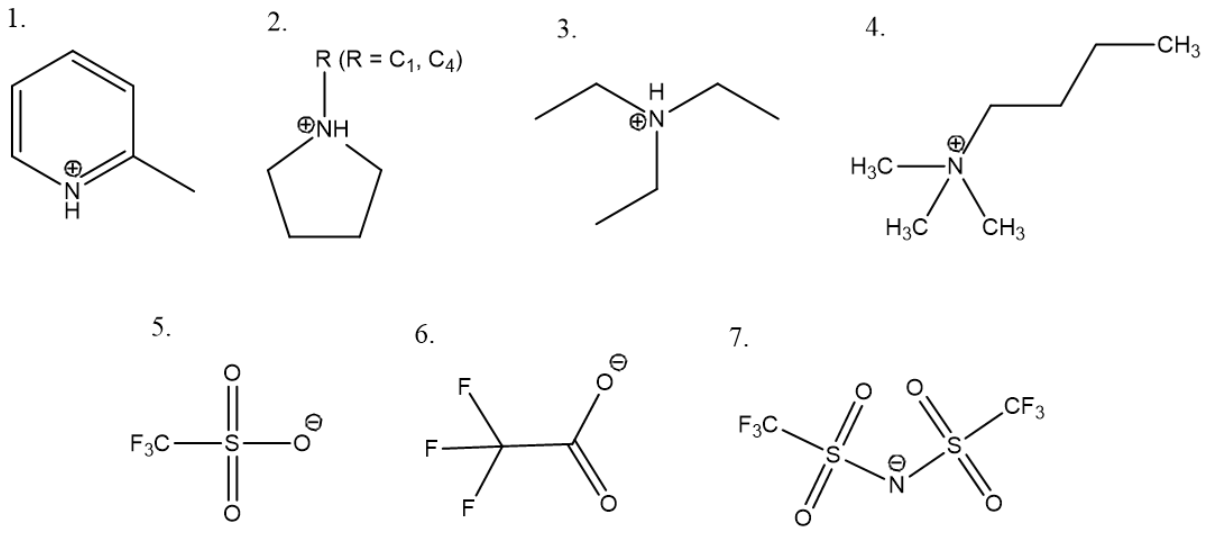

Figure 2.4: Structures of the cation and anion groups of ionic liquid candidates explored for RuO_2 MSCs (1. 2-MePy = 2-methyl pyridinium, 2. Pyr_{1H} = 1-methyl pyrrolidinium, Pyr_{4H} = 1-butyl pyrrolidinium, 3. TEAH = triethylammonium, 4. BTMA = butyl-trimethyl ammonium, 5. Tf = trifluromethanesulfonate, 6. TFA = trifluoroacetate, 7. TFSI = bis(trifluoromethane sulfonyl)imide).

All the PILs were prepared by the slow addition of the equimolar amount of acid into each respective base while stirring in an ice bath to avoid the decomposition from the exothermic reaction. To remove trace amounts of water from the precursor or atmosphere, the mixtures were then heated at 60 °C for 24 h under a vacuum. The vials containing PIL samples were sealed and kept in the glove box under argon atmosphere for the measurements. Water content was measured using Karl Fisher titration. Among the PILs, TEAH/TFSI had a lower water content of below ca. 500 ppm and Pyr_{4H}/TFA had a higher water content of >1000 ppm. The rest of the PILs showed a water content between 500 to 1000 ppm.

The physicochemical properties including the viscosity, density, and ionic conductivity values measured for the protic ionic liquids are provided in **Table 2.2**. To evaluate how the conductivity affects the electrochemical response of the MSC, the temperature dependence of ionic

conductivity is represented using the Arrhenius plot (**Figure 2.5)** The conductivity strongly depends on the ion-ion interaction and in PILs, hydrogen bonding also plays a role in the intermolecular interactions [16]. The Pyr_{4H}/TFA showed an ideal fit in the Arrhenius plot at all temperatures, which we believe could stem from the higher water content (>1000 ppm) as it can disrupt the strong ion interactions in the PIL. On the other hand, both TEAH/TFSI and 2-MePy/TFA showed curvature deviation at lower temperatures. For such systems, the Vogel–Tamman–Fulcher (VTF) fit is used to describe the ion conduction behavior, which implies the increase in temperature is not entirely resulting in increased ion mobility.

Electrolyte	η (RT) (cP)	ρ (RT) (g cm^{-3})	σ (RT) (mS cm^{-1})
2Me.Py-TFA	13.4	1.42	12.6
Pyr_{4H}-TFA	32.9	1.14	1.63
TEAH-TFSI	51.7	1.43	3.27

Table 2.2. Physicochemical properties of the studied protic ionic liquids.

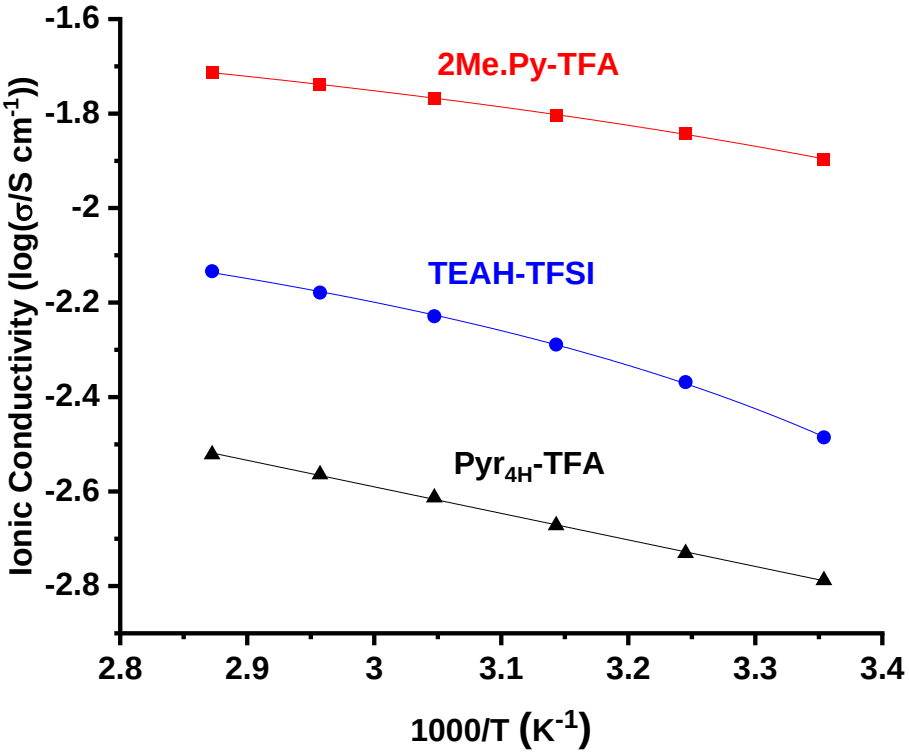

Figure 2.5: Arrhenius plots for the PILs with measurements done at an interval of 10°C from 25 to 75°C.

The Walden plot gives a qualitative analysis of the ionicity of PILs by comparing ionicity and equivalent conductivity values, which help us to understand the proton transfer property of PILs. An ionic liquid of "good" quality lies in proximity to the ideal line and those of poor quality will be lower than this line as described by Angell and co-workers [17]. The data corresponding to 0.5 M H_2SO_4 will appear above the ideal line owing to the Grotthus transport mechanism that is well-known in the literature [18]. The 2-MePy/TFA showed a value exactly on the reference KCl (**Figure 2.6)**, indicating a good ionicity, which is in accordance with some of the earlier reports of using 2-MePy/TFA where a large Δ pKa between the constituents granted a higher ionicity without forming a neutral species and losses by volatilization during the heating step [12]. Both TEAH/TFSI and Pyr_{4H}/TFA are positioned slightly below and closer to the ideal line with slight ion pairing in the latter as is expected from PILs, where charge transport occurs via a vehicle-type mechanism. Overall, the conductivity values of investigated PILs occupy the region of good ionic liquids in the Walden plot and are comparable to most of the PILs reported in the literature.

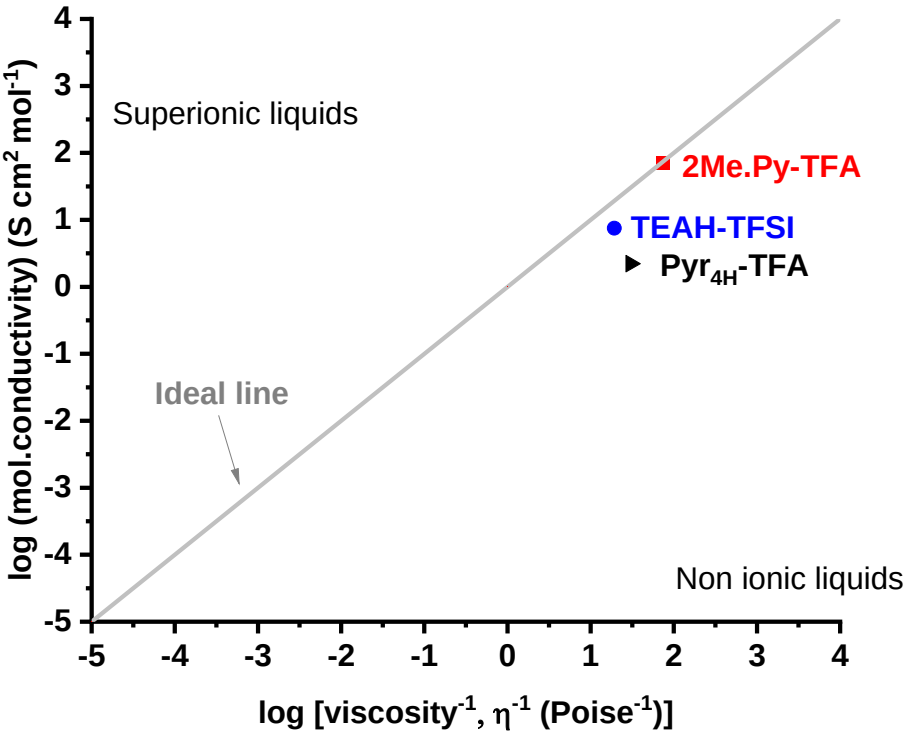

Figure 2.6: Walden plot that compares the ionicity and equivalent conductivity values of PILs.

2.3 Electrochemical study of RuO_2 Micro-supercapacitor using PILs

Our next goal was to determine the electrochemical window of RuO_2 MSC in these electrolytes. To achieve this, we run cyclic voltammetry (CV) scanning starting at open circuit potential to a point where irreversibility due to electrolyte oxidation and electrode damage become conspicuous. To have a better differentiation with the standard 0.5 M H_2SO_4 electrolyte, a comparison of the CVs of RuO_2 MSCs between 0 and 1 V using different PILs as well as in the aqueous electrolyte is shown in **Figure 2.7 a**. Although a higher current density is achieved with the aqueous acidic electrolyte due to faster redox kinetics and efficient utilization of active sites, the ESW is limited to *ca.* 1 V owing to the thermodynamic decomposition limit of water. It should be noted that among the synthesized PILs, 2-MePy/Tf and Pyr_{1H}/TFA remained in the solid or semi-solid form, therefore it is required to use an organic solvent and aprotic ionic-liquid medium

for their dilution and to use them as liquid electrolyte for the electrochemical characterization. **Figure 2.7 b** shows the normalized CVs (the current, *I*, has been normalized by the scan rate, *s*, and capacitance, *C*) of RuO_2 MSCs tested using PILs at their maximum cell voltage (1.1 V for 2-MePy/Tf and 1.5 V for the rest of the PILs (2-MePy/TFA, Pyr_{1H}/TFA, Pyr_{4H}/TFA, and TEAH/TFSI)). The CV curves showed pseudo rectangular shapes showing the pseudocapacitive charge transfer between PIL and RuO_2 beyond the thermodynamic stability window of conventional aqueous electrolytes.

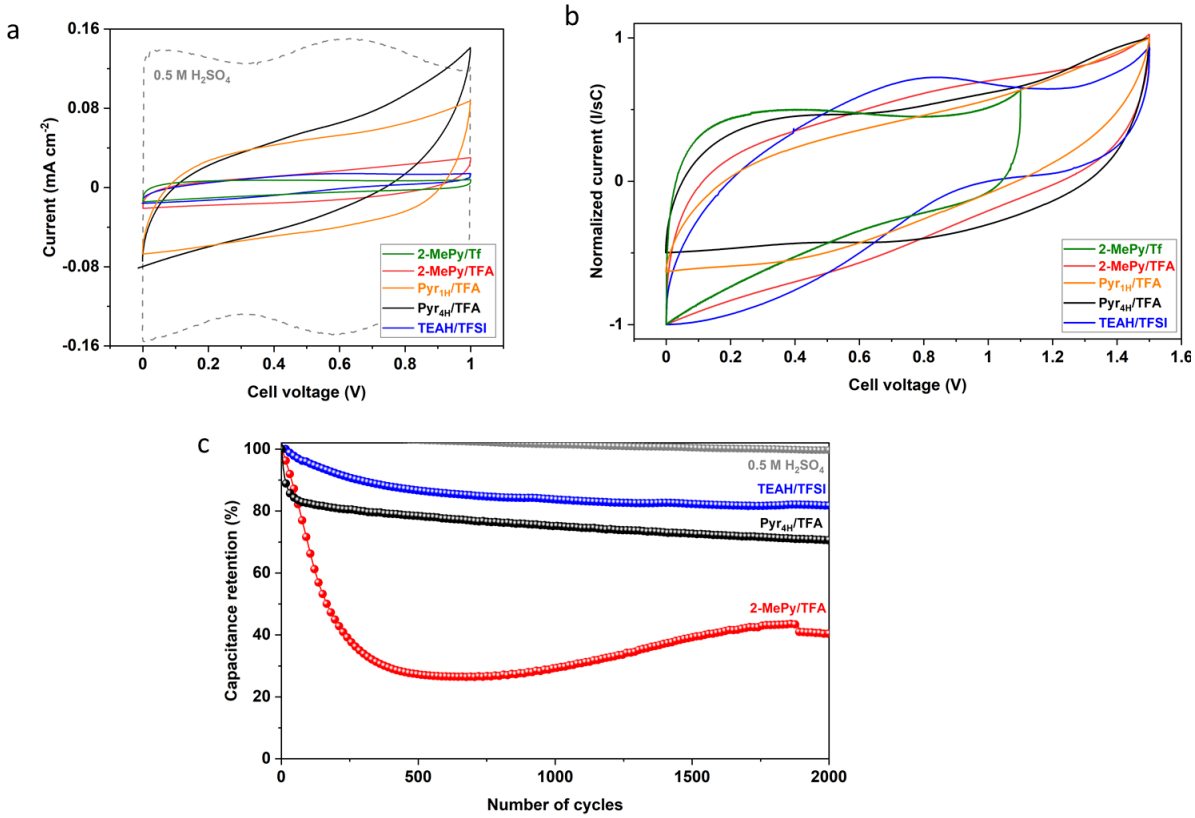

Figure 2.7: a. Cyclic voltammetry (CV) curves of RuO_2 on interdigitated flat Au substrates tested in different PILs and their comparison with 0.5 M H_2SO_4 (scan rate of 100 mV s^{-1}); b. Normalized CVs of RuO_2 in PILs at a scan rate of 100 mV s^{-1}; c. Cycling stability performance of RuO_2 MSCs in different electrolytes at 1 mA cm^{-2}.

To provide a comparison of the impact of the maximum voltage across the electrolytes used, the CV curve of RuO_2 MSC using 0.5 M H_2SO_4 up to 1.5 V is shown in **Figure 2.8.** A large current onset at 1.1 V corresponds to the irreversible oxidation of water.

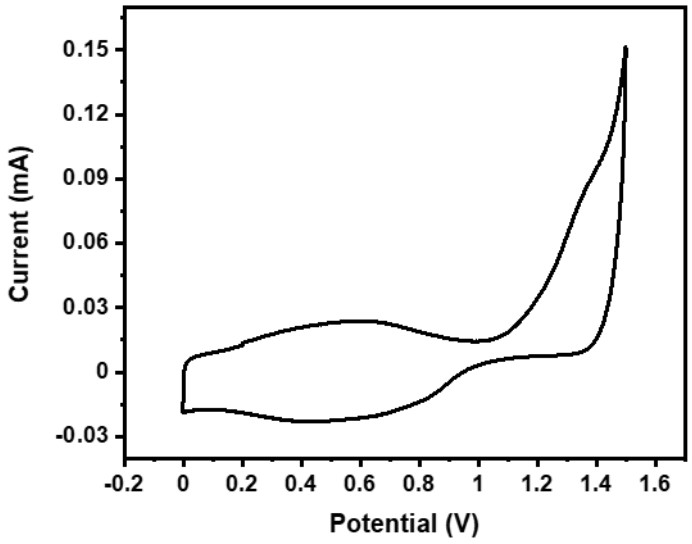

Figure 2.8: CV curve of RuO_2 on interdigitated flat Au substrate in 0.5 M H_2SO_4 at 100 mV s^{-1}.

Next, we performed cycling of the electrodes in all these electrolytes as long-term cycling is a key requisite for the practical application of MSCs. Despite a higher ionic conductivity, 2-MePy/TFA showed lower cyclability with a sharp capacitance drop up to *ca.* 500 cycles which remained stable afterward (**Figure 2.7 c)**. This can be ascribed to the significant damage happening to the RuO_2 electrode during the charge-discharge cycles and the active material dissolution in the electrolyte. The changes in the Ru metallic state after cycling in 2-MePy/TFA were further confirmed using XPS analysis of the electrodes before and after the long cycling **(Figure 2.9 & 2.10 b)**, which showed a major reduction in the Ru 3p signal which is ascribed to the degradation of the active material, RuO_2. On the other hand, TEAH/TFSI showed better long-term cycling stability with RuO_2, where the Ru 3p signals obtained from XPS remained intact **(Figure 2.10 a)**.

Provided the high ionicity, stability window, and long-term cyclability of TEAH/TFSI, we decided to perform further detailed electrochemical studies using this particular PIL.

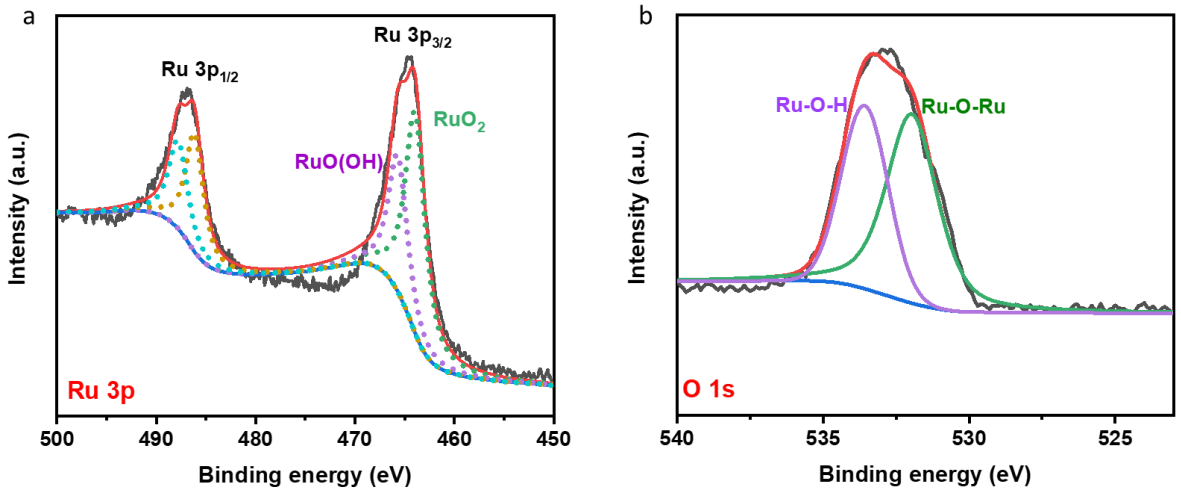

Figure 2.9: a. XPS Ru 3p and b. O 1s spectra of electrodeposited hydrous RuO_2 ($RuO_2.xH_2O$) electrode.

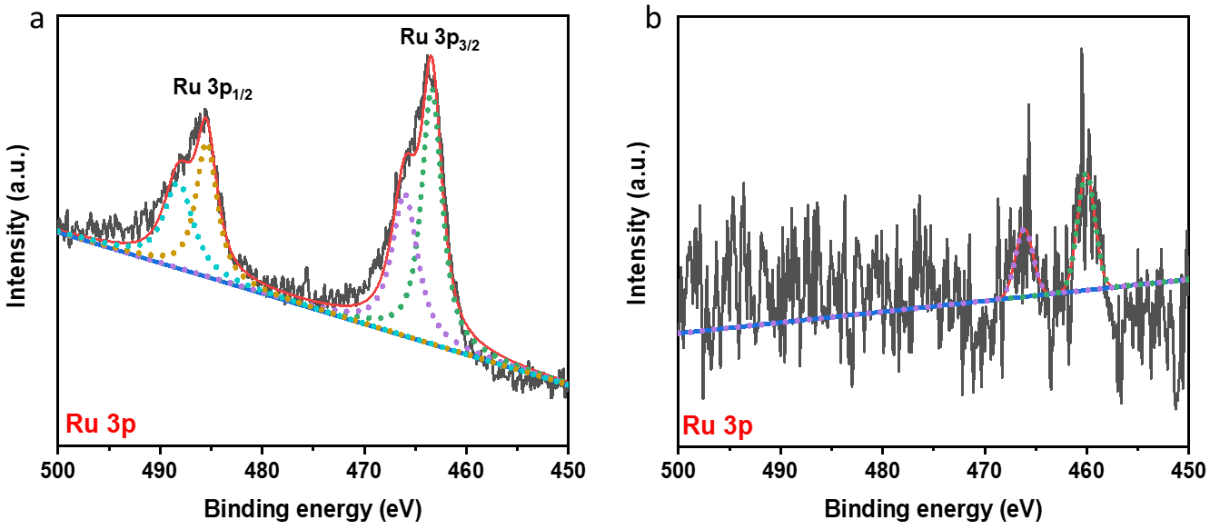

Figure 2.10: XPS Ru 3p spectra of RuO_2 electrodes after cycling in a. TEAH/TFSI and b. in 2MePy/TFA.

2.4 Impact of SiWa on PIL-based RuO_2 Micro-supercapacitor

2.4.1 Silicotungstic acid (SiWa)

Although PILs can exchange protons at the RuO_2 electrode surface, the lack of swift proton (H^+) transportability due to vehicle-type charge transport limits the rate performance [16, 19]. To address this issue, we decided to dope TEAH/TFSI with a solid ionic conductor of H^+, silicotungstic acid (SiWa, $H_4SiW_{12}O_{40}$) and monitored the change in the current response and voltage window. The SiWa belongs to the family of heteropolyacids, which are hydrous salts exhibiting high solubility in water and many organic solvents along with a high proton conductivity (e.g. 0.027 S cm^{-1} for $SiWa.28H_2O$) at room temperature. This can be ascribed to hydrogen-bonded conduction pathways in the crystal lattice originating from a large number of crystallized water molecules in the crystal hydrate and the dynamic dissociation of co-crystallized water molecules in the crystal hydrate via interactions with oxygen atoms of the Keggin anion **(Figure 2.11)**, which increases the density of free protons [20]. The protons, in the forms of H^+-nH_2O clusters (e.g. H_3O^+or $H_5O_2^+$), are transferred by hopping from H^+-nH_2O donor sites to nH_2O acceptors in the HPA to give rise to high proton conductivity.

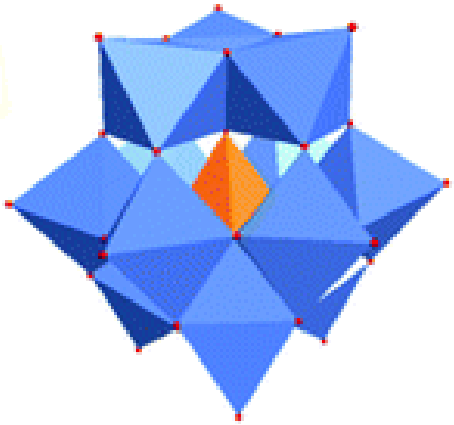

Figure 2.11: Polyhedral illustration of Polyoxometalate (POM) Keggin anion $[XM_{12}O_{40}]^{n-}$. The central $[XO_4]$ heteroatom units (shown in orange) are surrounded by a $[MO_x]_n$ addenda atom cage. [21]

2.4.2 Electrochemical Performance using SiWa-doped PIL

In our previous report, we successfully demonstrated the impact of SiWa with an aprotic ionic liquid electrolyte and the pseudocapacitive current enhancement using $RuO_xN_yS_z$ electrodes [22]. The study of SiWa with PILs has never been done before and it would be interesting to explore the compatibility and electrochemical behavior in comparison to an aprotic ionic liquid of a similar structure as TEAH/TFSI. The CV study revealed a huge enhancement in the pseudocapacitive current response in SiWa-doped butyl-trimethyl ammonium trifluoromethane sulfonyl imide (BTMA/TFSI), the aprotic analogue chosen for the study (**Figure 2.12 a)**, showing SiWa provided freely available H^+ ions to promote the surface redox reactions with RuO_2 which previously only had a double-layer contribution. On the other hand, in the protic IL, TEAH/TFSI, the SiWa accelerated the charge transport as evidenced by the rise in the current values owing to a combined Grotthus (from SiWa) and vehicle-type (from TEAH/TFSI) transport **(Figure 2.12 b)**. These findings clearly demonstrate the importance of proton conducting additives in achieving accelerated faradaic current response with RuO_2 electrodes.

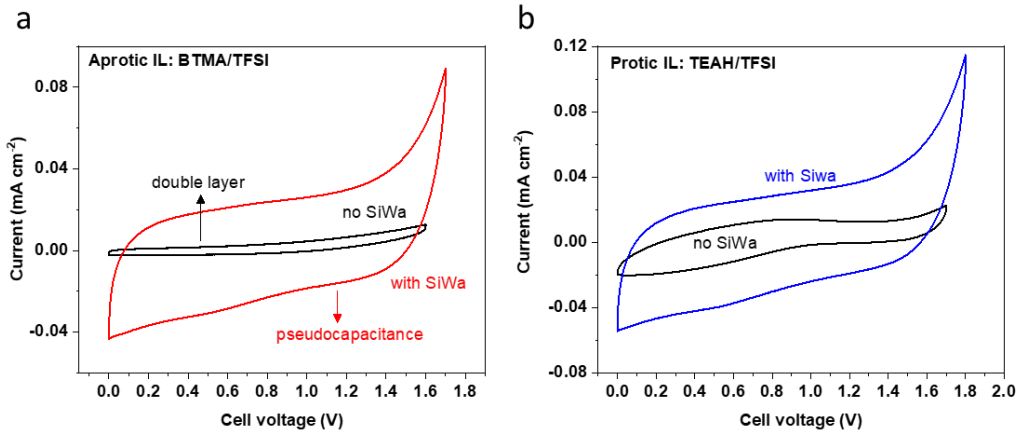

Figure 2.12: Capacitive behavior of protic and aprotic IL based on TFSI anion for RuO_2 MSCs using flat substrate in ILs with SiWa doping (10 wt%). a. CV curves (100 mV s^{-1}) in an aprotic ionic-liquid, butyl-trimethyl ammonium trifluoromethane sulfonyl imide (BTMA/TFSI) before and after SiWa doping; b. CV curves using TEAH/TFSI before and after SiWa doping.

2.5 Electrochemical study of RuO_2 on 3D substrates

To demonstrate the practical viability of MSCs, developing high roughness current collectors having high electrochemically active surface area while keeping the limited footprint space available is imperative. An advanced three-dimensional (3D) microelectrode architecture design offers enormous opportunities due to the high mass loading of active materials, large specific surface areas, fast ion diffusion kinetics, and short electron transport pathways. However, the current 3D electrode architectures depend on expensive and complex fabrication techniques, such as conventional lithography and colloidal templating methods, which are not feasible considering the large-scale and shape-conformable fabrication of 3D microelectrodes. [23] Also, it is vital to control the thickness, composition, porosity, and homogeneity of the 3D microelectrodes, as well as to develop scalable microfabrication routes.

2.5.1 Dynamic Hydrogen Bubble Template (DHBT)

The dynamic hydrogen bubble template method is a one-step electrodeposition technique at high current density under a 3-phase interface, where hydrogen bubbles serve as a template for the cathodic deposition of metals [24], [25]. Under extreme overpotential, the acidic bath solution containing the electrolyte ions breakdown into hydrogen bubbles. [26]

During the electrolysis reaction, hydrogen reduction occurs at the cathode, which initiates the nucleation of the hydrogen bubbles over the cathode. When the reaction proceeds, the following reduction phenomenon's take place concomitantly.

$$M^{n+}_{(aq)} + ne^- \longrightarrow M_{(S)} \qquad (1)$$

$$2H^+_{(aq)} + 2e^- \longrightarrow H_{2(g)} \qquad (2)$$

This co-reduction process causes H_2 bubble nucleation over the cathode surface and concurrently metal ions gets reduce and deposit over the H_2 bubble. The bubble formation dynamics involve three steps, i.e., nucleation, growth, and detachment (shown in **Figure 2.13 a**). Tiny H_2 bubbles are generated at the nucleation stage, hence most of the metal gets reduce over the cathode, and with time microbubbles grow by joining the nearest bubbles and attaining a critical size, and bubbles adhere to the cathode surface coalesce. At this stage, the reduction of metal happens over the surface of H_2 bubbles by blocking the surface sites of the cathode. Hence, the two-phase interface starts to change into the three-phase interface. [27] In the end, these bubbles get remove from the cathode by leaving a porous morphological footprint of the metal. The detailed mechanism is shown in **Figure 2.13 b**. Due to an increase in the bubble diameter, the pore size of the film is increased towards the outer surface. Importantly, bubble formation and growth play a crucial role in deciding the final morphology of the 3D structure. The formation of a 3D structure depends on several factors such as electrolyte concentration, pH, temperature, applied current, and hydrogen evolution kinetics.

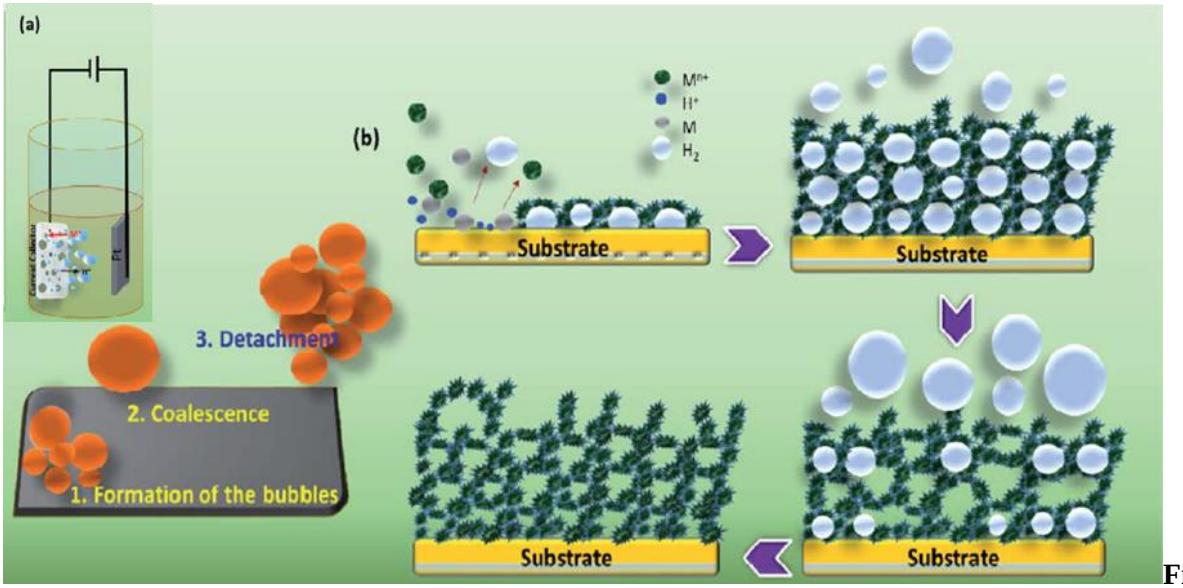

Figure 2.13: Schematic representation of the formation process of a 3D porous structure via DHBT method; (a) experimental set-up and (b) formation process [27].

The DHBT has not only a simple formation mechanism but an affordable cost, facile control over the structure, mechanical stability, etc. makes this technique very attractive especially for applications where such templates can act as a current collector. The 3D porous substrate derived from the DHBT route provides ample surface to promote the deposition of electroactive material with high mass loading and high electrical conductivity [28]. In addition, the metallic current collectors are fully covered with electroactive materials, so the chances of the substrate's contribution to the charge storage are almost negligible. [29]

Similar to our previous reports [22, 30, 31], we prepared high surface area interdigitated Au current collectors through the dynamic hydrogen bubble template (DHBT) method. The typical interconnected highly porous gold current collector containing RuO_2 deposits is revealed from the SEM image **(Figure 2.14).** The thickness of the porous electrodes after the RuO_2 deposition is ca. 20 μm.

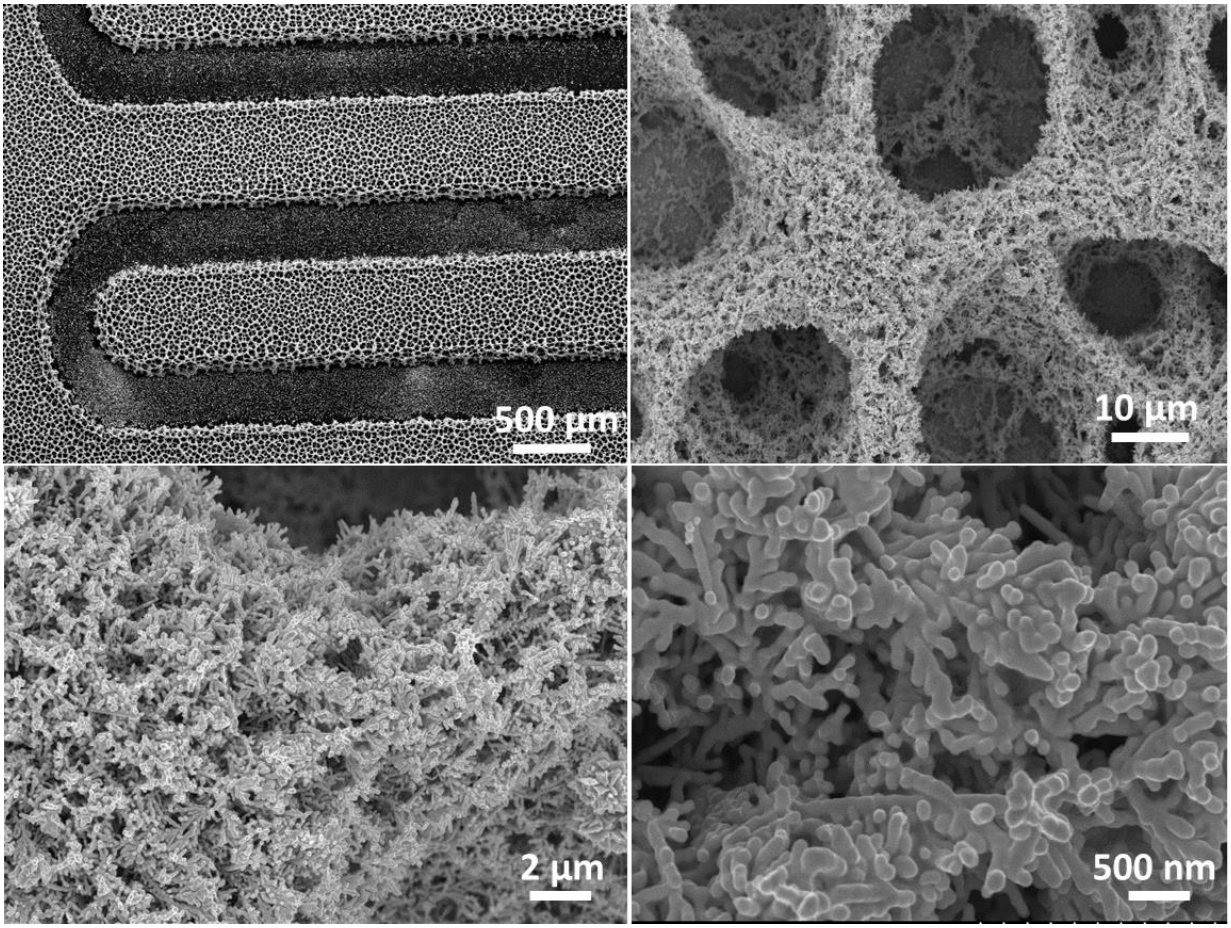

Figure 2.14: Scanning electron microscopy (SEM) images at different magnifications of DHBT Au substrate after RuO_2 deposition.

2.5.2 Electrochemical Performance using DHBT Substrates

A comparison of the CV curves of the RuO_2 electrodes tested in TEAH/TFSI and TEAH/TFSI + SiWa electrolytes is shown in **Figure 2.15**. A distinguishable gain in the current density is observed using SiWa doped electrolyte with redox peaks that appeared conspicuous, which reveals proton abundance in the electrolyte and facile transfer of H^+ at the RuO_2, promoting the surface-controlled faradaic process. Importantly, going from flat to high roughness Au substrates showed a higher cell voltage primarily because of a higher resistance coming from DHBT substrates with increased electrode thickness.

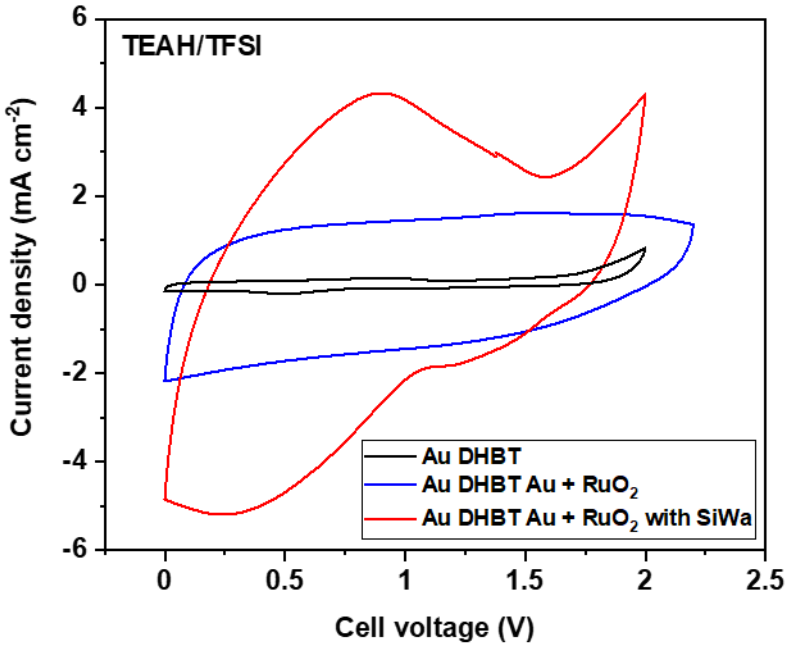

Figure 2.15: Comparison of the CVs of the MSC with the bare DHBT Au and after RuO_2 deposition at a scan rate of 100 mV s^{-1}.

The CV curves at different scan rates showed reversibility of the redox reactions with a raise in the current upon an increase in the scan rate **(Figure 2.16 a)**. The galvanostatic charge-discharge (GCD) curves at various current densities showed a non-linear shape typical for pseudocapacitive materials with long discharge times **(Figure 2.16 b)**.

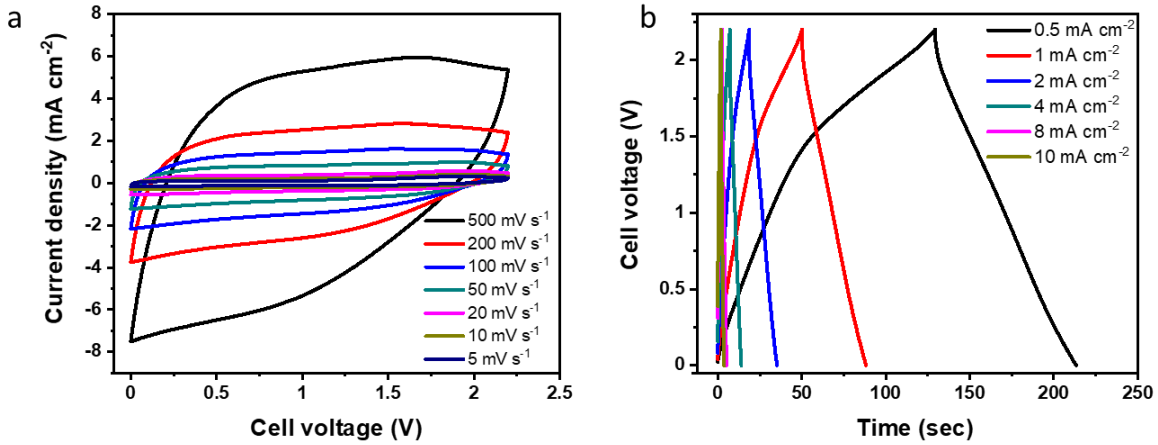

Figure 2.16: a. CV curves at different scan rates and b. GCD curves at different current densities of porous RuO_2 MSC tested using TEAH/TFSI electrolyte.

It's noteworthy that the charge accessibility of RuO_2 using PILs might behave differently in comparison with aqueous electrolytes on account of their viscous nature in combination with a highly porous substrate and we might have a significant fraction of active material not participating. To evaluate this, we used the method proposed by Trasatti *et al*., by calculating the outer charge (q_o) and total charge (q_t) as it is often used for RuO_2 materials [32] **(Figure 2.17 a)**. The q_o and q_t analysis of the electrode is done by plotting voltammetric charge q^* as a function of the sweep rate, v. Compared to the results from RuO_2 tested in aqueous 0.5 M H_2SO_4 electrolyte [31], PIL showed a lower q_o contribution (13%), which could be attributed to the larger size of the cations and anions in PILs making it difficult to access the densely connected pores lowering the charge storage kinetics. We strongly believe that this issue can be well addressed in the future with a better understanding of the underlying charge storage mechanism and rational designing of the current collectors offering better charge accessibility and efficient utilization of the active sites. Further, to unveil the change in electrolyte resistance in different substrates, the Nyquist plots correspond to RuO_2 MSCs tested in the same electrolyte with interdigitated flat *vs.* DHBT Au substrate configurations are acquired and shown in **Figure 2.17 b**. A low equivalent series resistance (ESR) of *ca.* 23.8 Ω cm^2 is obtained for porous RuO_2 MSC using SiWa-doped TEAH/TFSI with a near-vertical straight line in the low-frequency region indicating an ideal capacitive behavior.

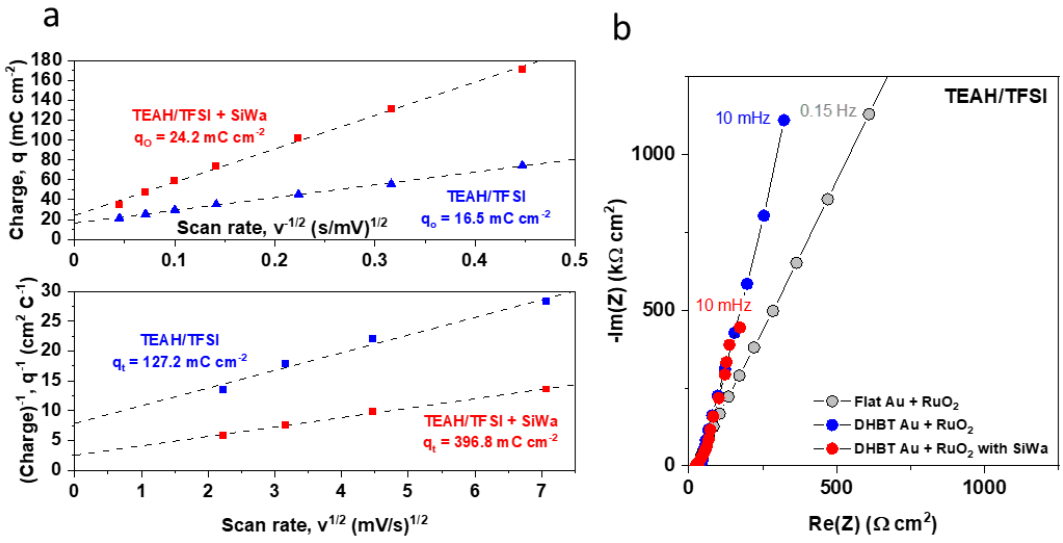

Figure 2.17: a. Determination of the outer charge (q_o) and total charge (q_t) of the electrode obtained by calculating the voltammetric charge, q*, as a function of the sweep rate, v.; b. Comparison of Nyquist plots of RuO_2 deposited on interdigitated flat Au vs. DHBT Au substrate.

The Bode plot was then used to determine the relaxation time constant (τ_0) that gives an idea about the minimum time required to reach 50 % of the capacitive energy storage, which was calculated from the characteristic frequency corresponding to a phase angle of 45°. The low τ_0 values of 2.6 and 3.9 s. for the neat and SiWa doped TEAH/TFSI, respectively, further corroborated the facilitated ion transport and a higher power delivery performance **(Figure 2.18)**.

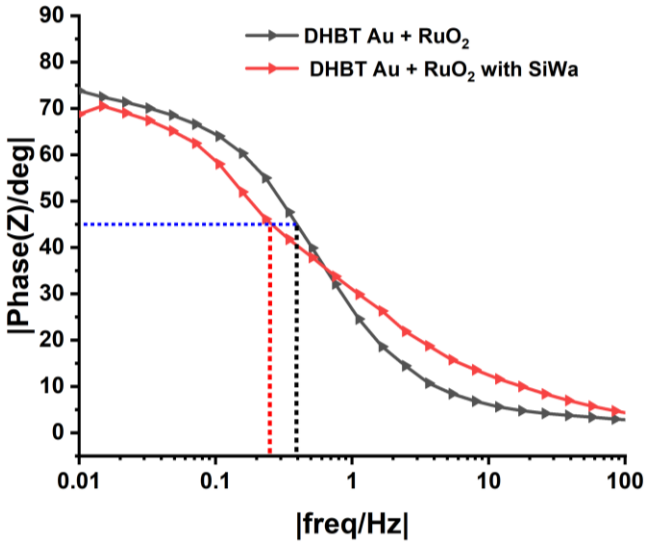

Figure 2.18: Bode plot of porous RuO_2 MSCs tested in TEAH/TFSI.

2.5.3 Ionogel-based 3D micro-supercapacitor and comparison with state-of-the-art

To envision the practical application of MSCs, it is imperative to develop solid-state-electrolyte which are leakage-free and able to perform well under real operational conditions. Liquid electrolytes are not compatible with microfabrication process due to evaporation and safety issues. Since SiWa doped TEAH/TFSI showed the best performance as the electrolyte for porous RuO_2 MSCs, we developed an ionogel using TEAH/TFSI + SiWa in combination with poly(vinylidene fluoride)-based host polymer. The choice of PVDF is obvious as it is a commonly used host matrix for the preparation of the ionogels in flexible energy storage devices as it offers high mechanical and thermal stability along with a high dielectric constant [33]. Ionogel was produced by mixing a poly(vinylidene fluoride) (Mw ≈ 534,000, Sigma Aldrich) in acetone and stirred until a uniform viscous solution is formed. After, SiWa ($H_4SiW_{12}O_{40}$) doped TEAH-TFSI electrolyte (90 wt%) was added to this solution and stirred for 2 h. The all solid-state micro-supercapacitor was realized by carefully drop-casting the ionogel electrolyte onto the interdigitated RuO_2 electrode and letting it dry at room temperature. To better understand the change in the ESR while transitioning from the liquid to gel-state of the electrolyte, we rely on the impedance spectroscopy measurement **(Figure 2.19)**. A higher ESR value of 52.5 Ω cm^2 for the solid-state device (more than double as compared to the liquid-state) can be attributed to the restricted ionic movement and the device being all-solid-state. The low frequency region in the EIS spectra is related to Warburg resistance with similar ion diffusion process in MSCs based on liquid-state and solid-state electrolytes.

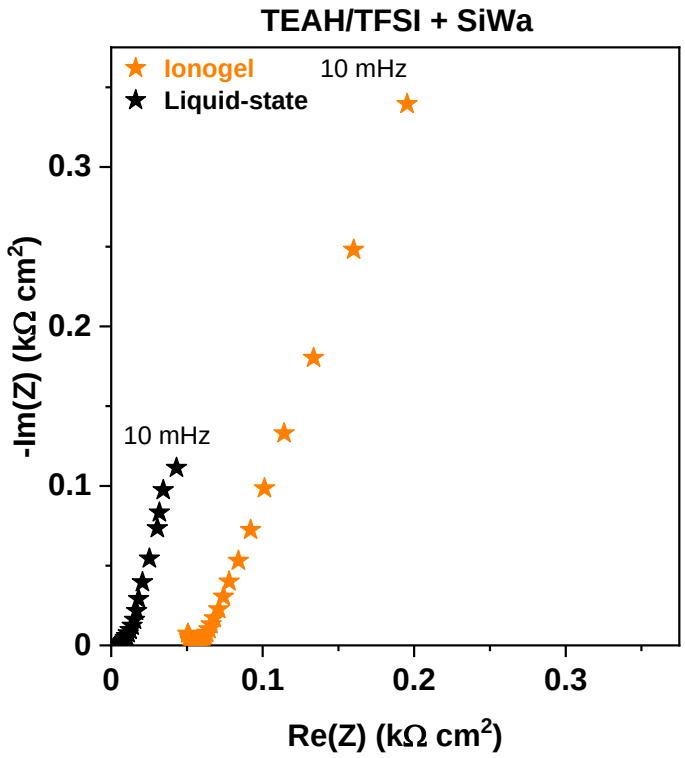

Figure 2.19: a. Electrochemical impedance spectroscopy (EIS) of porous RuO_2-based MSCs using liquid-state (black) and ionogel (orange) TEAH/TFSI electrolyte.

The pseudo-rectangular-shaped CV curves at different scan rates **(Figure 2.20)** showed the reversibility of the redox reactions. The solid-state MSC device showed the highest capacitance value of 79 mF cm^{-2} at 2 mV s^{-1}, which is closer to the performance reported using a liquid-state electrolyte (86 mF cm^{-2} at 5 mV s^{-1}).

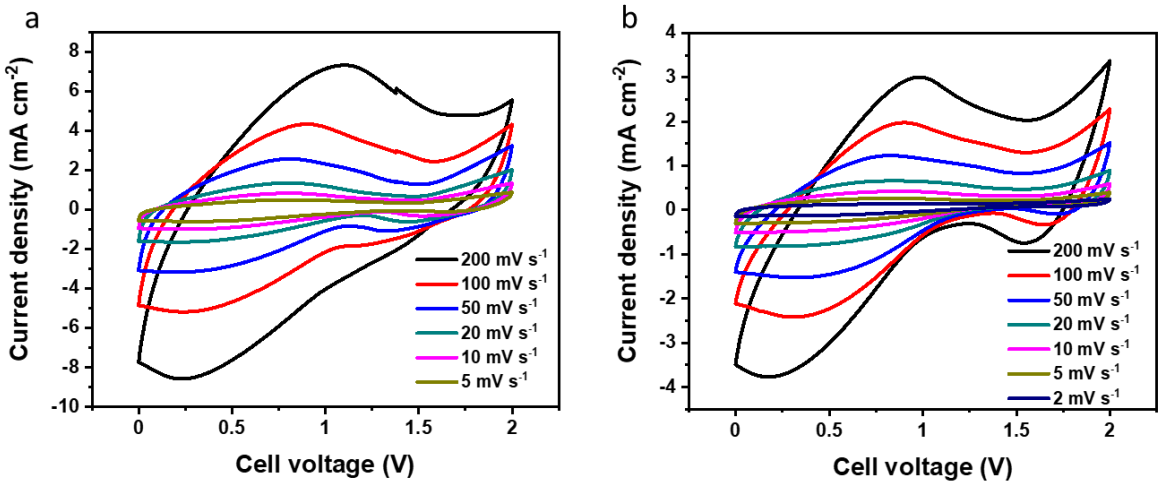

Figure 2.20: a. CV curves at different scan rates of 3D RuO_2 MSC tested in TEAH/TFSI + SiWa; b. CV curves of the all-solid-state MSC device using corresponding ionogel electrolyte.

The non-linear-looking GCD curves at various current densities indicate pseudocapacitive-based charge storage **(Figure 2.21)**. Compared to the CV and GCD curves of the MSCs using a liquid-state electrolyte, the all-solid-state MSC showed a characteristic resistive signature attributed to their higher ESR value.

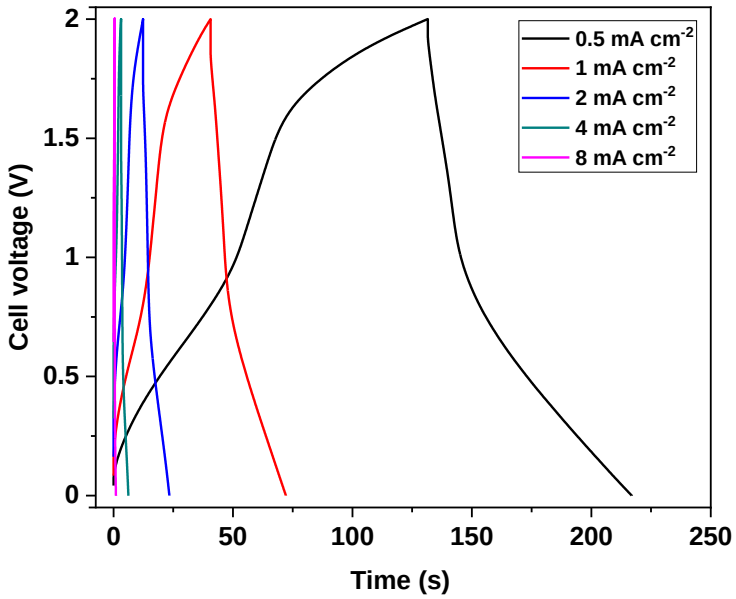

Figure 2.21: GCD curves of the all-solid-state MSC at different current densities.

We did try the electrochemical measurements of the ionogel-based all-solid-state MSC device in the 1.5 V window to understand whether it would lead to an improved electrochemical or cycling performance **(Figure 2.22)**. However, lowering the stability window did not lead to an improvement in long term cycling stability performance of the solid-state MSC.

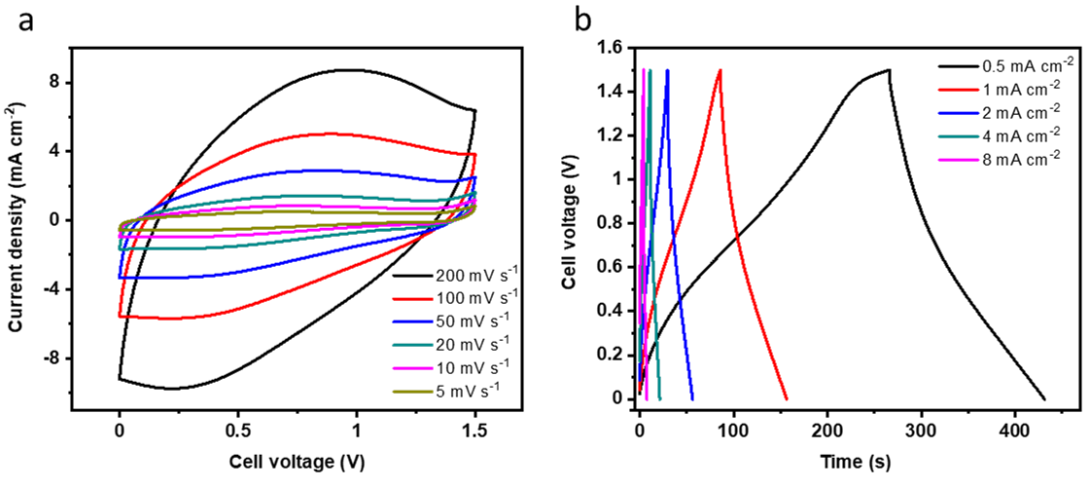

Figure 2.22: a. CV curves at different scan rates and b. GCD curves at different current densities of all-solid-state MSC device tested using SiWa-doped TEAH/TFSI electrolyte at 1.5 V.

The energy *vs.* power density comparison of porous RuO_2 MSCs tested in different electrolytes is represented in a Ragone plot to draw a broader perspective about their key difference in the areal performance matrix which is vital for the practical application of MSCs **(Figure 2.23)**. The higher cell voltage of PIL compared to the aqueous 0.5 M H_2SO_4 electrolyte led to an enhanced energy density performance of 31.8 µWh cm^{-2} at 0.5 mW cm^{-2} as compared to the MSC tested using 0.5 M H_2SO_4 (7.6 µWh cm^{-2} at 0.23 mW cm^{-2}). The solid-state MSC exhibited an energy density value of 17.26 µWh cm^{-2} at 0.56 mW cm^{-2}, which was slightly lower as compared to the liquid electrolyte.

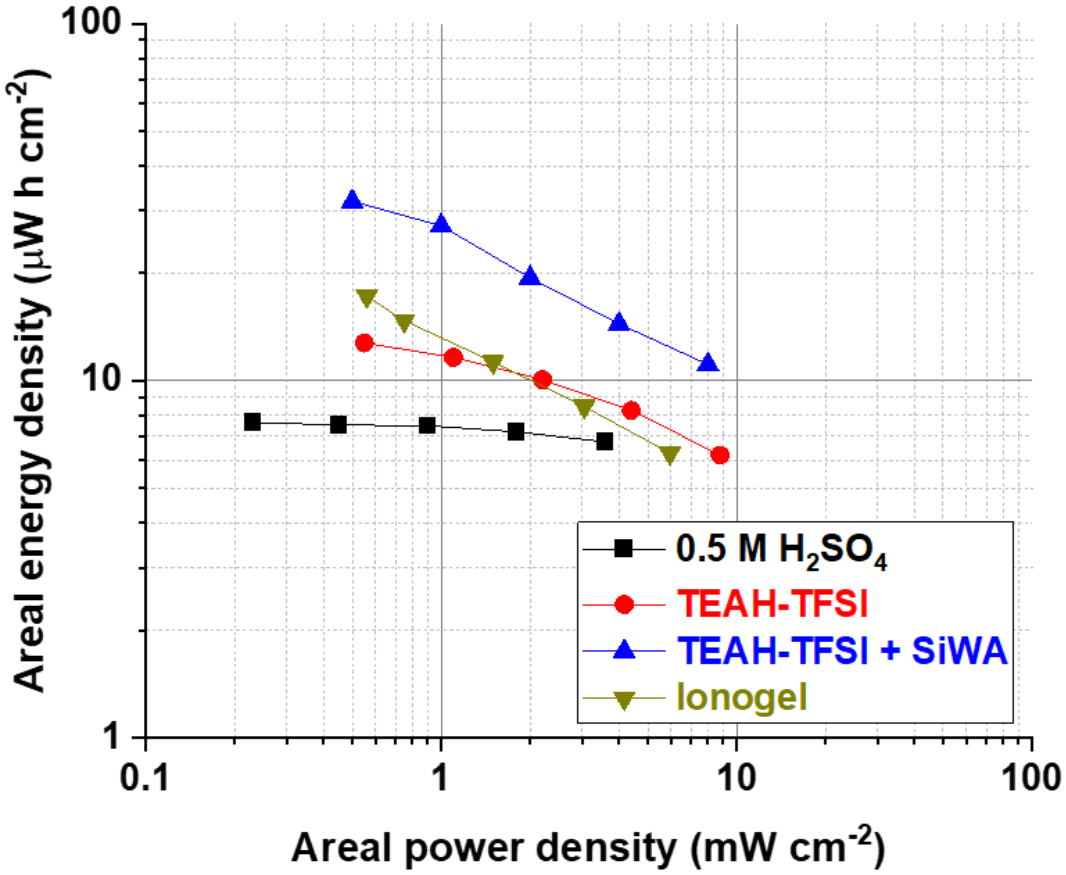

Figure 2.23: Ragone plot of porous RuO_2 MSCs tested in different electrolytes.

Table 2.3 shows a comparison of the electrochemical performance of porous RuO_2 MSCs with state-of-the-art in-plane MSCs consisting of carbon-based or pseudocapacitive materials. It's important to note that an explicit comparison with the performance reported in literature makes it difficult as there are big differences in the synthesis route, measurements followed, etc. and our goal here was to show an overview of the areal performance in different states of the electrolyte. Despite this difference, the performance of our RuO_2 MSC is comparable, if not superior, to the majority of reported MSCs based on double layer or pseudocapacitive-based materials.

Electrode Material	Electrolyte	Voltage (V)	Areal capacitance (mF cm^{-2})	Energy density (μW h cm^{-2})	Reference
PEDOT	1M H_2SO_4	0.8	9	-	[34]
MnO_2	1M Na_2SO_4	0.8	56	-	[35]
$Cu(OH)_2$@FeOOH	$EMIMBF_4/SiO_2$	1.5	58	18.07	[36]
LSG	1M H_2SO_4/PVA	1	25	2.6	[37]
EG	PVA/H_2SO_4	1	5.4	-	[38]
Onion-like carbon	1M Et_4NBF_4/APC	3	0.9	-	[39]
PPy/C	0.1M KCl	0.8	78.35	-	[40]
CNTs	PVA/H_3PO_4	1	2.44	-	[41]
EG/V_2O_5	PVA/LiCl	1	3.92	-	[42]
$Ti_3C_2T_x$//Ti_3CNT_x	PVA/H_2SO_4	0.6	61	0.63	[43]
F-graphene	$EMIMBF_4$	3.5	14.2	-	[44]
RuO_2	**0.5M H_2SO_4**	**0.9**	**85 @ 5 mV s^{-1}**	**9.5**	**This work**
	TEAH/TFSI	**2.2**	**34 @ 5 mV s^{-1}**	**22.8**	
	TEAH/TFSI + SiWa	**2**	**86@ 5 mV s^{-1}**	**47.7**	
	Ionogel	**1.5**	**79 @ 2 mV s^{-1}**	**24.6**	

Table 2.3. Performance comparison of porous RuO_2 MSCs with state-of-the-art in-plane MSCs.

In addition, even with pseudocapacitive electrode material and ionic-liquid electrolytes, the MSCs displayed a good long-term cycling performance of up to 5000 cycles **(Figure 2.24)**. It's

worth noting that the performance including areal capacitance, energy density, and cycle life can be greatly improved in the future with a rational choice of the PIL and a better understanding of the underlying charge storage mechanism. Although there's plenty of room open to address these important questions, the performance reported here clearly demonstrates the potential of RuO_2-based all-solid-state MSCs for future IoT-based applications.

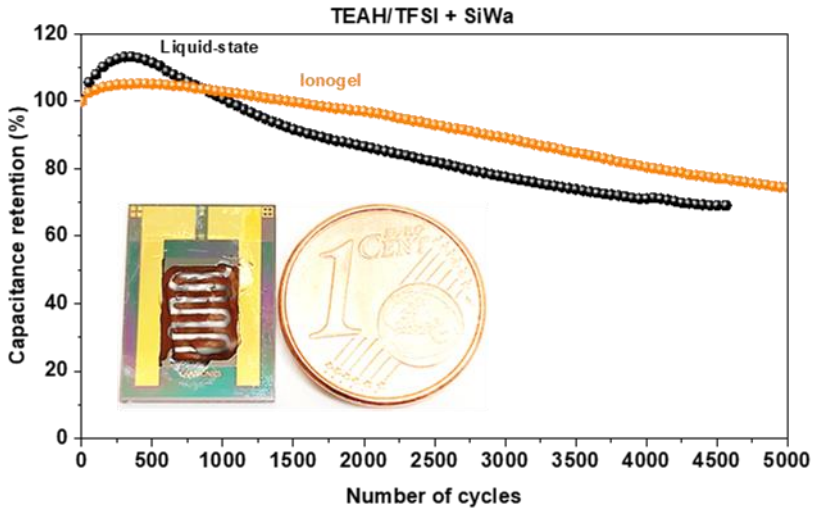

Figure 2.24: Long-term cycling stability study using liquid-state and ionogel electrolyte at 2 mA cm^{-2} (inset represents a typical porous RuO_2-MSC device with ionogel coating).

2.6 Conclusion

In summary, we have successfully demonstrated the use of protic ionic liquids as novel electrolytes for micro-supercapacitors employing electrodeposited RuO_2 electrodes. The surface-controlled proton-coupled electron transfer reaction is realized through the transfer of protons (H^+) from the base cation of PIL. The inclusion of SiWa granted the availability of free H^+ ions and enhanced pseudocapacitive current response with enlarged cell voltage. The use of PILs for real device application was further accomplished by the use of RuO_2 deposited on interdigitated porous

Au current collectors having a high area enlargement factor (AEF). The resultant porous MSC rendered a cell voltage exceeding 2 V with areal capacitance as high as 86 mF cm^{-2} at 5 mV s^{-1} and superior energy density performance of 31.8 µWh cm^{-2} at 0.5 mW cm^{-2}. The ionogel-based all-solid-state MSC showed the potential integration in real on-chip device applications rendering similar performance as liquid-state electrolyte with superior long-term cycling stability. We are convinced and important to emphasize that the performance can be greatly improved through rational architecting of porous MSC current collectors and conformal loading of the active material in combination with the ideal choice of the PIL. This work opens up new avenues for the development of high-performance MSC devices employing a combination of pseudocapacitive materials and ionic liquid-based safe electrolytes having better electrolyte ion confinement and higher energy storage performance.

2.7 References

[1] N. A. Kyeremateng, T. Brousse, D. Pech, Nat Nanotechnol 2017, 12, 7.

[2] J. H. Yu, C. Yu, W. Guo, Z. Wang, Y. W. Ding, Y. Y. Xie, K. L. Liu, H. Wang, X. Y. Tan, H. W. Huang, J. S. Qiu, Adv Funct Mater 2022, 32, 2204609.

[3] J. Zhang, G. Zhang, T. Zhou, S. Sun, Adv Funct Mater 2020, 30, 1910000.

[4] X. C. Tian, B. Xiao, X. Xu, L. Xu, Z. H. Liu, Z. Y. Wang, M. Y. Yan, Q. L. Wei, L. Q. Mai, Nano Research 2016, 9, 1012.

[5] T. Stettner, A. Balducci, Energy Storage Mater 2021, 40, 402.

[6] D. Rochefort, A. L. Pont, Electrochem. Commun. 2006, 8, 1539.

[7] S. Lindberg, S. Jeschke, P. Jankowski, M. Abdelhamid, T. Brousse, J. Le Bideau, P. Johansson, A. Matic, J Power Sources 2020, 460, 228111.

[8] A. Djire, J. Y. Ishimwe, S. Choi, L. T. Thompson, Electrochem Commun 2017, 77, 19; F. Al-Zohbi, J. Jacquemin, F. Ghamouss, B. Schmaltz, M. Abarbri, K. Cherry, M. F. Tabcheh, F. Tran-Van, J Power Sources 2019, 431, 162.

[9] M. Armand, F. Endres, D. R. MacFarlane, H. Ohno, B. Scrosati, Nat Mater 2009, 8, 621; J. Le Bideau, L. Viau, A. Vioux, Chem Soc Rev 2011, 40, 907.

[10] C. A. Angell, N. Byrne, J. P. Belieres, Acc Chem Res 2007, 40, 1228; L. Mayrand-Provencher, D. Rochefort, J Phys Chem C 2009, 113, 1632; T. Vogl, P. Goodrich, J. Jacquemin, S. Passerini, A. Balducci, J Phys Chem C 2016, 120, 8525.

[11] M. Anouti, M. Caillon-Caravanier, Y. Dridi, H. Galiano, D. Lemordant, J Phys Chem B 2008, 112, 13335.

[12] L. Mayrand-Provencher, S. X. Lin, D. Lazzerini, D. Rochefort, J Power Sources 2010, 195, 5114.

[13] L. Timperman, P. Skowron, A. Boisset, H. Galiano, D. Lemordant, E. Frackowiak, F. Beguin, M. Anouti, Phys Chem Chem Phys 2012, 14, 8199; A. Brandt, J. Pires, M. Anouti, A. Balducci, Electrochim Acta 2013, 108, 226; X. H. Wang, M. Salari, D. E. Jiang, J. C. Varela, B. Anasori, D. J. Wesolowski, S. Dai, M. W. Grinstaff, Y. Gogotsi, Nat Rev Mater 2020, 5, 787.

[14] S. Menne, T. Vogl, A. Balducci, Chem Commun (Camb) 2015, 51, 3656.

[15] L. Köps, F. A. Kreth, A. Bothe, A. Balducci, Energy Storage Mater 2022, 44, 66.

[16] J. P. Belieres, C. A. Angell, J Phys Chem B 2007, 111, 4926.

[17] W. Xu, E. I. Cooper, C. A. Angell, The J. Phys. Chem. B. 2003, 107, 6170.

[18] H. A. Elwan, M. Mamlouk, K. Scott, J Power Sources 2021, 484, 229197.

[19] M. Yoshizawa, W. Xu, C. A. Angell, J Am Chem Soc 2003, 125, 15411.

[20] K. D. Kreuer, M. Hampele, K. Dolde, A. Rabenau, Solid State Ionics 1988, 28, 589; R. C. T. Slade, H. A. Pressman, E. Skou, Solid State Ionics 1990, 38, 207.

[21] S. Herrmann, C. Ritchie, C. Streb, Dalton Trans 2015, 44, 7092.

[22] S. G. Patnaik, J. Shamsudeen Seenath, D. Bourrier, S. Prabhudev, D. Guay, D. Pech, ACS Energy Lett. 2020, 6, 131.

[23] J. W. Long, B. Dunn, D. R. Rolison, H. S. White, Adv. Energy Mater. 2020, 10, 2002457.

[24] W. L. Tsai, P. C. Hsu, Y. Hwu, C. H. Chen, L. W. Chang, J. H. Je, H. M. Lin, A. Groso, G. Margaritondo, Nature 2002, 417, 139.

[25] J. Zhang, M. D. Baro, E. Pellicer, J. Sort, Nanoscale 2014, 6, 12490.

[26] H. C. Shin, J. Dong, M. L. Liu, Adv Mater 2003, 15, 1610.

[27] N. Swain, B. Saravanakumar, M. Kundu, L. Schmidt-Mende, A. Ramadoss, J. Mater. Chem. A 2021, 9, 25286.

[28] Y. Li, W. Z. Jia, Y. Y. Song, X. H. Xia, Chem. Mater. 2007, 19, 5758.

[29] H. Jiang, Y. Guo, T. Wang, P. L. Zhu, S. H. Yu, Y. Yu, X. Z. Fu, R. Sun, C. P. Wong, Rsc Adv 2015, 5, 12931.

[30] A. Ferris, S. Garbarino, D. Guay, D. Pech, Adv Mater 2015, 27, 6625.

[31] A. Ferris, D. Bourrier, S. Garbarino, D. Guay, D. Pech, Small 2019, 15, e1901224.

[32] S. Ardizzone, G. Fregonara, S. Trasatti, Electrochim Acta 1990, 35, 263.

[33] P. F. R. Ortega, J. P. C. Trigueiro, G. G. Silva, R. L. Lavall, Electrochim Acta 2016, 188, 809; B. Asbani, B. Bounor, K. Robert, C. Douard, L. Athouel, C. Lethien, J. Le Bideau, T. Brousse, J. Electrochem. Soc. 2020, 167, 100551; S. Rajeevan, S. John, S. C. George, J Power Sources 2021, 504, 230037.

[34] N. Kurra, M. K. Hota, H. N. Alshareef, Nano Energy 2015, 13, 500.

[35] X. Wang, B. D. Myers, J. Yan, G. Shekhawat, V. Dravid, P. S. Lee, Nanoscale 2013, 5, 4119.

[36] J. Q. Xie, Y. Q. Ji, J. H. Kang, J. L. Sheng, D. S. Mao, X. Z. Fu, R. Sun, C. P. Wong, Energ Environ Sci 2019, 12, 194.

[37] W. L. Zhang, Y. J. Lei, F. W. Ming, Q. Jiang, P. M. F. J. Costa, H. N. Alshareef, Adv. Energy Mater. 2018, 8, 1801840.

[38] Z. Liu, Z. S. Wu, S. Yang, R. Dong, X. Feng, K. Mullen, Adv Mater 2016, 28, 2217.

[39] D. Pech, M. Brunet, H. Durou, P. Huang, V. Mochalin, Y. Gogotsi, P. L. Taberna, P. Simon, Nat Nanotechnol 2010, 5, 651.

[40] M. Beidaghi, C. Wang, Electrochim Acta 2011, 56, 9508.

[41] W. Yu, H. Zhou, B. Q. Li, S. Ding, ACS Appl. Mater. & Interfaces 2017, 9, 4597.

[42] P. Zhang, F. Zhu, F. Wang, J. Wang, R. Dong, X. Zhuang, O. G. Schmidt, X. Feng, Adv Mater 2017, 29, 1604491.

[43] C. F. Zhang, M. P. Kremer, A. Seral-Ascaso, S. H. Park, N. McEvoy, B. Anasori, Y. Gogotsi, V. Nicolosi, Adv Funct Mater 2018, 28, 1705506.

[44] F. Zhou, H. Huang, C. Xiao, S. Zheng, X. Shi, J. Qin, Q. Fu, X. Bao, X. Feng, K. Mullen, Z. S. Wu, J Am Chem Soc 2018, 140, 8198.

Chapter 3 RuO_2 MSCs using Pyrrolidinium-based PILs containing varying alkyl substitution and anion groups

3.1 Pyrrolidinium-based PILs

In this chapter, we investigate the use of pyrrolidinium-based protic ionic liquids (PILs) containing varying alkyl substitution and anion groups as electrolytes for RuO_2 micro-supercapacitors. The molten conducting salt using pyrrolidinium-based cation appears to be most promising owing to its relatively low cost, and low toxicity and helps to increase the operating voltage of supercapacitors and batteries without reducing the power and cycle life [1], [2], [3], [4], [5]. To gain more insight into how the pyrrolidinium-based PIL affects micro-supercapacitor charge storage using RuO_2 electrodes, we carefully designed the PIL cations with varying alkyl substitutions and anion groups **(Figure 3.1)**. It should be noted that when the number of carbon atoms in the alkyl chain length reduces below C_3 (which is the case for Pyr_{1H}-TFA), the resulting PIL tends to solidify. This makes it difficult to use such PIL as an electrolyte for our MSCs. Whereas in the case of Pyr_{1H}-BF_4 with a different anionic group, the PIL becomes extremely hydrophilic with a water content of ca. 8000 ppm even after drying. It should be noted that when the water content drops below a certain limit while undergoing ultra-high vacuum treatment, Pyr_{1H}-BF_4 will no longer remain in the liquid state. Hence the right balance between water and the PIL ratio is important to avail their function as electrolytes for supercapacitors.

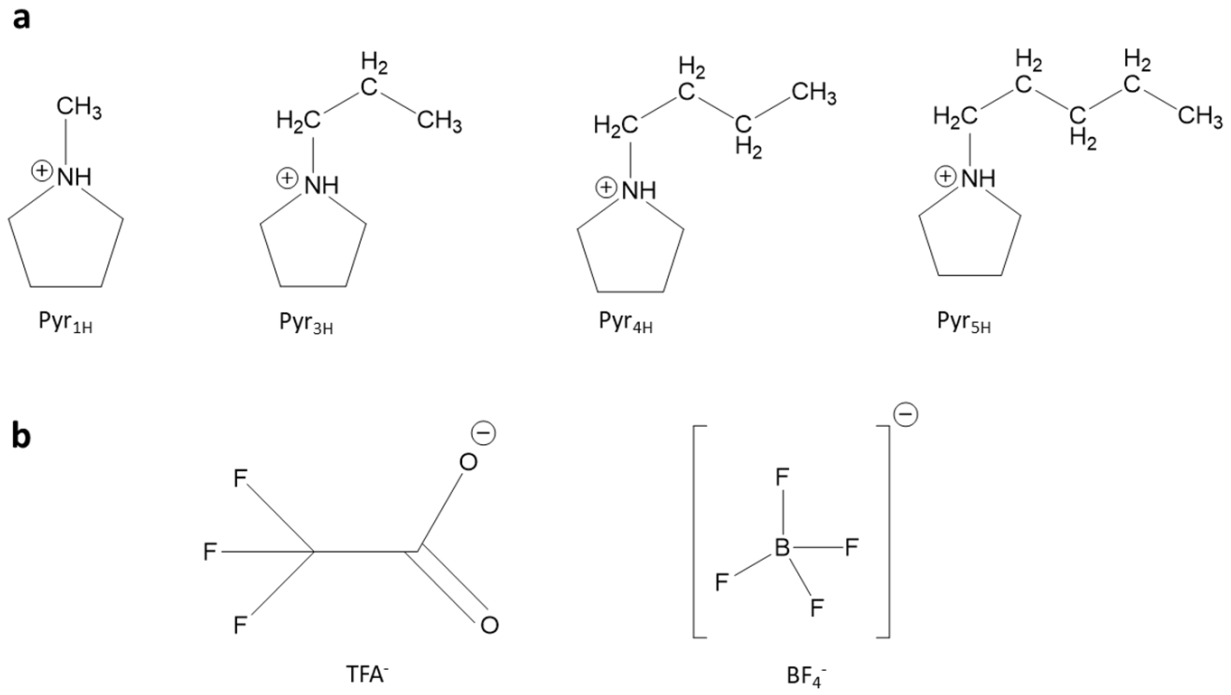

Figure 3.1: Structure of the pyrrolidinium-based cations (a) and corresponding anion groups (b) investigated for the RuO_2 MSCs (Pyr_{1H} = 1-methyl pyrrolidinium, Pyr_{3H} = 1-propyl pyrrolidinium, Pyr_{4H} = 1-butyl pyrrolidinium, Pyr_{5H} = 1-pentyl pyrrolidinium, TFA = trifluoroacetate, BF_4 = tetrafluoroborate).

Unlike aprotic ionic liquids (AILs), the presence of a proton at the base cation in PILs can give rise to a hydrogen bond network [6], [7]. This unique feature in a PIL can be potentially utilized to design hydrophilic PILs where water molecules can interact with PIL via hydrogen bonding interaction. This reciprocity between water and PIL can boost the electrolyte conductivity by combining a Grotthuss-like proton migration with vehicular transport [1], [8], [9], [10]. The prospect of understanding the interplay between PIL and water is therefore appearing to be of significant interest for rationally developing electrolytes for energy storage devices [11], [12]. In the context of RuO_2 MSCs, designing hydrophilic PILs holds promise as it can accelerate the charge transfer and pseudocapacitive charge storage without compromising the power density performance.

3.1.1 Synthesis of Pyrrolidinium-based PILs

All the PILs were prepared by the neutralization reaction by slowly adding the acid precursor into the alkyl pyrrolidine base in an equimolar ratio. Due to the exothermic nature, the reaction was conducted in an ice bath while stirring. When the reaction was over, PIL samples were dried under a vacuum and kept in the glove box under an argon atmosphere. The Pyr_{1H}-BF_4 used for this study is provided to us by Prof. Andrea Balducci, (Friedrich Schiller University Jena, Germany). The water content in PILs was measured by the Karl Fisher titration method.

3.1.2 Characterization of Pyrrolidinium-based PILs

To understand the transport properties of pyrrolidinium-based PILs, conductivity, density, and viscosity measurements were carried out. The measured values are given in **Table 3.1**.

Electrolyte	η (RT) (cP)	ρ (RT) (g cm^{-3})	σ (RT) (mS cm^{-1})
Pyr_{1H}-BF_4	37.03	1.27	21
Pyr_{3H}-TFA	23.08	1.2	3.8
Pyr_{4H}-TFA	32.9	1.14	1.63
Pyr_{5H}-TFA	23.17	1.09	1.05

Table 3.1. Physicochemical properties of the pyrrolidinium-based protic ionic liquids.

The temperature-dependent ionic conductivity values of the PILs were represented on a common Arrhenius plot **(Figure 3.2 a)**, and the values understandably reflect the ion-ion interaction, strength of hydrogen bonding, and water content in the PIL. Apparently, the hygroscopic nature of Pyr_{1H}-BF_4 showed the highest molar ionic conductivity (ca. 20 mS cm^{-1} at 20 °C) with a water content of ca. 8000 ppm. This value is significantly higher than that observed in other PILs, which indicate a significant contribution coming from Grotthuss type charge transport observed in aqueous electrolytes. For pyrrolidinium-based PILs with TFA^- anions, the PIL with lower alkyl chain length (Pyr_{3H}-TFA) showed higher conductivity values as smaller alkyl chain group can enable faster ion migration, similar to what's observed with some of the reported

ionic liquid-based supercapacitors [13], [14]. The high ionicity of $Pyr_{1H}BF_4$ is also reflected in the Walden plot (a plot compares the relationship between conductivity and viscosity values), where it occupied a region above the ideal line (as described by Angell and co-workers [15]) similar to aqueous protic electrolytes **(Figure 3.2 b)**. This is very unusual with respect to PILs, where a non-vehicular charge transport contribution is prevalent and one must be very careful while representing such PILs on a Walden plot as the normal assumptions on ionic liquid characteristics are no longer met [16]. The origin of $Pyr_{1H}BF_4$'s unique property could also be attributed to its water in salt structure [17]. A recent report from Mariani *et al.* states that the ionicity of ILs is often overestimated, due to an incomplete acid-base reaction [18]. This peculiar behaviour in Pyr_{1H}-BF_4 despite its viscous nature could originate from a higher water content leading to disruption of ion-ion interaction resulting in PIL to remain in a completely dissociated state. Whereas the conductivity values investigated for the remaining PILs (Pyr_{3H}-TFA, Pyr_{4H}-TFA, and Pyr_{5H}-TFA), they occupy the region of good ionic liquids in the Walden plot with slight ion pairing as most of the reported PILs in the literature [7].

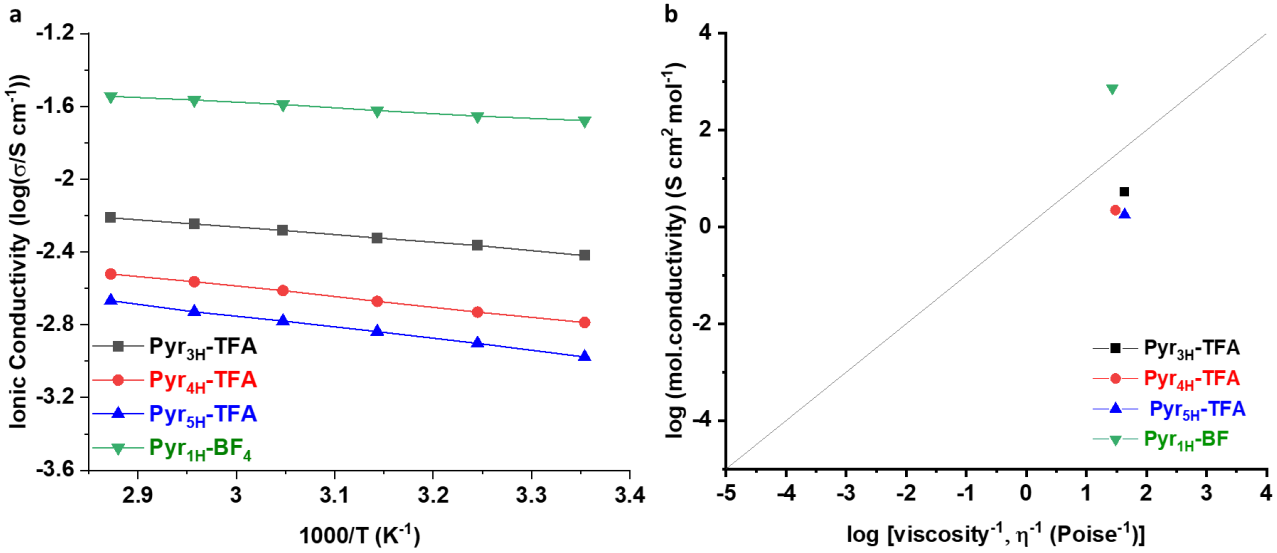

Figure 3.2: Characterisation of electrolytes. a. Arrhenius plots for the pyrrolidinium-based PILs with measurements done at an interval of 10°C from 25 to 75°C; b. The walden plot compares the ionicity and equivalent conductivity values of pyrrolidinium-based PILs.

Overall, the conductivity values exhibited by these chosen PIL candidates show promising to be used as electrolytes for RuO_2 MSCs.

3.2 Electrochemical study of RuO_2 MSC using Pyrrolidinium-based PILs

In this section, the electrochemical characterization results of RuO_2 MSCs using pyrrolidinium-based PILs are provided in greater detail. At first, the study is done with flat interdigitated Au substrates and later using interdigitated DHBT substrates with higher RuO_2 loading. In the end, results obtained for all-solid-state porous RuO_2 MSC employing ionogel electrolytes are provided.

3.2.1 Electrochemical study on flat substrates

Figure 3.3 a show a comparison of the CVs of RuO_2 MSCs tested in pyrrolidinium-based PILs with a similar number of RuO_2 deposition cycles at a cell voltage of 1.5 V. The CVs showed a pseudocapacitive shape with a typical redox signature of the RuO_2 electrode. The MSC cell voltage using PILs is superior to RuO_2 MSCs tested using aqueous electrolytes where the ESW is limited to *ca.* 1 V owing to the low redox potential of electrochemical H_2O splitting (1.23 V) restricting the ESW, resulting in low cell voltage and energy density [19]. Among all the PILs studied, Pyr_{3H}-TFA showed a higher CV current density attributed to its lower alkyl chain length and better ionic mobility enabling swift charge transfer to promote surface redox reactions. Despite the high molar conductivity of Pyr_{1H}-BF_4, the current density of RuO_2 MSC exhibited by this PIL appears to be in the range of Pyr_{4H}-TFA. This could imply that redox active sites are not easily accessible with Pyr_{1H}-BF_4, and that its higher viscosity, despite its higher conductivity (σ) value, influences charge storage behavior. A comparison of EIS plots of RuO_2 MSCs tested in pyrrolidinium-based PILs is shown in **Figure 3.3 b.** The EIS showed an ideal capacitive behavior

in all the electrolytes with lower ESR values for Pyr_{3H}-TFA and Pyr_{1H}-BF_4. The ESR values increase as the alkyl chain length of the base cation increases, which was evident from the resistive CV of RuO_2 MSC tested using Pyr_{5H}-TFA.

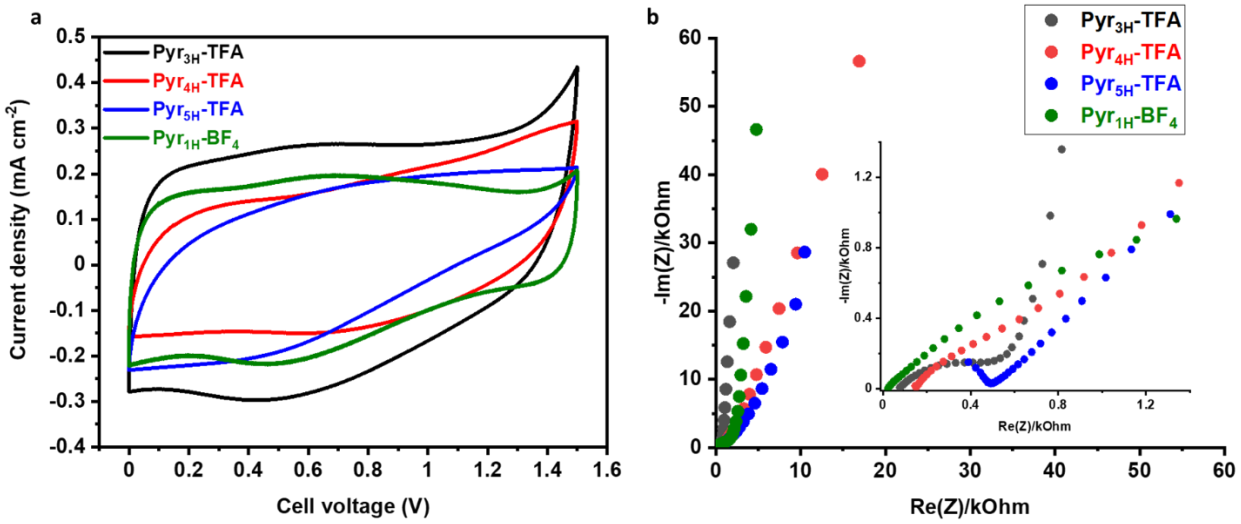

Figure 3.3: Electrochemical characterization of RuO_2 on interdigitated flat Au substrates tested in different pyrrolidinium-based PILs. a. Comparison of CV curves at 100 mV s^{-1}; b. Comparison of EIS from 100 kHz to 10 mHz.

3.2.2 Electrochemical study on 3D Porous substrates

Following the initial investigation of PILs using RuO_2 deposited on flat MSC substrates, we performed electrochemical characterization on DHBT MSC substrates with higher RuO_2 loading (for a DHBT deposition time of 10 min and 300 RuO_2 deposition cycles). The metallic current collector's thickness and aspect ratio AR (defined as the ratio of the electrochemically active surface area to the geometrical surface area) were approximately 30 μm and 374 cm^2 cm^{-2}, respectively. Compared to flat substrates, a porous DHBT current collector offers a higher surface area to load more active materials and can help achieve practical level charge storage performance. Interestingly, CV current density showed a similar behavior as that of RuO_2 deposited on a flat interdigitated substrate with Pyr_{3H}-TFA showing a higher current response along with a

comparable current density for Pyr_{1H}-BF_4 and Pyr_{4H}-TFA **(Figure 3.4 a)**. It can be noticed that a slight distortion and change in the shape of CV curves moving from flat to porous substrates as the ion dynamics and charge transfer behavior gets complex with more active materials present in these high roughness substrates. The same trend is reflected in the EIS results of DHBT MSC as represented in **Figure 3.4 b**, where Pyr_{1H}-BF_4 showed the lowest ESR value followed by Pyr_{3H}-TFA. This further indicates a small internal electrical resistance (or energy loss) for these electrolyte systems. A comparison of the ESR values of RuO_2 MSCs tested with pyrrolidinium-based PILs are shown in **Table 3.2**. Certainly, a difference in the length of the alkyl chain on the pyrrolidinium cation can results in the structural change of the electrode/ionic liquid interface and thus affects the electrochemical performance. The lower ionic conductivity of Pyr_{5H}-TFA prevents these ions to access the deeper active sites on the densely connected pores leading to a higher device resistance.

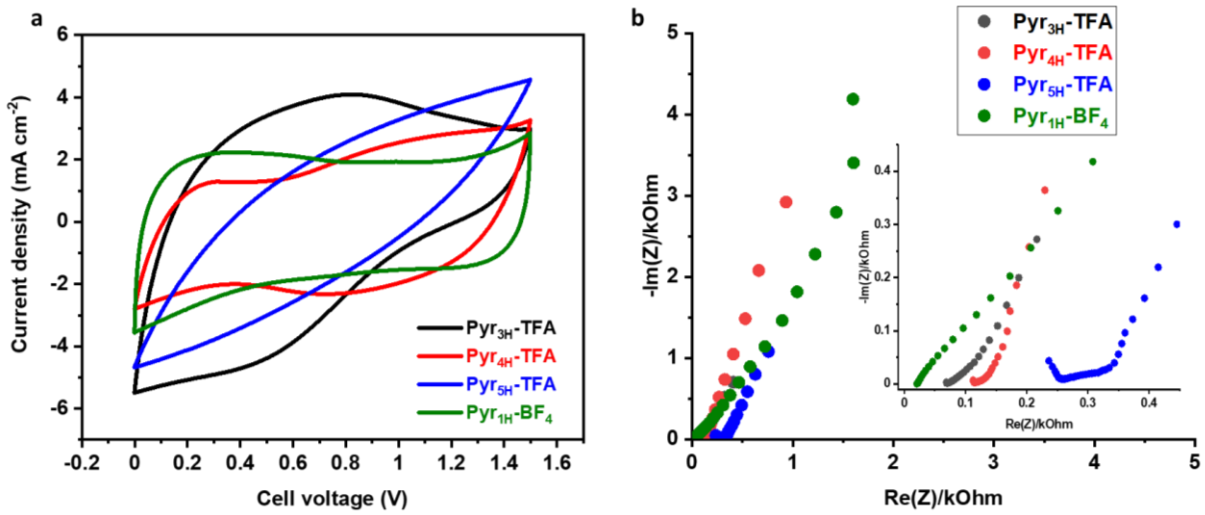

Figure 3.4: Electrochemical characterization of RuO_2 on interdigitated DHBT Au substrates tested in different pyrrolidinium-based PILs. a. Comparison of CV curves at 100 mV s^{-1}; b. Comparison of EIS from 100 kHz to 10 mHz.

PIL	ESR (Ω cm^2)
Pyr_{1H}-BF_4	5
Pyr_{3H}-TFA	17
Pyr_{4H}-TFA	28
Pyr_{5H}-TFA	60

Table 3.2: Comparison of the equivalent series resistance (ESR) values of RuO_2 MSCs tested in pyrrolidinium-based PILs.

Among all the pyrrolidinium-based PILs explored for RuO_2 MSCs, Pyr_{3H}-TFA and Pyr_{1H}-BF_4 showed promising results. Hence, these PILs are chosen to make detailed electrochemical characterization with porous RuO_2 MSCs. These PIL candidates are also exclusively selected for developing ionogel electrolytes to construct all-solid-state porous RuO_2 MSCs.

The CV curves of porous RuO_2 MSCs tested using Pyr_{3H}-TFA at different scan rates are shown in **Figure 3.5 a.** The CVs exhibit pseudocapacitive signatures with reversibility of the redox process. Faradaic charge storage is also well represented in the galvanostatic charge-discharge (GCD) plots with non-linear curves at varying current densities **(Figure 3.5 b)**. The porous RuO_2 MSC using Pyr_{3H}-TFA rendered an areal capacitance value as high as 106 mF cm^{-2} at 5 mV s^{-1}. This further demonstrates that the charge storage performance can be further enhanced by using DHBT substrate with higher surface area and more loading of the active material.

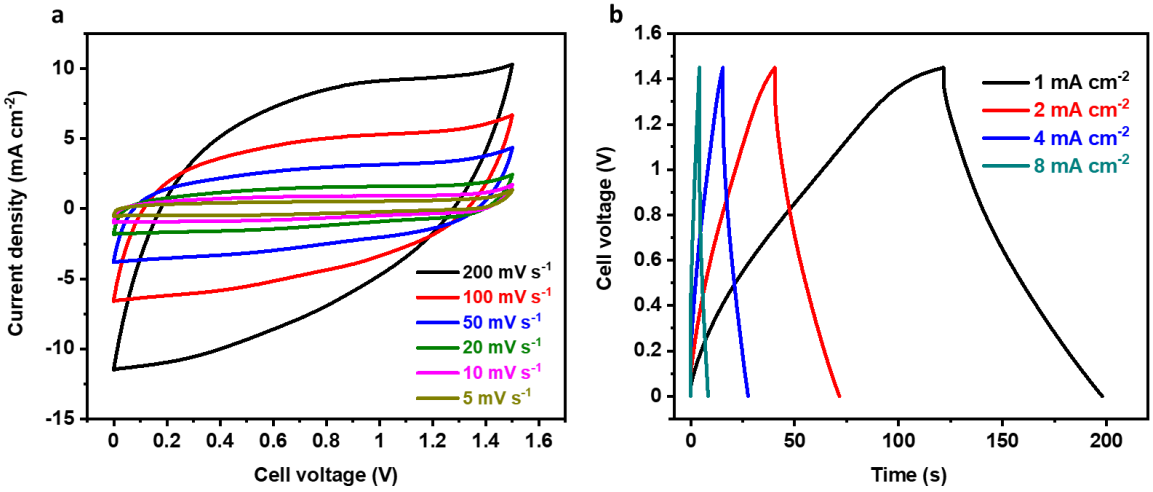

Figure 3.5: Porous RuO_2 MSCs tested in Pyr_{3H}-TFA. a. CV curves at different scan rates; b. GCD curves at different current densities.

3.2.3 All-Solid-State 3D RuO_2 MSC

To facilitate the integration of MSCs for on-chip device applications, developing safer and solid-state electrolytes is inevitably important. We, therefore, developed an all-solid-state MSC using interdigitated porous RuO_2 electrodes and Pyr_{3H}-TFA-derived ionogel electrolyte. A comparison of the CVs of porous RuO_2 MSC using neat Pyr_{3H}-TFA and corresponding ionogel electrolyte showed that the solid-state MSC can still retain pseudocapacitive features with a slightly reduced current density **(Figure 3.6 a)**. For a similar number of RuO_2 deposition cycles as explored for the neat Pyr_{3H}-TFA, the corresponding all-solid-state porous RuO_2 MSC using Pyr_{3H}-TFA-derived ionogel showed an areal capacitance performance of 48 mF cm^{-2} at 5 mV s^{-1}. It's very evident from the EIS results that the ionogel electrolyte slightly restricts the ionic conductivity with an increase in the value of ESR **(Figure 3.6 b)**. The solid-state MSC exhibited an ESR value of 22 Ω cm^2, which is 27% higher as compared to when the liquid form of Pyr_{3H}-TFA is employed. Despite this difference, the Pyr_{3H}-TFA-based porous RuO_2 MSC could exhibit a high specific power of 25.6 mW cm^2.

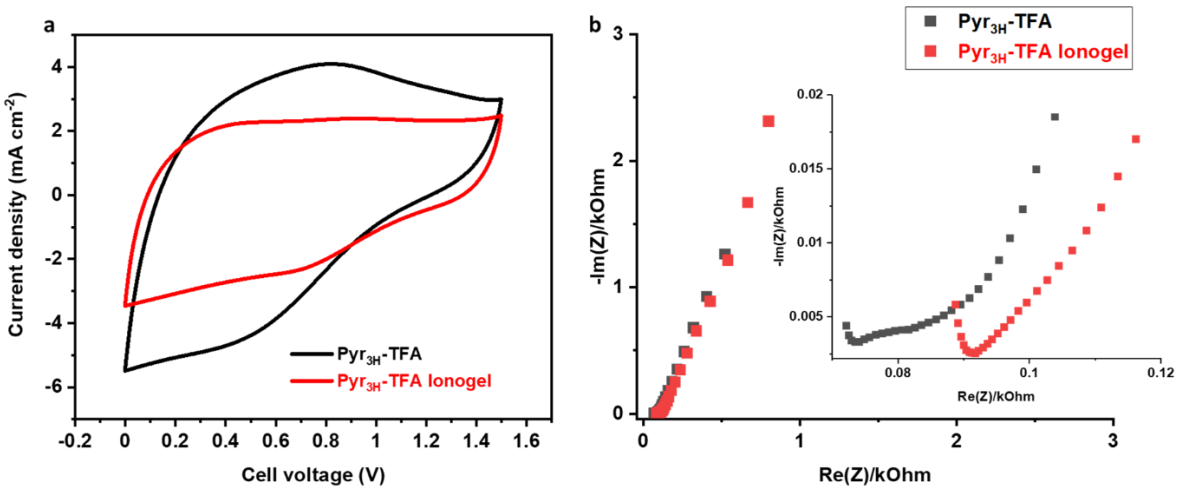

Figure 3.6: a. CV curves of liquid state and all-solid-state porous RuO_2 MSC using Pyr_{3H}-TFA and Pyr_{3H}-TFA derived ionogel electrolyte at 100 mV s^{-1} and b. corresponding EIS curves.

The CV curves of porous RuO_2 MSC using Pyr_{1H}-BF_4 also displayed a pseudocapacitive footprint with the reversibility of the redox reactions at different scan rates **(Figure 3.7 a)**. The ideal capacitive behavior is very well demonstrated by the EIS plot with a greatly reduced ESR (2 Ω cm^2) and a nearly vertical line at low frequencies parallel to the imaginary axis of the impedance spectrum **(Figure 3.7 b)**. This extremely low ESR while using Pyr_{1H}-BF_4 could be originating from the high-water content that's uniformly distributed in the PIL facilitating a Grotthuss-type proton transport.

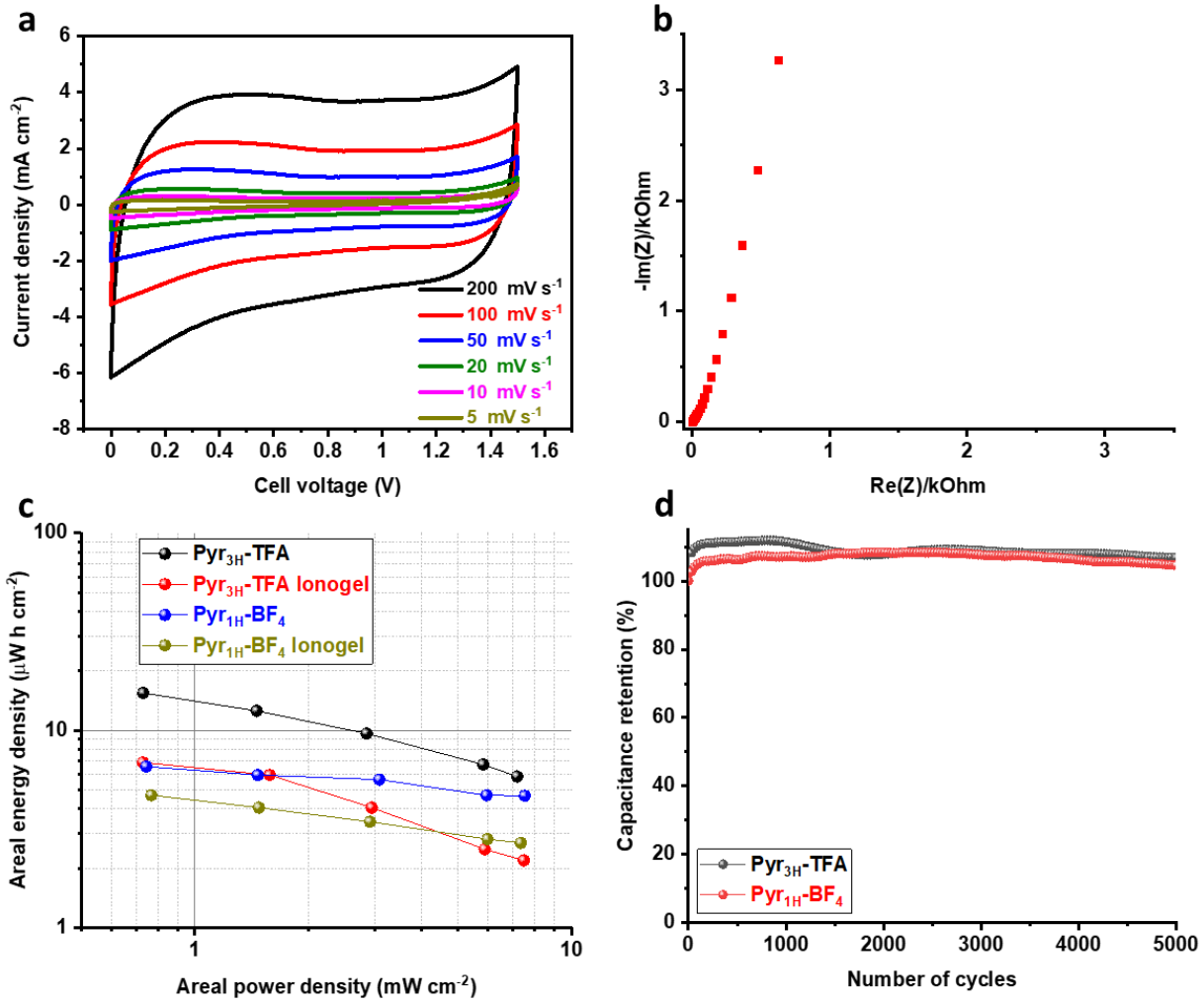

Figure 3.7: a. CV curves at different scan rates and b. EIS of porous RuO_2 MSC tested in Pyr_{1H}-BF_4; c. The ragone plot of porous RuO_2 MSCs tested in Pyr_{3H}-TFA and Pyr_{1H}-BF_4- based electrolytes and d. cycling stability performance.

The Ragone plot gives a very good perspective on the energy and power density performance of energy storage devices. A comparison of our porous RuO_2 MSCs tested in Pyr_{3H}-TFA and Pyr_{1H}-BF_4-based electrolytes is shown in **Figure 3.7 c**. The combined merits of a higher cell voltage and areal capacitance of porous RuO_2 MSC using Pyr_{3H}-TFA give rise to an enhanced energy density performance of 15.5 µWh cm^{-2} at 0.73 mW cm^{-2}. The energy density can still retain a value of 5.9 µWh cm^{-2} at a higher power density of 7.2 mW cm^{-2}. The corresponding solid-state

MSC using Pyr_{3H}-TFA-derived ionogel displayed a decent areal energy density performance of 8.4 μWh cm^{-2} at 0.19 mW cm^{-2}. Parallelly, the RuO_2 MSCs tested using Pyr_{1H}-BF_4 and Pyr_{1H}-BF_4-based ionogel electrolytes showed reasonable energy density performance of 6.5 μWh cm^{-2} and 4.7 μWh cm^{-2} respectively at corresponding power densities of 0.74 mW cm^{-2} and 0.76 mW cm^{-2}. The superior power densities obtained for porous RuO_2 MSCs with Pyr_{1H}-BF_4 can be ascribed to their lower ESR values resembling aqueous electrolytes. The cycling performance of energy storage devices is an important characteristic that will determine the practical application of micro-supercapacitors. The porous RuO_2 MSC using Pyr_{3H}-TFA and Pyr_{1H}-BF_4 demonstrated excellent long-term cycling stability **(Figure 3.7 d),** which unarguably suggests the practical employability of our MSCs. Although there are several avenues to further elevate the performance including a rational current collector design, and conformal loading of RuO_2 enabling better charge accessibility with the PILs, the excellent electrochemical characteristics using pyrrolidinium-based PILs hold promise to use RuO_2-based MSCs for future IoT-based technologies.

3.3 Conclusion

Herein, we have shown the application of pyrrolidinium-based protic ionic liquids with varying alkyl substitution and anion groups as potential electrolyte candidates for RuO_2 micro-supercapacitors. The pseudocapacitive charge storage is achieved using these PILs with a cell voltage of 1.5 V that's unachievable with conventional aqueous electrolytes. The porous RuO_2 MSC using 1-propyl pyrrolidinium trifluoroacetate (Pyr_{3H}-TFA) showed an areal capacitance value of 106 mF cm^{-2} at 5 mV s^{-1} which corresponds to an energy density of 33.1 μWh cm^{-2}. The all-solid-state MSCs developed using Pyr_{3H}-TFA and Pyr_{1H}-BF_4 electrolytes showed promising results with complimentary energy and power performances. In addition, these PILs showed a long-term cycling behavior for the devices, which further demonstrates the practical prospect of

RuO_2 MSCs. Despite the remarkable MSC charge storage performance using these novel electrolytes, there remain ample opportunities to further improve the charge storage performance through optimization strategies and unveiling the underlying charge storage mechanism. These approaches will not only provide newer insights on suitable power solutions but also will undoubtedly foster the advancement of IoT technology.

3.4 References

[1] M. Anouti, M. Caillon-Caravanier, Y. Dridi, H. Galiano, D. Lemordant, J Phys Chem B 2008, 112, 13335.

[2] S. Pohlmann, A. Balducci, Electrochim Acta 2013, 110, 221.

[3] S. Pohlmann, R. S. Kuhnel, T. A. Centeno, A. Balducci, Chemelectrochem 2014, 1, 1301.

[4] C. Wolff, S. Jeong, E. Paillard, A. Balducci, S. Passerini, J Power Sources 2015, 293, 65.

[5] L. Köps, F. A. Kreth, A. Bothe, A. Balducci, Energy Storage Mater 2022, 44, 66.

[6] M. Yoshizawa, W. Xu, C. A. Angell, J Am Chem Soc 2003, 125, 15411.

[7] T. Stettner, A. Balducci, Energy Storage Mater 2021, 40, 402.

[8] R. Hayes, S. Imberti, G. G. Warr, R. Atkin, Angew Chem Int Ed Engl 2012, 51, 7468.

[9] F. Al-Zohbi, J. Jacquemin, F. Ghamouss, B. Schmaltz, M. Abarbri, K. Cherry, M. F. Tabcheh, F. Tran-Van, J Power Sources 2019, 431, 162.

[10] J. Ingenmey, S. Gehrke, B. Kirchner, ChemSusChem 2018, 11, 1900.

[11] B. Gorska, L. Timperman, M. Anouti, F. Beguin, Phys Chem Chem Phys 2017, 19, 11173.

[12] Y. L. Zhang, R. J. Ye, D. Henkensmeier, R. Hempelmann, R. Y. Chen, Electrochim Acta 2018, 263, 47.

[13] W. W. Liu, X. B. Yan, J. W. Lang, Q. J. Xue, J Mater Chem 2011, 21, 13205.

[14] P. Wuamprakhon, R. Donthongkwa, K. Hantanasirisakul, V. Promarak, J. Limtrakul, M. Sawangphruk, Chem Commun (Camb) 2021, 57, 13712.

[15] C. A. Angell, N. Byrne, J. P. Belieres, Acc Chem Res 2007, 40, 1228.

[16] W. Xu, E. I. Cooper, C. A. Angell, The J. Phys. Chem. B. 2003, 107, 6170.

[17] L. Dick, T. Stettner, Y. X. Liu, S. Q. Liu, B. Kirchner, A. Balducci, Energy Storage Mater 2022, 53, 744.

[18] A. Mariani, M. Bonomo, X. P. Gao, B. Centrella, A. Nucara, R. Buscaino, A. Barge, N. Barbero, L. Gontrani, S. Passerini, J. Mol. Liq. 2021, 324, 115069.

[19] M. Yu, D. Lin, H. Feng, Y. Zeng, Y. Tong, X. Lu, Angew Chem Int Ed Engl 2017, 56, 5454.

Chapter 4 Ionic liquid-based electrolytes for Porous $RuO_xN_yS_z$ and 3D MnO_2-based MSCs

4.1 Introduction of $RuO_xN_yS_z$ and MnO_2

In this chapter, we looked into additional metal-oxide-based pseudocapacitive materials that could be used as micro-supercapacitor electrodes. $RuO_xN_yS_z$ and MnO_2 were chosen as the active materials. The $RuO_xN_yS_z$ electrode is an N and S-doped ruthenium oxide electrode, whereas the MnO_2 electrode is a well-known pseudocapacitive electrode from the metal-oxide family. To maximize the energy storage capability using these electrodes, we created the proper ionic-liquid-based electrolytes.

4.1.1 $RuO_xN_yS_z$

Ruthenium dioxide is well known for having extremely high specific pseudocapacitance due to its ability to undergo reversible rapid redox reactions involving multiple valence states [1]. Furthermore, it has excellent electronic conductivity, which is required for a stable supercapacitor electrode with a low overall impedance. Because of these intriguing properties, many groups have attempted to incorporate RuO_2 in various intriguing configurations to tap the enormous potential in supercapacitors [2], [3] as well as in battery applications [4], [5]. The material for the fabrication of high-energy/power electrodes for micro-supercapacitors in the current study was a new ruthenium oxide-based material (i.e., hetero atom incorporated ruthenium oxide, $RuO_xN_yS_z$). The presence of heteroatoms such as N and S in the RuO_x framework not only affects the microstructure and surface area, but can also improve electrolyte wettability and provide better access to active sites in supercapacitors [6].

4.1.1.1 Deposition of $RuO_xN_yS_z$ on Au DHBT substrate

A Ti(100 nm)/Au(300 nm) thin film was deposited by evaporation on an oxidized silicon substrate and electrochemically pre-treated by cycling the potential at a scan rate of 100 mV/s between -0.3 and +1.7 V versus saturated calomel electrode (SCE) in 1 M H_2SO_4 until a stable voltammogram was obtained. Porous metallic current collectors were prepared using the dynamic hydrogen bubble template (DHBT) technique from an optimized solution of 2 x 10^{-3} M of $HAuCl_4.3H_2O$ in 3 M H_2SO_4 by applying 5 A/cm^2 for 20 min in a 3-electrode configuration. Because of its simplicity and ease of preparation, DHBT is easily transferable to the pilot production line in microelectronic facilities. As mentioned in the previous chapter, porous metallic current collectors are also ideal for loading pseudocapacitive materials like RuO_2 [2]. The porous Au film was then washed several times in de-ionized water and used as a current collector for subsequent deposition of novel RuO_x-based material for MSCs. Electrodeposition of hydrous RuO_2 has been evaluated in the past by different techniques including cyclic voltammetry [7], anodic [8], and cathodic [9] polarization in static as well as pulsed configurations. Out of all the techniques, pulsed techniques provided the best results for supercapacitive applications [10]. Although pulsed potential methods may appear to be more controllable, pulsed current configurations are more versatile because they can be easily scaled up industrially without the use of a reference electrode. Hence, we investigated pulsed current electrodeposition of hydrous RuO_x-based material on porous Au substrates. Furthermore, the majority of the reported protocols used $RuCl_3$-based precursors, owing to their well-understood chemistry in aqueous media. [11]. However, due to the high potential complexation of Cl^- with Au, $RuCl_3$ was not compatible with the porous Au substrates prepared by DHBT, so we screened several other salts and chose $[Ru(NO)]_2(SO_4)_3$ for plating hydrous $RuO_xN_yS_z$. A 10 mM of ruthenium nitrosyl sulfate

$[Ru(NO)]_2(SO_4)_3$ was dissolved in 100 mL of 0.025 M K_2SO_4 and 0.004 M H_2SO_4. Prior to electrodeposition, the electrolyte bath was de-aerated for 20 minutes with N_2 bubbling.

The linear sweep voltammetry (LSV) profile of the Au current collector in the electrolyte bath revealed two distinct interfacial processes, an initial gold oxidation peak (visible in the solution even without the Ru salt), and nitrosyl sulfate (NS) salt-precursor oxidation. **(Figure 4.1 a)**. The current for the pulse was chosen to cover both these processes. A galvanostatic pulse of 7 mA cm^{-2} for 10 sec (optimized for porous substrates from LSV studies) was followed by a rest period of 30 s to stabilize/equilibrate the porous structure/electrolyte interface **(Figure 4.1 b)**. The total pulse time determined the actual content of $RuO_xN_yS_z$ on the substrates and increased pulse period depositions (1 h, 2 h, 3 h, etc.) were performed to have higher active material loading. The bare porous gold structure had a thickness of ~ 50-60 µm and the samples with the highest loading (4 hours of pulsed deposition) had a thickness of ~ 160 µm.

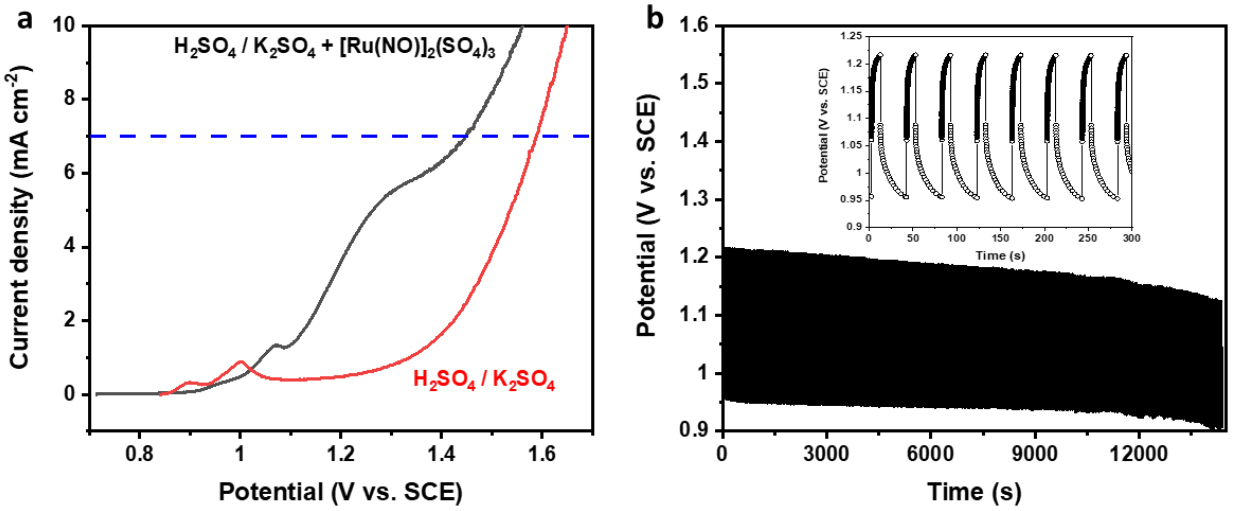

Figure 4.1: (a) Linear sweep voltammetry (LSV) studies showing different interfacial processes during the potential scan rate of 10 mV s^{-1}. The dotted line indicates the current density corresponds to the oxidation of nitrosyl sulfate (NS) salt-precursor. (b) Evolution of potential time curve during 4 hours of deposition.

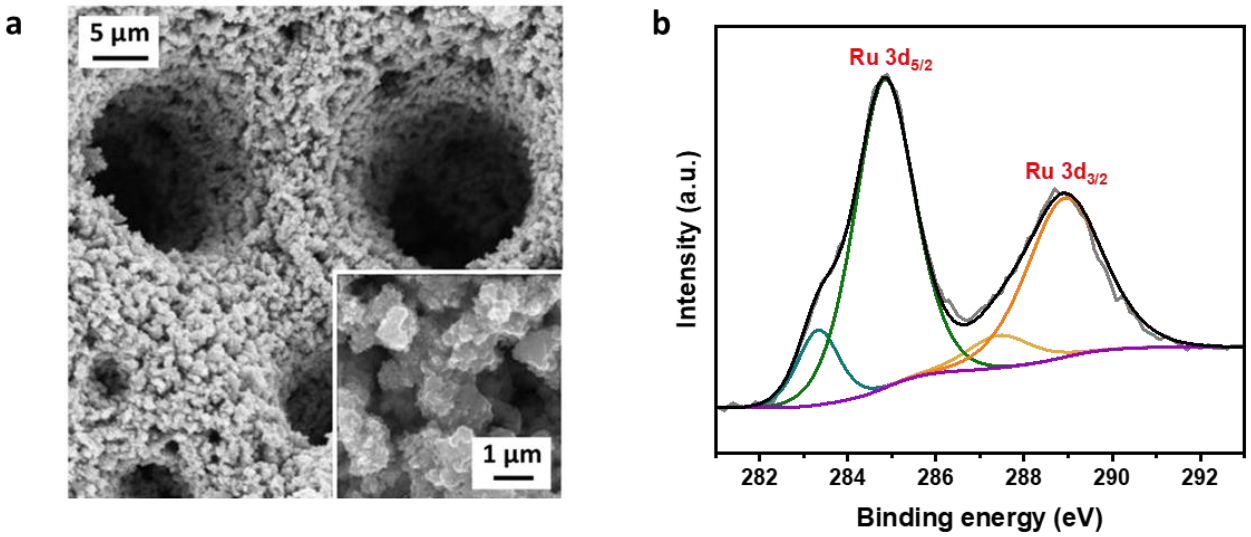

Figure 4.2: (a) SEM micrographs at different magnifications after 4 hours of deposition. (b) Ru-3d core-level XPS spectrum of the deposited material.

The morphology and structure of the $RuO_xN_yS_z$ electrodes are analyzed using SEM, EDAX, and XPS techniques. **Figure 4.2 a** shows the microstructure of the deposited samples which have the original DHBT structure retained but with flaky RuO_x-based deposits over the dendritic Au structure. It is worth noting, however, that even after extended deposition times, neither the large nor the smallest pores of the porous substrates are blocked by the active material. Such conformal deposition is required to fully exploit the benefits of 3D nanostructuring and achieve higher energy density. The XPS Ru-3d core level spectra of the deposited $RuO_xN_yS_z$ is given in **Figure 4.2 b**. The conformal deposition of the Ru-based active material over the entire porous Au structure is further confirmed using elemental mapping through energy-dispersive X-ray analysis (EDAX) as shown in **Figure 4.3**.

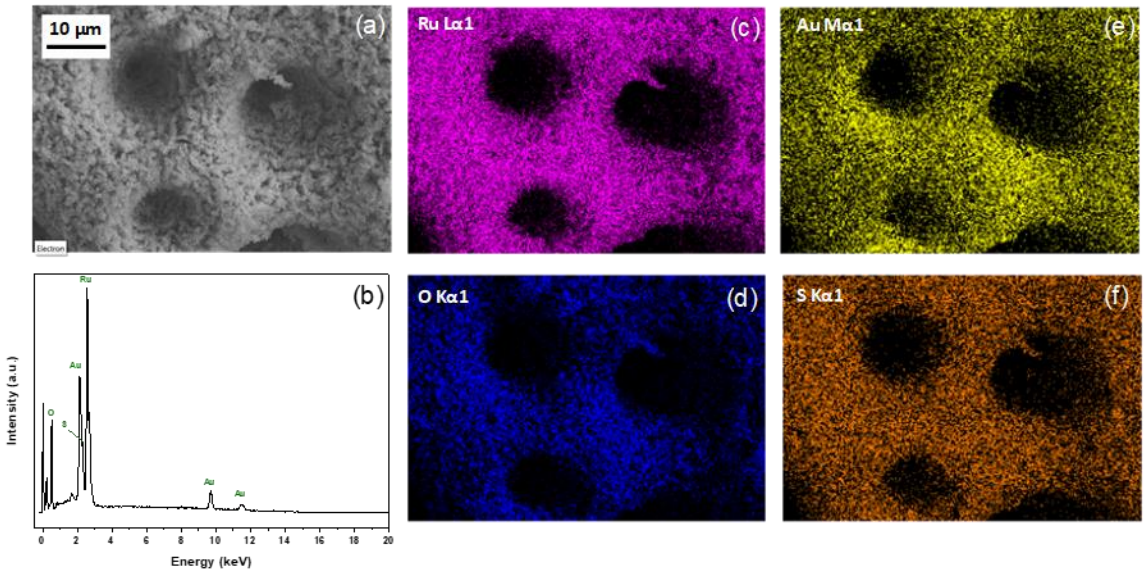

Figure 4.3: (a) SEM image and (b) EDAX spectrum of porous $RuO_xN_yS_z$ after 4 h of deposition. (c), (d), (e), and (f) Elemental mapping showing conformal deposition of Ru species on porous gold surface. Trace contents of other elements including sulfur and oxygen are also observed, which might be oxidative side products from the salt precursor $[Ru(NO)]_2(SO_4)_3]$ utilized for electrodeposition.

4.1.2 MnO_2

Pseudocapacitive micro-supercapacitors are a type of electrochemical capacitor that uses rapid and reversible faradaic surface reactions to store charge [12]. Ru-based micro-supercapacitors have greater power and cycling stability and can give an energy density per unit footprint area that is quite similar to lithium-based micro-batteries [2]. These micro-devices are now restricted to specialized uses due to the high and unstable price of ruthenium as well as the environmental problems associated with its mining and processing. For commercial scale-up, replacing ruthenium with alternative transition metals with greater abundance and lower cost is essential. Manganese dioxide MnO_2 stands out among other pseudocapacitive materials because to its high theoretical specific capacitance, widespread availability, and environmental friendliness [13], [14].

Various crystallographic structures exhibited by the MnO_2 are depicted in **Figure 4.4**. MnO_2 microstructures consist of a series of allotropic forms based on MnO_6 octahedra building blocks. MnO_6 units may share their corners, faces, and edges to build various structures: channeled (1D), layered (2D), or interconnected (3D) tunnels. Depending on the number of MnO_6 units in the MnO_2 unit cell, different sizes of the channel cavity may be obtained.

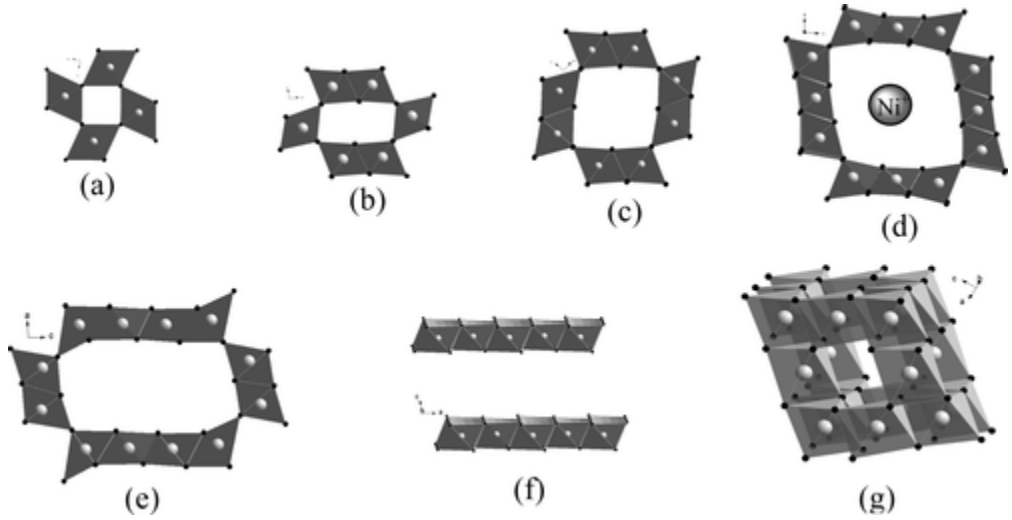

Figure 4.4: Crystallographic structures of MnO_2. **a,** pyrolusite. **b**, ramsdellite. **c**, cryptomelane. **d**, Ni-todorokite. **e**, OMS-5. **f**, birnessite. **g**, spinel. [15].

In aqueous electrolytes, the general charge/discharge mechanism in MnO_2-based supercapacitors may be described by the following reaction:

$$MnO_2 + M^+ + e^- \leftrightarrow MnOOM$$

where M represents hydrated protons (H_3O^+) and/or alkali cations such as K^+, Na^+, and Li^+. The general reaction mechanism implies an adsorption/desorption process of cations at the material surface and/or an insertion/extraction process of cations into the material bulk [15].

Although its capacitance is lower than that of the eminent RuO_2, manganese is the fifth most abundant metal in the Earth's crust making its price derisory compared to the overpriced ruthenium

oxide in trace amount. However, MnO_2 suffers from low conductivity, inefficient electron transport and ion diffusion, and low structural stability, which results in low electrochemical utilization and poor cycling life [16].

4.1.2.1 Deposition of MnO_2 on Ni DHBT substrate

At first, deposition of Ti(100 nm)/Ni(200nm) thin film is obtained by evaporation on an oxidized silicon substrate. The porous DHBT Ni as current collector is produced in a bath solution of 0.1 M NiCl / 2 M NH_4Cl by applying a constant current density of 2 A cm^{-2}. The electrodeposition of MnO_2 was carried out on Ni DHBT substrate from 0.14 M $MnSO_4$ solution by applying a pulse of 1.25 V (vs SCE) for 2 s followed by an open circuit potential (OCP) of 3 s.

Highly porous Ni current collectors were created using the previously mentioned DHBT method, which is a simple and scalable electrodeposition process on oxidized Si wafers. The MnO_2 active material was then electrodeposited on the highly structured nickel current collector using a pulsed current technique. The XPS Mn 2p spectra for the deposited MnO_2 is shown in **Figure 4.5**.

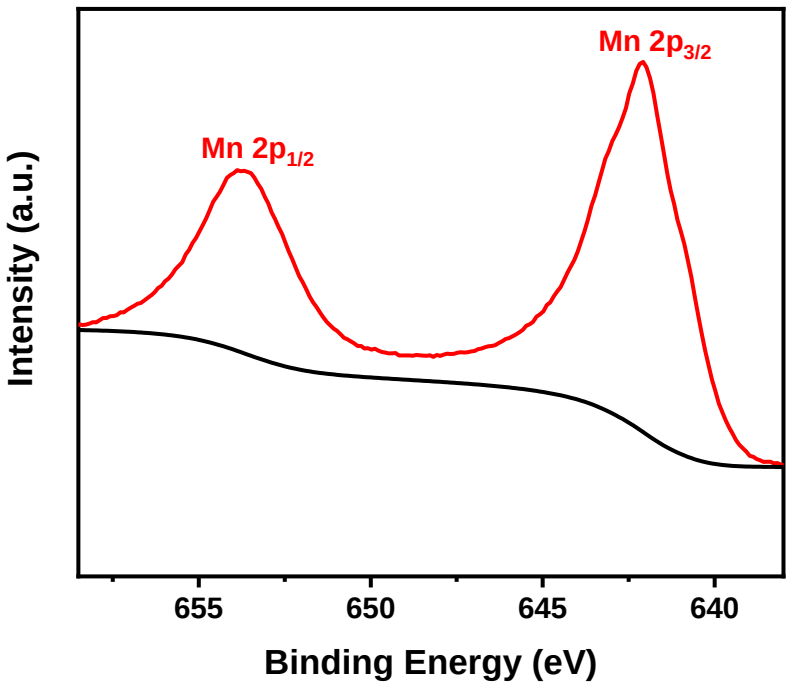

Figure 4.5: XPS spectrum (Mn-2p) corresponds to the deposited MnO_2.

4.2 Choice of Ionic liquids for $RuO_xN_yS_z$ and MnO_2

Based on the electrode characteristics, the IL solvents and appropriate salts containing the charge carrier ions were rationally developed. The $RuO_xN_yS_z$ electrode is more similar to the RuO_2 electrode in that H^+ ions can enable charge transfer, whereas Na^+-containing solvents are the best choice for charge storage in the MnO_2 electrode.

4.2.1 Proton conducting additive-doped IL for $RuO_xN_yS_z$ MSC

We chose an aprotic ionic liquid solvent (1-ethyl-3-methylimidazolium bis(trifluoromethylsulfonyl)imide (EMIM-TFSI)) doped with proton conducting SiWa additive to develop $RuO_xN_yS_z$ micro-supercapacitors with a wider cell voltage **(Figure 4.6)**. While H^+ ions from SiWa can promote surface redox reactions via proton-coupled electron transfer, the EMIM-TFSI allows the redox process to have a wider stability window.

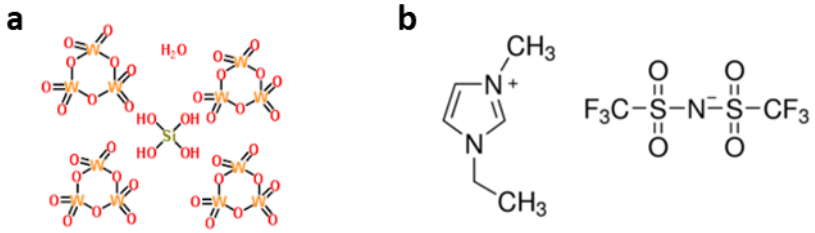

Figure 4.6: Structures of the cation and anion groups of ionic liquid candidates explored for $RuO_xN_yS_z$ micro-supercapacitors. (a) Proton-conducting salt, SiWa. (b) Ionic liquid electrolyte.

4.2.2 Na salt containing ILs for MnO_2 MSC

Since electrolytes containing Na^+ ions are expected to cause pseudocapacitive charge storage in MnO_2, we have synthesized and tested electrolytes using Na salts diluted in aprotic pyrrolidinium- and imidazolium-based ionic liquids solvents **(Figure 4.7)** for MnO_2 electrodes.

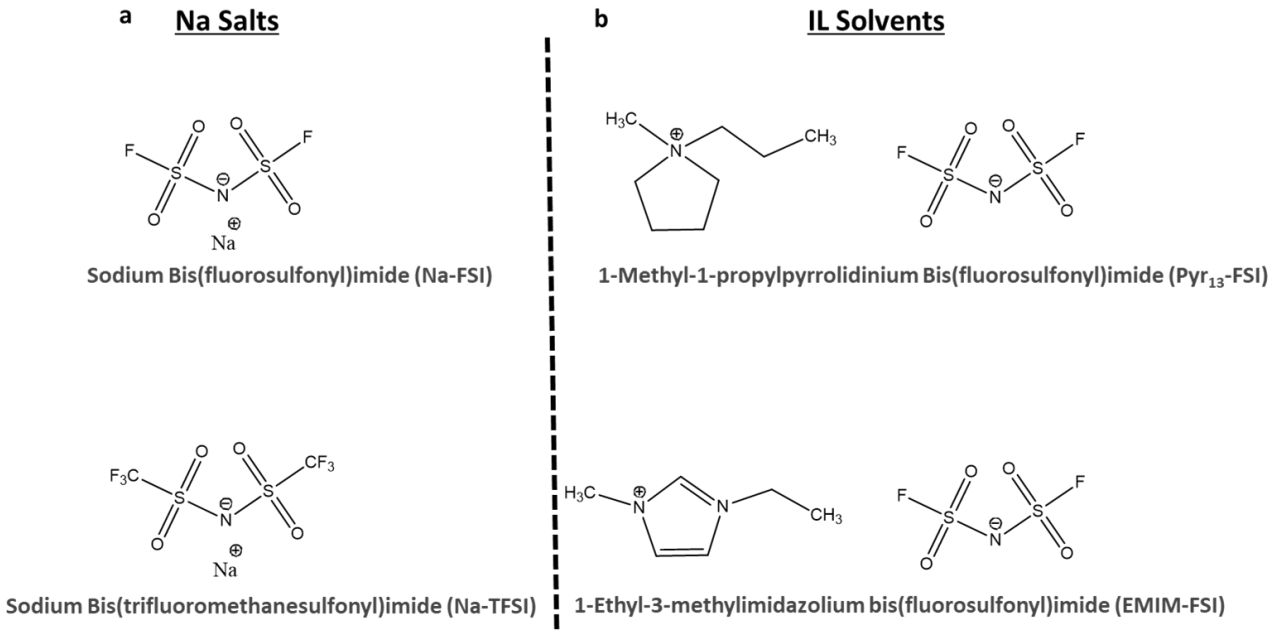

Figure 4.7: Structures of the cation and anion groups of ionic liquid candidates explored for MnO_2 micro-supercapacitors. (a) Na salts. (b) Ionic liquids solvents.

The purpose of comparing NaFSI and NaTFSI was to see if ion transport (and viscosity) affects charge storage properties. Because of the greater mobility of the smaller ion, FSI^- anions have higher conductivities.

The EMIM-FSI and Pyr_{13}-FSI solvents were selected because of their low viscosity values (25 and 53 cP, respectively). $EMIM^+$ cation has better charge transport characteristics but the acidic proton at the C_2 position (the carbon atom between the two N atoms on the cycle) can make them less stable at lower potentials. Because the absence of acidic protons and conjugation on the cycle reduces reactivity, pyr_{13}^+ cation has been used more successfully as a battery electrolyte [23].

4.3 Electrochemical study of 3D $RuO_xN_yS_z$ and 3D MnO_2 MSCs

The electrochemical characterization results of 3D $RuO_xN_yS_z$ and 3D MnO_2 MSCs using aqueous and ionic liquid-based electrolytes are provided in the following section.

4.3.1 Electrochemical study of 3D $RuO_xN_yS_z$ MSCs in aqueous electrolyte

In this section, electrochemical characterization results of the 3D $RuO_xN_yS_z$ MSCs using aqueous electrolyte (0.5 M H_2SO_4), PVA-doped gel electrolyte, and ionic liquid-based electrolyte (SiWa- doped EMIM-TFSI) are provided in greater detail.

We first studied the electrochemical performance $RuO_xN_yS_y$ electrodes in a three-electrode configuration using 0.5 M H_2SO_4 electrolyte to evaluate the charge storage properties of this new material in a conventional electrolyte. To optimize the capacitive performance of porous $RuO_xN_yS_y$, different pulse durations during the deposition step were explored. **Figure 4.8 a** shows representative cyclic voltammograms (CVs) for capacitive performances of different samples with increased active material loadings. Higher specific capacitance was observed with an increase of

active materials while retaining the capacitive profile at a given scan rate. The electrode exhibits an extremely high capacitance of 8.5 F cm^{-2} when cycled at 5 mV s^{-1}, which is to our knowledge the highest value ever reported for a micro supercapacitor electrode.

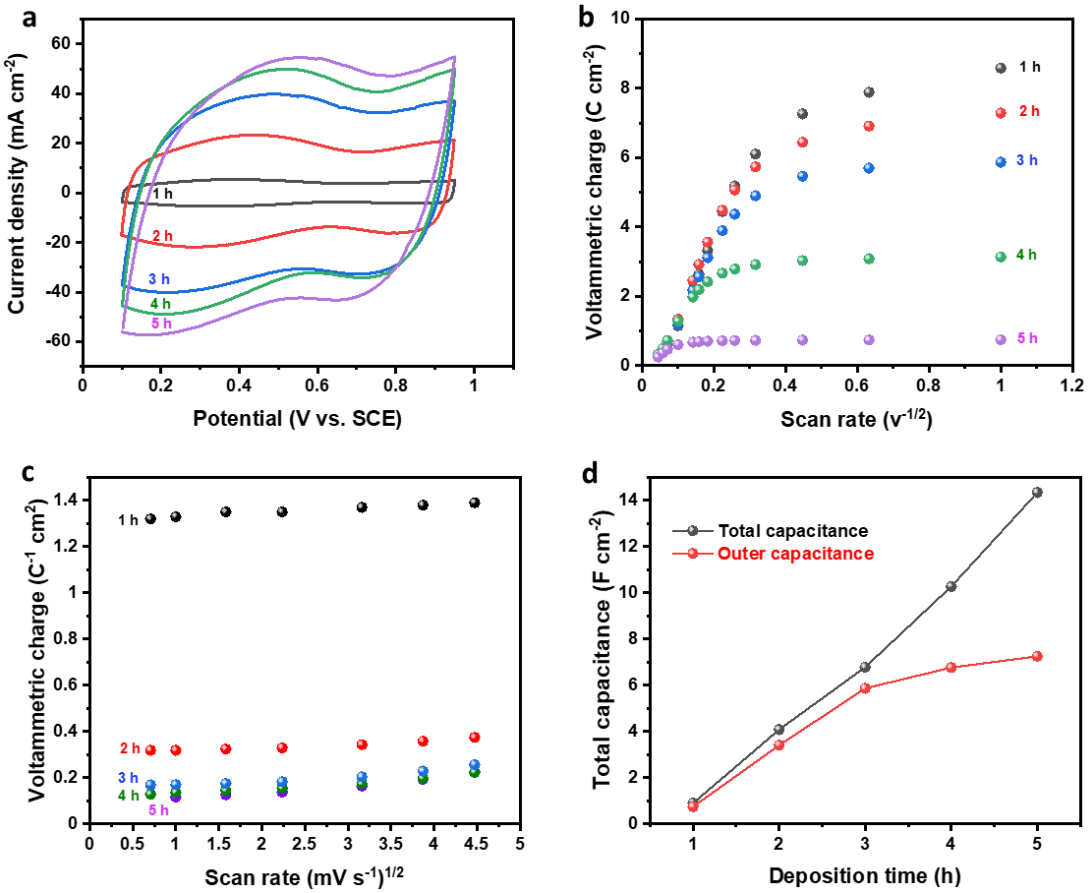

Figure 4.8: Electrochemical study of porous $RuO_xN_yS_z$ as micro-supercapacitor electrode. (a) Cyclic voltammetry profiles of electrodes after different deposition durations in 0.5 M H_2SO_4. (b) Determination of the outer charge, q_{outer}, of different electrodes obtained by calculating average voltammetric charge, q*, as a function of sweep rate v. (c) Determination of the total charge, q_{total}, of the electrodes. (d) Evolution of total capacitance, Ct, and outer capacitance, Co, after different deposition durations.

We also conducted CV studies at various sweep rates (ranging from 0.5 to 500 mV s^{-1}) to better understand charge accessibility in various samples (**Figures 4.8 b and c**). We were able to achieve a record value of 14.3 F cm^{-2} for 5 hours of total pulse time deposition by systematically varying the loading (**Figure 4.8 d**). Outer charge contribution (q_{outer}) accounted for more than 80% of the

total charge stored (q_{total}), indicating that the majority of the deposited material was in direct contact with the electrolyte. However, the difference between the q_{outer} and q_{total} curves progressively increased as deposition time was increased, indicating relatively lower charge accessibility in thicker layers of $RuO_xN_yS_z$ despite overall higher specific capacitance.

Galvanostatic charge-discharge (GCD) measurements were used to assess the areal capacitance of the porous electrodes (**Figure 4.9**) with improved charge accessibility (3 h deposition). Little voltage hysteresis between charge and discharge was visible in GCD profiles at various current densities, which is a feature of pseudocapacitive materials [24]. The areal capacitance of the micro-supercapacitor electrode was calculated from the GCD curve to be 6.6 F cm^{-2} at a current density of 10 mA cm^{-2}, and 5.0 F cm^{-2} at a current density of 100 mA cm^{-2}, retaining 75% of the initial capacitance even after a tenfold increase in current.

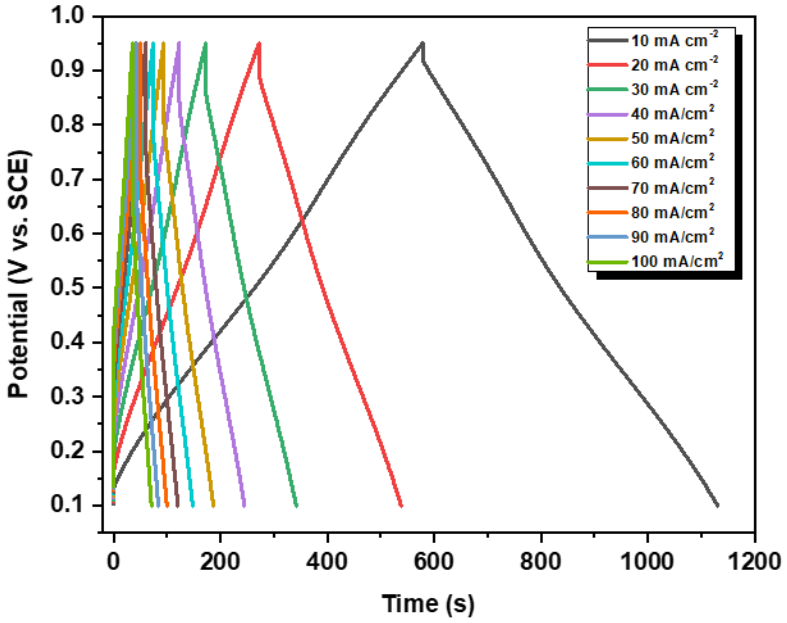

Figure 4.9: Galvanostatic charge-discharge (GCD) profiles of porous RuOxNySz (3 hours deposition) at different currents.

Such high area-specific capacitance has not previously been reported with 3D electrodes for RuO_2-based materials, to our knowledge. The use of this strategy in full 3D interdigitated devices will be especially interesting for high-energy micro-supercapacitors in a variety of niche applications.

4.3.2 Electrochemical study of 3D $RuO_xN_yS_z$ in solid-state and IL-based MSC

To evaluate the performance of $RuO_xN_yS_z$ electrode material in a real device, we developed an interdigitated all-solid-state micro-supercapacitor that is integrated into a silicon wafer. An oxidized silicon wafer was initially patterned with a thin metallic Ti/Au sublayer using traditional photolithography and lift-off methods. The DHBT approach was then used to selectively electrodeposit porous gold current collectors onto the conductive portions. The thickness and aspect ratio AR (defined as the ratio of the electrochemically active surface area to the geometrical surface area) of the metallic current collector were ca. 30 μm and 374 cm^2 cm^{-2}, respectively. After that, $RuO_xN_yS_z$ was electrodeposited onto the 3D conducting current collector that was created. We studied the electrochemical behavior of the MSC device with $RuO_xN_yS_z$ electrodes using poly(vinyl alcohol) (PVA)-based gel electrolyte as well as in [EMIM][TFSI] ionic liquid (1-ethyl-3-methylimidazolium bis(trifluoromethylsulfonyl)imide) doped with SiWa electrolyte.

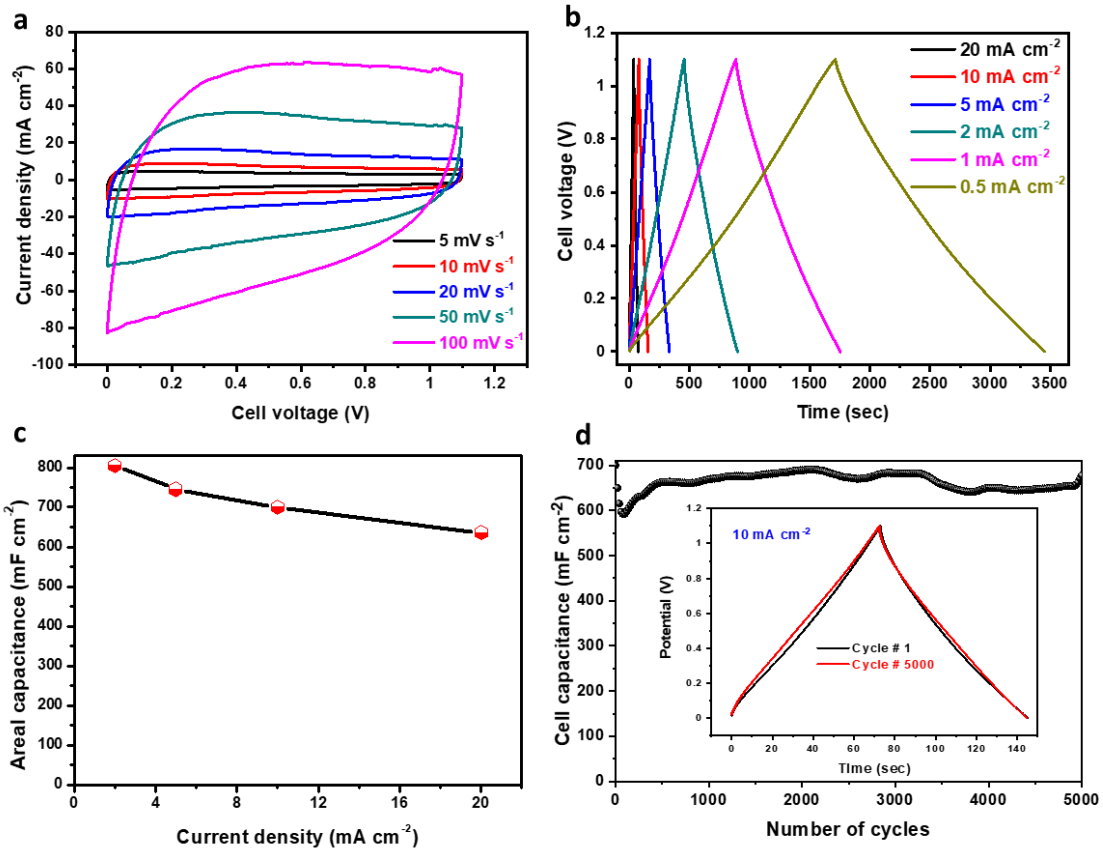

Figure 4.10: Electrochemical characterisation of an all-solid-state interdigitated porous $RuO_xN_yS_z$ MSC (electrolyte: PVA-H_2SO_4-SiWa). (a) Cyclic voltammograms at different scan rates and (b) and GCD curves at different current densities. (c) Rate performance at different current densities. (d) Cycling stability study at 10 mA cm^{-2}. The inset shows 1st and 5000th GCD curve.

Figure 4.10 a show the CV curves obtained from an all-solid-state MSC tested in the PVA-doped gel electrolyte at varying scan rates. Within an operating cell voltage of 1.1 V, the CVs demonstrated the reversibility of the redox reaction. The solid-state micro-supercapacitor has an impressive cell capacitance of 714 mF cm^{-2} at 5 mV s^{-1}. The non-linear GCD curves with long discharge times at lower current densities indicate the all-solid-state MSC device's superior charge storage and delivering potential (**Figure 4.10 b**). The rate performance of the microdevice is shown by plotting areal capacitance vs. current densities **(Figure 4.10 c)** with a maximum areal capacitance performance of 805 mF cm^{-2} at 2 mA cm^{-2}. Repeated galvanostatic charge-discharge

cycles at a high current density of 10 mA cm^{-2} were used to test the solid-state microdevice's long-term cycling behavior (**Figure 4.10 d**). Even after 5000 cycles, the device exhibits stable cycling performance with almost no loss of specific capacitance and identical symmetrical triangular curves for all cycles.

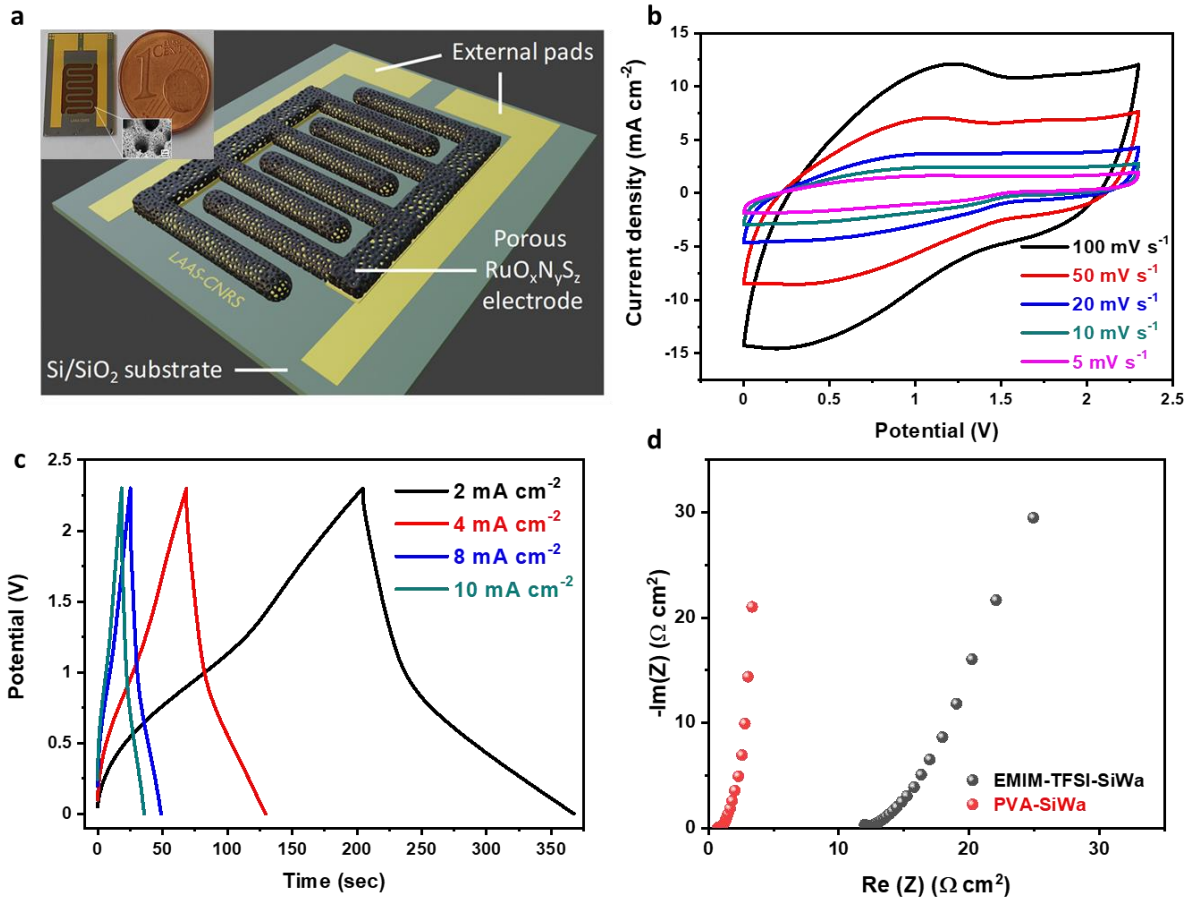

Figure 4.11: Electrochemical characterization of interdigitated porous $RuO_xN_yS_z$ micro-supercapacitor tested with SiWa-doped EMIM-TFSI electrolyte. (a) Schematic and photograph (inset) of an interdigitated porous micro-supercapacitor before encapsulation. Cyclic voltammograms at different scan rates (c) and GCD curves at different current densities tested in doped [EMIM][TFSI]. (d) Nyquist plot of the porous interdigitated $RuO_xN_yS_z$ micro-supercapacitors based on doped PVA and doped EMIM-TFSI electrolytes.

The CV curves at different scan rates for the interdigitated porous $RuO_xN_yS_z$ MSC tested with the doped [EMIM][TFSI] revealed an extended cell voltage of up to 2.3 V with no visible electrolyte or electrode degradation (**Figure 4.11 b**). Within the enlarged voltage window, the

GCD curves at various current densities displayed typical pseudocapacitive signatures (**Figure 4.11 c**). According to the Nyquist plot, the all-solid-state interdigitated porous $RuO_xN_yS_z$ MSC with PVA-based gel electrolyte had a very low equivalent series resistance (ESR) of 0.7 Ω cm^2 (**Figure 4.11 d**). No leakage current is seen, with a near vertical straight line in the low-frequency region, as expected for a pseudocapacitive material. The specific energy density reached a value of 432 mJ cm^{-2} and a maximum power density of 421 mW cm^{-2}. Although the $RuO_xN_yS_z$ micro-supercapacitor tested with SiWa-doped EMIM-TFSI electrolyte achieves a high voltage, it comes at the expense of a lower cell capacitance and higher ESR. In this case, the energy and power density attained are 460 mJ cm^{-2} and 110 mW cm^{-2}, respectively.

4.3.3 Electrochemical study of 3D MnO_2 MSCs using ILs

When aqueous electrolytes are used, it limit the operating cell voltage due to water breakdown and partial dissolution of MnO_2 into soluble MnOOH species above about 1 volt. Although the energy stored is directly proportional to the square of the cell voltage, developing enhanced solid-state electrolytes with an expanded electrochemical stability window (ESW) for Na^+ charge storage is a significant challenge. Previously, we demonstrated that protic ionic liquids could be used to generate a high pseudocapacitive effect of RuO_2 with extended ESW [38], [39]. Ionic liquids are considered safe alternatives to conventional aqueous and organic electrolytes due to their non-flammability, low volatility, high ionic conductivity, and widened potential windows. Furthermore, ionic liquids can be easily converted to a quasi-solid state by developing ionogels and overcoming the challenges of micro-supercapacitor packaging [40], [41]. In this work, we developed and tested several electrolytes for 3D MnO_2 MSCs using Na salts diluted in aprotic pyrrolidinium and imidazolium-based ionic liquid solvents (Na salts (Na-FSI and Na-TFSI) & ionic liquid solvents (Pyr_{13}-FSI and EMIM-FSI)) as MnO_2 does not require H^+ and alkali ions are

often used. The electrochemical CV and EIS results are shown in **Figure 4.12**. We observed no discernible variation in the performances of the MnO_2 micro-supercapacitor (cell voltage and rate performance) between the various examined ionic liquids. Hence, we believe that rather than electrolyte ion transport itself, the restrictions appear to be caused by interfacial interactions and/or ion transport within the active material. Also, it doesn't appear that the potential limitations are too strict for the $EMIM^+$ cation to react (i.e., the negative limit is not sufficiently negative for $EMIM^+$ to react) for a difference to be seen with the $Pyr13^+$. These findings clearly demonstrate that the chosen Na salt-based ionic liquid electrolytes have the potential to improve the energy density performance of MSCs using MnO_2 electrodes.

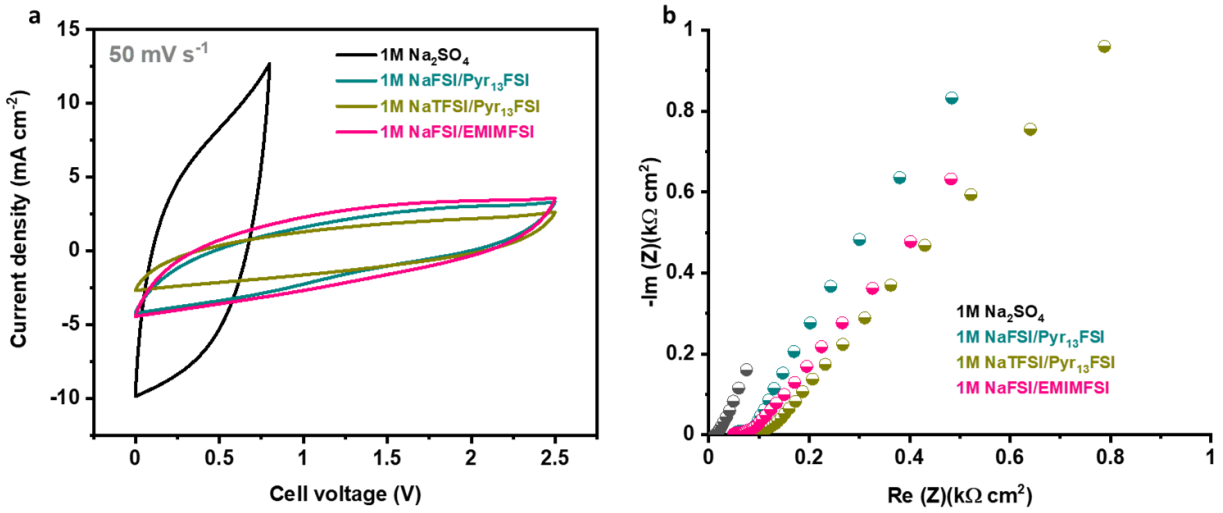

Figure 4.12: Electrochemical performance of MSC with thin film of Ni / MnO_2 electrodes (5 min Ni DHBT + 1000 cycles of MnO_2). (a) CV curves at 50 mV s^{-1} tested in 1M Na_2SO_4 and Na-based ionic liquid electrolytes and (b) corresponding EIS graphs from 100 kHz to 10 mHz.

Next, we performed the MnO_2 micro-supercapacitor charge storage using 1 M sodium bis(fluorosulfonyl)imide (NaFSI) salt diluted in aprotic 1-methyl-1-propylpyrrolidinium bis(fluorosulfonyl)imide ($Pyr_{13}FSI$) ionic liquid. It is worth noting that ionic liquids based on FSI^- anions are known to be chemically stable and to have a low viscosity, which often correlates with good ionic conduction. [43], [44] **Figure 4.13 a** shows CV curves obtained at 2 mV s^{-1} with

successively increasing the cell voltage windows from 0 to 2.6 V. The micro-supercapacitor was able to cycle up to 2.6 V without displaying any symptoms of active material deterioration or electrolyte oxidation. The pseudocapacitive CVs suggest that the main source of faradaic current may be the Na^+ ion. [42] In addition, the micro-supercapacitor is shown to be noticeably stable within this voltage range by the plot of charge ratio ($Q_{anode}/Q_{cathode}$) vs. the cell voltage **(Figure 4.13 b)**.

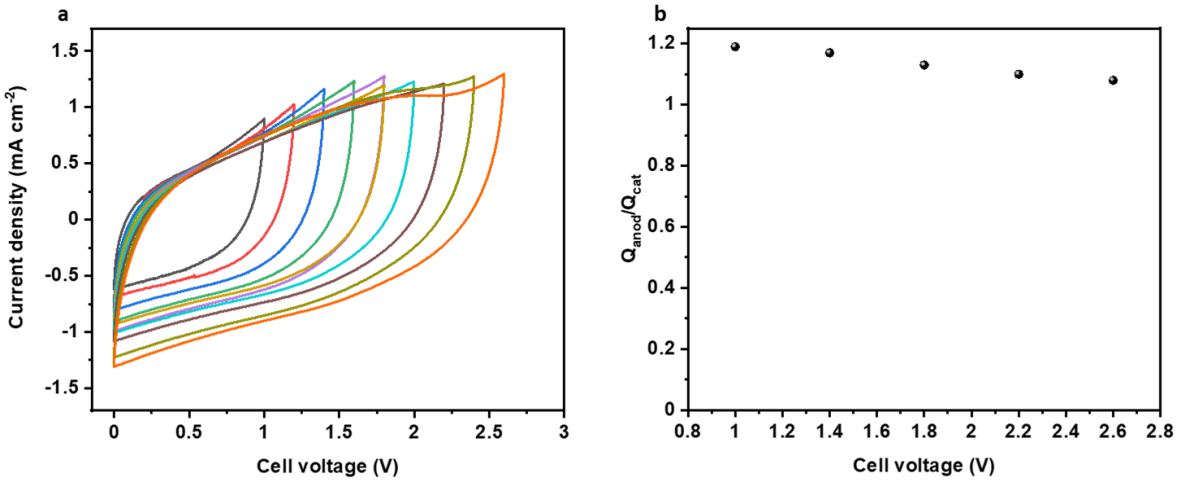

Figure 4.13: MSC Cell performance using ionic liquid electrolyte. (a) CV curves with increasing cell voltage tested in 1 M NaFSI /Pyr_{13}FSI ionic liquid at 2mV s^{-1}. (b) Ratio of voltammetric charge ($Q_{anodic}/Q_{cahodic}$) with cell voltage increase from 1 to 2.6V in 1 M NaFSI /Pyr_{13}FSI.

Figure 4.14 depicts the cycling performance of micro-supercapacitors up to 2000 cycles tested in aqueous and ionic liquid electrolytes. With NaFSI/Pyr_{13}FSI, a very high level of stability is seen after the initial minor increase in capacitance, which is attributed to the electrolyte's slow penetration into the porous electrode and effective utilization of the active surface. Over all, the electrochemical performance of MnO_2 micro-supercapacitors hold promise for their potential future applications.

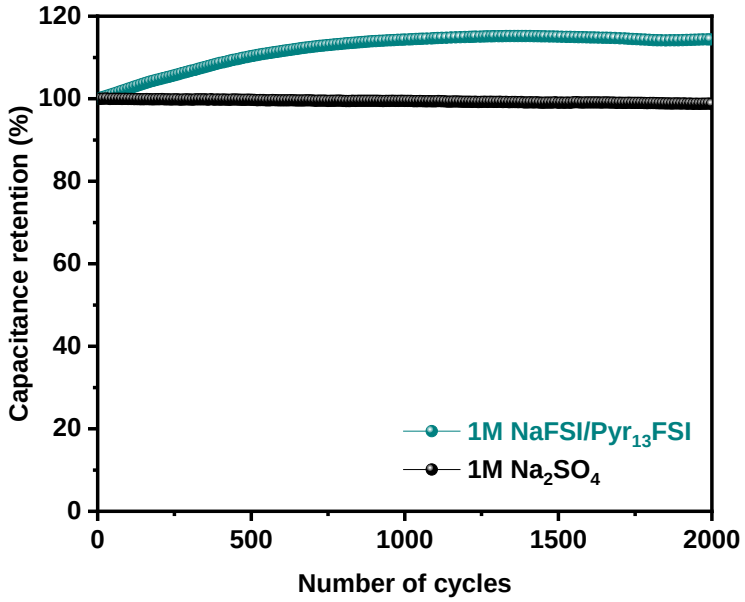

Figure 4.14: Cycling stability study of 3D MnO_2 MSCs tested using 1 M Na_2SO_4 and 1 M NaFSI /Pyr_{13}FSI electrolytes at 2 mA cm^{-2}.

4.4 Conclusion

In conclusion, conformal $RuO_xN_yS_z$ electrodeposition at ambient temperature has been achieved on 3D porous current collectors with a very large surface area. The supercapacitor using 3D $RuO_xN_yS_z$ electrodes showed high capacitance of > 10 F cm^{-2} with remarkable stability for over 5000 cycles. These electrodes can be easily integrated with current microfabrication processes for a variety of microsystems as well as for brand-new forthcoming applications in the IoT era because to their easy simple electrodeposition fabrication method. To extend the lifespan, increase storage capacity, and improve electrochemical performance, these electrodes can be further combined with solid electrolytes or ionic liquids. With the right counter electrode materials, they can also be imagined in 3D stacked interdigitated structures, offering outstanding energy/power density micro-energy solutions for innovative microsystems.

Next, we have demonstrated the possibility of realizing micro-supercapacitor using MnO_2-based electrodes exhibiting extended operational potential window, long lifetimes and superior

charge storage. To realize this, we have rationally designed the electrolytes by combining Na-salts and aprotic ionic liquid media. MnO_2 MSC employing NaFSI/Pyr_{13}FSI ionic liquid electrolyte demonstrated stability window of more than three times with exceptional areal energy density performance when compared to reported aqueous electrolytes. In addition, the safety and effective encapsulation by ion confinement characteristics of electrolytes based on ionic liquids show that MnO_2 MSCs are feasible for use in upcoming commercial applications.

4.5 References

[1] Q. Li, S. S. Zheng, Y. X. Xu, H. G. Xue, H. Pang, Chem Eng J 2018, 333, 505.

[2] A. Ferris, S. Garbarino, D. Guay, D. Pech, Adv Mater 2015, 27, 6625.

[3] K. Brousse, S. Pinaud, S. Nguyen, P. F. Fazzini, R. Makarem, C. Josse, Y. Thimont, B. Chaudret, P. L. Taberna, M. Respaud, P. Simon, Adv. Energy Mater. 2019, 10, 1903136.

[4] S. H. Choi, J. S. Kim, Y. S. Yoon, Electrochim Acta 2004, 50, 547.

[5] K. E. Gregorczyk, A. C. Kozen, X. Chen, M. A. Schroeder, M. Noked, A. Cao, L. Hu, G. W. Rubloff, ACS Nano 2015, 9, 464.

[6] C. H. Yang, W. X. Que, Y. Tang, Y. P. Tian, X. T. Yin, J. Electrochem. Soc. 2017, 164, A1939.

[7] C. C. Hu, Y. H. Huang, J. Electrochem. Soc. 1999, 146, 2465.

[8] C.-C. Hu, M.-J. Liu, K.-H. Chang, J Power Sources 2007, 163, 1126.

[9] B. O. Park, C. D. Lokhande, H. S. Park, K. D. Jung, O. S. Joo, J Mater Sci 2004, 39, 4313.

[10] R. K. V. Prataap, R. Arunachalam, R. P. Raj, S. Mohan, L. Peter, Curr Appl Phys 2018, 18, 1143.

[11] J. J. Jow, H. J. Lee, H. R. Chen, M. S. Wu, T. Y. Wei, Electrochim Acta 2007, 52, 2625.

[12] C. Choi, D. S. Ashby, D. M. Butts, R. H. DeBlock, Q. Wei, J. Lau, B. Dunn, Nat Rev Mater 2019, 5, 5.

[13] W. Wei, X. Cui, W. Chen, D. G. Ivey, Chem Soc Rev 2011, 40, 1697.

[14] S. Boyd, K. Ganeshan, W. Y. Tsai, T. Wu, S. Saeed, D. E. Jiang, N. Balke, A. C. T. van Duin, V. Augustyn, Nat Mater 2021, 20, 1689.

[15] O. Ghodbane, J. L. Pascal, F. Favier, ACS Appl Mater Interfaces 2009, 1, 1130.

[16] Y.-C. Hsieh, K.-T. Lee, Y.-P. Lin, N.-L. Wu, S. W. Donne, J Power Sources 2008, 177, 660.

[17] B. J. Plowman, L. A. Jones, S. K. Bhargava, Chem Commun (Camb) 2015, 51, 4331.

[18] E. Eustache, C. Douard, A. Demortiere, V. De Andrade, M. Brachet, J. Le Bideau, T. Brousse, C. Lethien, Adv. Mater. Technol. 2017, 2, 1700126.

[19] L. Wen, R. Xu, Y. Mi, Y. Lei, Nat Nanotechnol 2017, 12, 244.

[20] M. Toupin, T. Brousse, D. Belanger, Chem Mater 2002, 14, 3946.

[21] A. A. Audi, P. M. A. Sherwood, Surf and Interface Anal. 2002, 33, 274.

[22] T. Brousse, M. Toupin, R. Dugas, L. Athouel, O. Crosnier, D. Belanger, J. Electrochem. Soc 2006, 153, A2171.

[23] X. H. Wang, M. Salari, D. E. Jiang, J. C. Varela, B. Anasori, D. J. Wesolowski, S. Dai, M. W. Grinstaff, Y. Gogotsi, Nat Rev Mater 2020, 5, 787.

[24] V. Augustyn, P. Simon, B. Dunn, Energ Environ Sci 2014, 7, 1597.

[25] N. A. Kyerematen, T. Brousse, D. Pech, Nat Nanotechnol 2017, 12, 7.

[26] P. Huang, C. Lethien, S. Pinaud, K. Brousse, R. Laloo, V. Turq, M. Respaud, A. Demortiere, B. Daffos, P. L. Taberna, B. Chaudret, Y. Gogotsi, P. Simon, Science 2016, 351, 691.

[27] F. Bu, W. W. Zhou, Y. H. Xu, Y. Du, C. Guan, W. Huang, Npj Flexible Electronics 2020, 4, 31.

[28] S. Ardizzone, G. Fregonara, S. Trasatti, Electrochim Acta 1990, 35, 263.

[29] M. F. El-Kady, M. Ihns, M. Li, J. Y. Hwang, M. F. Mousavi, L. Chaney, A. T. Lech, R. B. Kaner, Proc Natl Acad Sci U S A 2015, 112, 4233.

[30] E. Eustache, C. Douard, R. Retoux, C. Lethien, T. Brousse, Adv. Energy Mater. 2015, 5, 1500680.

[31] H. Hu, Z. Pei, H. Fan, C. Ye, Small 2016, 12, 3059.

[32] Y. Wang, L. Sun, D. Xiao, H. Du, Z. Yang, X. Wang, L. Tu, C. Zhao, F. Hu, B. Lu, ACS Appl Mater Interfaces 2020, 12, 43864.

[33] B. Bounor, B. Asbani, C. Douard, F. Favier, T. Brousse, C. Lethien, Energy Storage Mater 2021, 38, 520.

[34] C. M. Julien, A. Mauger, Nanomaterials 2017, 7, 396.

[35] L. Liu, H. P. Zhao, Y. Lei, Infomat 2019, 1, 74.

[36] D. Pech, M. Brunet, T. M. Dinh, K. Armstrong, J. Gaudet, D. Guay, J Power Sources 2013, 230, 230.

[37] C. Gao, J. Huang, Y. Xiao, G. Zhang, C. Dai, Z. Li, Y. Zhao, L. Jiang, L. Qu, Nat Commun 2021, 12, 2647.

[38] D. Rochefort, A. L. Pont, Electrochem Commun 2006, 8, 1539.

[39] J. S. Seenath, D. Pech, D. Rochefort, J Power Sources 2022, 548, 232040.

[40] J. Le Bideau, L. Viau, A. Vioux, Chem Soc Rev 2011, 40, 907.

[41] T. Guillemin, C. Douard, K. Robert, B. Asbani, C. Lethien, T. Brousse, J. Le Bideau, Energy Storage Mater 2022, 50, 606.

[42] S. Lindberg, S. Jeschke, P. Jankowski, M. Abdelhamid, T. Brousse, J. Le Bideau, P. Johansson, A. Matic, J Power Sources 2020, 460, 228111.

[43] I. A. Shkrob, T. W. Marin, Y. Zhu, D. P. Abraham, J Phys Chem C 2014, 118, 19661.

[44] M. Kerner, N. Plylahan, J. Scheers, P. Johansson, Phys Chem Chem Phys 2015, 17, 19569.

[45] M. K. Song, S. Cheng, H. Chen, W. Qin, K. W. Nam, S. Xu, X. Q. Yang, A. Bongiorno, J. Lee, J. Bai, T. A. Tyson, J. Cho, M. Liu, Nano Lett 2012, 12, 3483.

[46] S. K. Ghosh, ACS Omega 2020, 5, 25493.

General Conclusion

In this thesis, we have successfully developed novel ionic liquid electrolytes suitable for micro-supercapacitors based on metal-oxide electrodes. Both protic and aprotic ionic liquid electrolytes are designed rationally based on the electrode material properties. The structure property relationship of the materials, including the electrolytes, is meticulously studied prior to performing electrochemical characterisation.

In the first part, we have successfully demonstrated the use of various protic ionic liquids as novel electrolytes for micro-supercapacitors employing electrodeposited RuO_2 electrodes. We selected PIL cations and anions rationally based on their physicochemical properties such as viscosity, conductivity, etc. The surface-controlled proton-coupled electron transfer reaction is realized through the transfer of protons (H^+) from the base cation of PIL with extended operational cell voltage. When PIL is doped with proton conducting SiWa, the concentration of free H^+ ions increase, improving rate performance and pseudocapacitive charge storage. We achieved state-of-the-art MSC charge storage and energy density performance while using porous current collector substrates, which allowed us to increase active material loading. The same level of performance could be translated to ionogel-based all-solid-state MSCs clearly revealing the potential integration of PIL-based RuO_2 MSC in real world on-chip applications with long-term cycling capabilities.

In the following part, we have developed aprotic ionic liquid-based electrolytes for MSCs using $RuO_xN_yS_z$ and MnO_2 electrodes. Conformally deposited of $RuO_xN_yS_z$ on 3D porous current collectors with an extremely high surface area displayed exceptional capacitance values with outstanding stability. Solid-state and ionic liquid-based MSCs using $RuO_xN_yS_z$ electrodes showed enhanced electrochemical performance, including a high energy and power densities and lifetime. Furthermore, we demonstrated the possibility of realizing micro-supercapacitors based on

pseudocapacitive MnO_2. We screened various Na salt containing ionic liquid-based media for MnO_2-based electrodes and demonstrated the micro supercapacitor with superior energy density performance by offering extended operational potential window.

Through this project, we have concluded that ionic liquids are superior to traditional aqueous electrolytes in terms of broadening the electrochemical stability window while enabling surface pseudocapacitive charge storage in metal oxide-based micro-supercapacitor electrodes. Ionic liquid electrolytes can overcome the drawbacks of conventional electrolytes thanks to their improved ion confinement. This is certainly advantageous for their application in on-chip IoT applications, where achieving the desired energy density without significantly compromising power delivery performance is a major challenge, and we know that solid-state ionogel electrolytes will overcome leakage and safety issues, allowing their feasible integration via microfabrication. Besides, the pseudocapacitive electrodes can also be easily made using a basic electrodeposition technique, making them perfect for incorporation into currently used microfabrication processes. We believe that these micro-supercapacitor devices could provide excellent energy/power density micro-energy solutions for creative microsystems seeking energy autonomy in the Internet of Things age.

Perspectives

Through this work, we have developed high-performance MSC devices using pseudocapacitive materials and ionic liquid-based safe electrolytes having better encapsulation (ion confinement) and higher energy storage performance. Certainly, advanced device microfabrication techniques govern the complexity and scalability of on-chip MSCs. Amongst the thin/thick film metal-oxide-based microelectrodes, ionic liquids using 3D architecture endow on-chip MSCs with high energy density, large power density, and long lifespan simultaneously. Although we made great strides towards achieving a high-energy storage performance, there remain several unresolved challenges that need to be tackled as well as plenty of room for future persuasion. It is believed that research on high-performance MSCs aids in the advancement of modern electronics, and we have provided some key future directions below:

- In terms of electrode materials, there's opportunities to develop cost effective materials for MSCs with structural engineering strategies (heteroatom doping, pore creation, phase transformation, interface/interlayer engineering, etc.). This allows for tailoring of intrinsic/extrinsic properties such as electrical conductivity, surface area, phase structure, crystallinity, chemical component, and redox-active sites, and helps to attain high electrochemical performance of on-chip MSCs.

- The physicochemical properties of electrolytes play a major role in determining the electrochemical charge storage performance. Although a wide electrochemical stability window is achieved with our MSCs, other key aspects such as temperature range operation, safety, and cost must be considered in order to fully utilize their potential in future applications. When it comes to PILs, it's imperative to further investigate the properties such as ionicity and/or super-ionicity to help in the design of advanced PILs exhibiting high conductivity and "easily available" proton(s) to be efficiently utilized in electrochemical energy storage allowing for highly reversible and fast

energy storage. In addition, understanding the interplay between PILs and water appears as one of the most intriguing direction in terms of stability window expansion. The investigation on the possibility to control and tune the mobility of the proton in PILs may potentially help in realizing novel PILs with greater electrochemical stability than aqueous electrolytes. The solid-state gel-based electrolytes are more favourable to the applications in portable and flexible modern microelectronics, but their high viscosity is a shortcoming which restricts the ion transport kinetics. Therefore, more efforts should be devoted to better understanding of the IL-polymer interactions and rationally developing ionogel-electrolytes capable of sustaining high rate handling. Furthermore, the addition of electrolyte functional additives may aid in the formation of a stable solid-electrolyte interface and increase wettability and cycling stability.

- For 3D micro electrodes, a rational current collector structuring with openly accessible pores and conformal deposition of active material will ameliorate the issues of electrolyte ion accessibility and helps in better active material utilisation. The sufficiently porous structure can accommodate any volume change during charge/discharge process, extending the cycling life of 3D MSCs. It should be noted that if there are any empty voids in a specific footprint region of porous electrodes, it will affect the packing density and electrode mass loading. Hence, using cutting-edge theoretical and experimental characterization tools, it is necessary to completely investigate how pore size, pore distribution, and pore wall thickness affect the behavior of ion transport and charge storage in constrained 3D porous microelectrodes. By combining in-situ analysis techniques with operando spectroscopic characterizations, real time visualization of electrochemical processes and understanding the evolution of morphology, structure, and component during the charge/discharge process will be possible. This, combined with theoretical modeling studies, will undoubtedly yield novel insights into the underlying charge storage mechanisms.

In summary, advanced microfabrication technologies, electrode architecture design, innovative active material and electrolyte development would be necessary to realize 3D MSCs with superior energy density, high power density, as well as a long cycling lifespan. Besides, finding cost-effective solutions to realise this technology with better device encapsulation will aid in the scaling up of on-chip MSC production and cater to the advancement of IoT technology.

RESUMÉ DE THÈSE

Dévelopement d'électrolytes à base de liquides ioniques dédiés aux micro-supercondensateurs à base d'oxydes métalliques

Jensheer Shamsudeen Seenath

Co-directeurs de thèse :

David PECH (Université Paul Sabatier)

et Dominic Rochefort (Université de Montréal)

Avec le développement des systèmes électroniques embarqués se pose la question de la miniaturisation du stockage réversible de l'énergie. De nos jours, cette fonction est principalement assurée par des micro-batteries. Ces composants possèdent cependant une faible puissance disponible, une durée de vie limitée et un domaine de fonctionnement en température restreint. Les "micro-supercondensateurs" sur puce permettraient de s'affranchir de ces limitations, mais ils ne sont aujourd'hui qu'au stade de la recherche universitaire avec des densités d'énergie bien inférieures à celles des micro-batteries. L'énergie et la puissance stockées dans un supercondensateur sont proportionnelles au carré de la fenêtre de potentiel, qui dépend elle-même de la stabilité électrochimique de l'électrolyte utilisé. L'électrolyte joue ainsi un rôle prépondérant sur les propriétés des supercondensateurs (tension, gamme de température, courant de fuite, durée de vie…).

Cette thèse vise à développer des liquides ioniques protiques et aprotiques dédiés aux micro-supercondensateurs pseudocapacitifs à base d'oxydes métalliques (RuO_2, MnO_2). Les électrolytes à base de liquides ioniques présentent des propriétés intéressantes, notamment une faible pression de vapeur saturante, une stabilité aux hautes températures, ainsi qu'une large fenêtre de potentiel. Ils contribuent ainsi à améliorer la densité d'énergie surfacique, principal problème rencontré par les micro-supercondensateurs actuels. Les liquides ioniques étudiés ont été conçus sur la base de leurs structures et de leurs propriétés physico-chimiques. Des caractérisations électrochimiques ont été réalisées avec des micro-supercondensateurs à base d'oxyde de ruthénium et d'oxyde de manganèse. De très bonnes performances ont été obtenus en utilisant des collecteurs de courant poreux à grande surface spécifique. Les électrolytes liquides constituant cependant un verrou technologique à la réalisation de micro-supercondensateurs fonctionnels compatible avec les procédés de microfabrication, des ionogels composés d'une matrice solide dans laquelle a été confinée le liquide ionique ont également été réalisés.

Chapitre 1 : Introduction et Contexte

Le premier chapitre commence par une brève introduction sur l'historique du stockage de l'énergie électrique, des supercondensateurs et de leurs principes fondamentaux. Les micro-supercondensateurs et leur état de l'art sont ensuite introduits dans le contexte de l'Internet des Objets (IoT). Les matériaux d'électrodes et les différentes catégories d'électrolytes sont détaillés ainsi que les outils de caractérisation physico-chimiques et électrochimiques utilisés pour réaliser ce projet. Les objectifs clefs de cette thèse sont finalement présentés.

Contexte

L'Internet des Objets (IoT) est une technologie émergente qui connecte des objets du quotidien à l'Internet, permettant ainsi une communication entre eux et avec les utilisateurs. Cette technologie est en train de transformer notre manière d'interagir avec les objets, créant un environnement où les objets sont de plus en plus autonomes et peuvent communiquer entre eux. Cependant, pour que l'IoT soit viable, il est nécessaire de disposer de sources d'énergie suffisantes pour alimenter ces milliards d'objets connectés.

Les micro-supercondensateurs sont une alternative prometteuse aux batteries, car ils offrent une densité de puissance plus élevée, une durée de vie plus longue, une meilleure stabilité thermique et une capacité de charge et de décharge plus rapide. En outre, les micro-supercondensateurs sont plus respectueux de l'environnement que les batteries, car ils peuvent être fabriqués à partir de matériaux durables et recyclables.

Il existe différents types de supercondensateurs, les plus couramment utilisés étant les supercondensateurs à double couche électrique (EDLC) et les supercondensateurs pseudocapacitifs. Les supercondensateurs pseudocapacitifs stockent les charges électriques par réactions réversibles d'oxydo-réduction, contrairement aux supercondensateurs à double couche

électrique qui ne stockent l'énergie qu'à travers l'adsorption de charges électriques sur la surface de l'électrode. Les matériaux pseudocapacitifs, tels que les oxydes métalliques et les polymères conducteurs, ont une densité d'énergie plus élevée que les matériaux à double couche électrique et peuvent être utilisés pour augmenter la capacité de stockage d'énergie des supercondensateurs. Cependant, ils ont également des limitations en termes de stabilité thermique et tension en raison de l'électrolyte acqueux utilisé.

Les micro-supercondensateurs ont connu des avancées significatives ces dernières années, en particulier avec l'avènement des micro-supercondensateurs 3D. Ces dispositifs sont basés sur des structures tridimensionnelles sur lesquelles est déposé le matériau actif. Les micro-supercondensateurs 3D présentent des avantages considérables par rapport aux dispositifs planaires conventionnels, notamment une densité d'énergie plus élevée et une capacité de charge et de décharge plus rapide. Cependant, pour atteindre des performances optimales, il est crucial de prendre en compte les performances surfaciques et non gravimétriques, c'est-à-dire la capacité de stockage d'énergie par unité de surface plutôt que par unité de masse. De plus, l'optimisation des performances des micro-supercondensateurs 3D nécessite une compréhension approfondie des interactions électrode-électrolyte et des mécanismes de transport ionique au niveau des interfaces électrolyte-électrode.

Les électrolytes

Les électrolytes sont un composant crucial des supercondensateurs car ils permettent le transfert de charges électriques entre les électrodes. Il existe trois types d'électrolytes utilisés dans les supercondensateurs: aqueux, organique et liquide ionique.

Les électrolytes aqueux sont les plus couramment utilisés dans les supercondensateurs en raison de leur faible coût et de leur haute conductivité électrique. Ils sont également relativement sûrs et faciles à manipuler. Cependant, les électrolytes aqueux ont une faible tension de fonctionnement

et une faible stabilité à haute température, ce qui limite leur application. Les électrolytes organiques, tels que les solvants à base d'acétonitrile ou de carbonate de propylène, ont une tension de fonctionnement plus élevée que les électrolytes aqueux et sont donc souvent utilisés dans les supercondensateurs à haute énergie. Cependant, les électrolytes organiques peuvent être plus inflammables et moins stables que les électrolytes aqueux.

Les liquides ioniques (IL pour *Ionic Liquid*) sont les plus récents types d'électrolytes utilisés dans les supercondensateurs. Ils ont une grande stabilité thermique et une grande capacité de stockage d'énergie. Les liquides ioniques peuvent également être utilisés à des températures extrêmes, ce qui les rend utiles pour les applications militaires et spatiales. Un liquide ionique est un sel fondu à basse température, qui se présente sous forme liquide à température ambiante. Contrairement aux électrolytes classiques, les liquides ioniques sont constitués uniquement d'ions, ce qui leur confère des propriétés uniques telles qu'une conductivité ionique élevée, une grande stabilité thermique et une faible volatilité. Ces caractéristiques en font des matériaux prometteurs pour de nombreuses applications, notamment dans les domaines du stockage d’énergie.

Bien que les électrolytes liquides présentent une conductivité ionique élevée, leur utilisation dans l'étape d’encapsulation des micro-supercondensateurs peut entraîner des problèmes de fuite et de stabilité. De plus, la manipulation et le stockage des électrolytes liquides peuvent être complexes. En réponse à ces problèmes, de plus en plus de recherche sont consacrées à l'utilisation d'électrolytes solides pour les micro-supercondensateurs, car ces derniers présentent des avantages en termes de stabilité, de sécurité et de durée de vie.

Les liquides ioniques

Les liquides ioniques peuvent être classés en 3 types : aprotiques, protiques et zwitterioniques. Les liquides ioniques aprotiques sont souvent utilisés dans les batteries lithium-ion et les supercondensateurs à double-couche tandis que les liquides ioniques protiques plutôt pour des

applications piles à combustible. Les liquides ioniques protiques (PIL pour *Protic Ionic Liquid*) forment un sous-ensemble des LI. Formés à partir d'un mélange d'un acide et une base de Brønsted, ils possédent un proton labile pouvant intervenir dans le stockage de charge pseudocapacitif. Comparés aux liquides ioniques aprotiques, ils sont moins chers, plus faciles à synthétiser et possèdent généralement une plus faible viscosité. Les IL zwitterioniques avec ajout de sels sont adaptés aux dispositifs électrochimiques ainsi qu'aux systèmes de membranes. Il existe un compromis entre conductivité ionique, point de fusion, viscosité et fenêtre de potentiel des liquides ioniques. Contrairement aux électrolytes organiques, les micro-dispositifs utilisant des électrolytes à base de liquides ioniques pourraient offrir des tensions de cellule supérieures à 3 V sans problème de sécurité, même à hautes températures. Cependant, leur viscosité élevée – en particulier à basse température - et leur faible conductivité ionique peuvent augmenter de manière importante la résistance série équivalent (ESR) et la puissance du micro-dispositif, même si cette dernière peut être compensée par une densité d'énergie plus élevée. Pour pallier ces insuffisances, des efforts ont été déployés pour judicieusement sélectionner la composition des liquides ioniques et comprendre la dynamique des ions à l'interface électrode / électrolyte. La combinaison de différents cations et anions permet une grande souplesse dans la conception des matériaux et la sélection de leurs propriétés selon l'application souhaitée. Dans les supercondensateurs, les cations couramment utilisés sont l'imidazolium, le pyrrolidinium, l'ammonium, le sulfonium et le phosphonium, et les anions employés sont le tétrafluoroborate (BF_4^-), l'hexafluorophosphate (PF_6^-), le bis(trifluorométhane sulfonyl)imide (TFSI ou NTf_2), le bis(fluoro sulfonyl)imide (FSI), le dicyanamide (DCA), etc.

Cette thèse vise à développer de nouveaux électrolytes à base de liquides ioniques, à la fois protiques et aprotiques, adaptés aux micro-supercondensateurs pseudocapacitifs à base d'oxydes métalliques. Nous étudions plus particulièrement dans le chapitre 2 différents liquides ioniques

protiques dédiés aux micro-supercondensateurs RuO_2. Le chapitre 3 est plus particulièrement consacré aux liquides ioniques protiques à base de pyrrolidinium possédant différents groupements anioniques et substitutions alkyles de longueur variable pour des micro-supercondensateurs RuO_2 plan et poreux. Sur la base de ces électrolytes, des ionogels sont également développés. Enfin, dans le chapitre 4, des liquides ioniques dopés avec des additifs conducteurs de protons et des liquides ioniques contenant des sels de sodium (Na) sont respectivement envisagés pour des électrodes alternatives telles que le $RuO_xN_yS_z$ et le MnO_2.

Chapitre 2 : Liquides ioniques protiques adaptés aux micro-supercondensateurs RuO_2

Réalisation de micro-dispostifs

Des micro-supercondensateurs RuO_2 plans en configuration interdigitée ont préalablement été réalisés pour étudier les PIL sélectionnés. Ces micro-supercondensateurs ont été réalisés par photolithograhie standard sur des plaquettes de Si et le dépôt d'oxyde de ruthénium, détaillé dans le manuscrit de thèse, par voie électrochimique. Le matériau actif a été caractérisé par microscopie électronique à balayage (MEB, Figure 1) et spectrocopie photoélectronique X (XPS pour *X-ray Photoelectron Spectrocopy*).

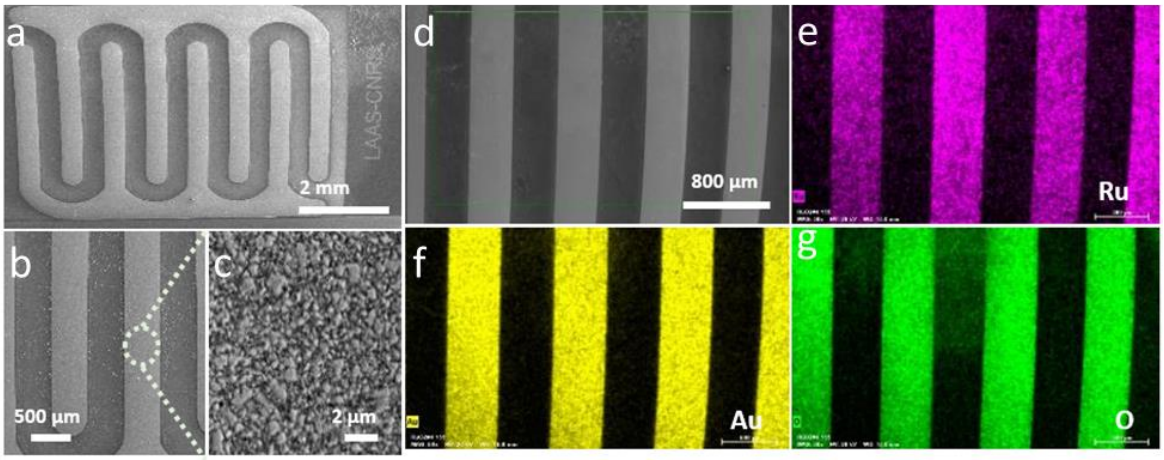

Figure 1. Images MEB à différents grossissements (a-d) et cartographie élémentaire du RuO_2 déposé sur un collecteur de courant plat interdigité en Au (e-g).

Sélection des PIL

La structure des liquides ioniques protiques étudiées est présentée Figure 2. La séléction a été effectuée sur la base de leurs propriétés physico-chimiques, à savoir une forte ionicité (par le choix d'un ΔpKa élevée entre le cation et l'anion), une bonne conductivité ionique, une faible viscosité et une large fenêtre de potentiel électrochimique. Alors que les PIL à base de pyrrolidinium ou d'alkyl ammonium peuvent offrir une large fenêtre de stabilité, les PIL composés d'un cation à base de pyridine et d'un anion d'acide trifluoroacétique permet une ionicité élevée (forte différence de pKa).

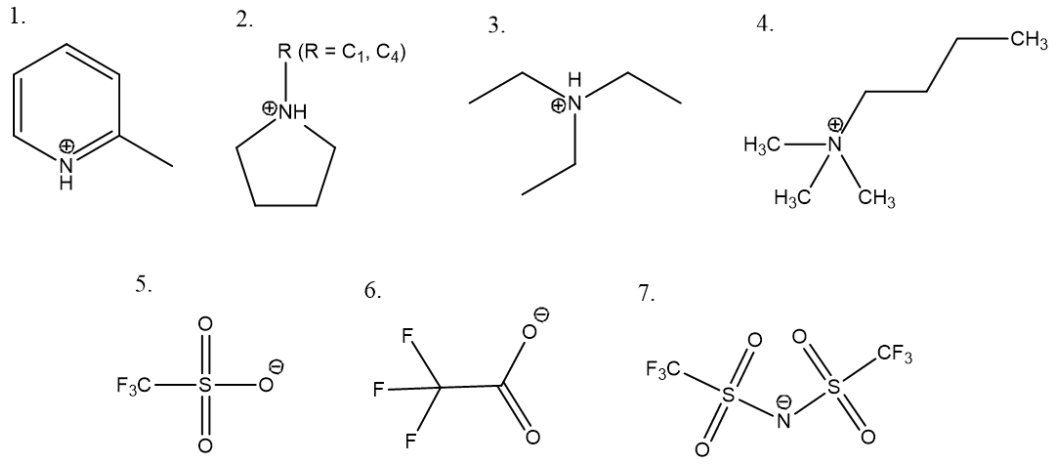

Figure 2. Structures des cations et anions des liquides ioniques explorés pour les micro-supercondensateurs RuO_2 (*1. 2-MePy = 2-méthyl pyridinium, 2. Pyr_{1H} = 1-méthyl pyrrolidinium, Pyr_{4H} = 1-butyl pyrrolidinium, 3. TEAH =*

triéthylammonium, 4. BTMA = butyl-triméthyl ammonium, 5. Tf = trifluorométhanesulfonate, 6. TFA = trifluoroacétate, 7. TFSI = bis(trifluorométhane sulfonyl)imide).

Étude électrochimique

Une comparaison des différents PIL a tout d'abord été effectué par voltampérométrie cyclique (CV pour *Cylic Voltammetry*) avec l'électrolyte aqueux 0,5 M H_2SO_4 couramment utilisé avec l'oxyde de ruthénium RuO_2 sur des micro-supercondensateurs entre 0 et 1 V (Figure 3).

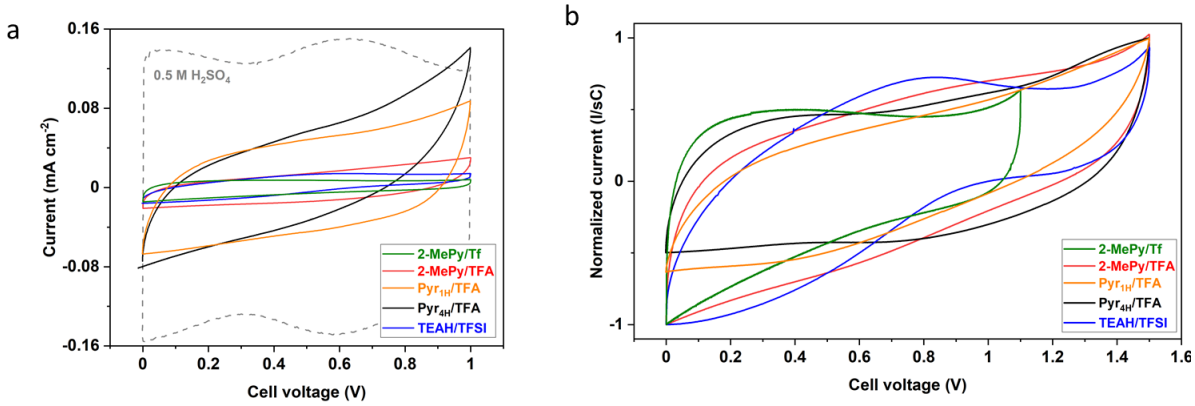

Figure 3. *a. Courbes de voltampérométrie cyclique de micro-supercondensateurs plans interdigités testés avec différents PIL et comparaison avec 0,5 M H_2SO_4 (vitesse de balayage de 100 mV/s) ; b. CV normalisés de RuO_2 dans des PIL à une vitesse de balayage de 100 mV/s.*

Bien que la densité de courant soit plus élevée avec l'électrolyte acide aqueux en raison d'une cinétique plus rapide et d'une utilisation efficace des sites actifs, sa tension est limitée à environ 1 V en raison de la limite de décomposition thermodynamique de l'eau. Notons que parmis les PIL synthétisées, le 2-MePy/Tf et le Pyr_{1H}/TFA sont restées sous forme solide ou semi-solide, il a donc été nécessaire d'utiliser un solvant organique et un milieu liquide ionique aprotique pour leur dilution, les rendre liquide et pouvoir les caractériser électrochimiquement.

La figure 3b montre les CV normalisés (courant *I* normalisé par la vitesse de balayage *s* et la capacité *C*) des micro-supercondensateurs RuO_2 testées en utilisant des PIL à leur tension cellulaire maximale (1,1 V pour 2-MePy/Tf et 1,5 V pour le reste des PIL : 2-MePy/TFA, Pyr_{1H}/TFA, Pyr_{4H}/TFA, et TEAH/TFSI). Les CV ont montré des formes pseudo-rectangulaires

indiquant un transfert de charge pseudocapacitif entre la PIL et RuO_2 au-delà de la fenêtre de stabilité thermodynamique des électrolytes aqueux conventionnels.

Influence d'un additif protonique sur les performances des micro-supercondensateur RuO_2 à base de PIL

Bien que les PIL puissent échanger des protons à la surface du RuO_2, leur transport est lent et limité. Pour résoudre ce problème, nous avons exploré un dopage des IL avec un conducteur ionique solide de proton H^+, l'acide silicotungstique hydraté (SiWa, $H_4SiW_{12}O_{40}$). Le SiWa appartient à la famille des hétéropolyacides qui sont des sels hydratés possédant une solubilité élevée dans l'eau et dans de nombreux solvants organiques, ainsi qu'une conductivité protonique élevée à température ambiante (par exemple 0,027 S/cm pour le $SiWa.28H_2O$). L'étude du SiWa avec des PIL n'a jamais été réalisée auparavant et il était intéressant d'explorer la compatibilité et le comportement électrochimique par rapport à un liquide ionique aprotique ayant une structure similaire à celle du TEAH/TFSI.

L'étude par voltampérométrie cyclique révèle une nette amélioration du courant pseudocapacitif dans le BTMA/TFSI dopé au SiWa, l'analogue aprotique choisi pour l'étude (Figure 4a), indiquant que le SiWa fournit des protons H^+ librement disponibles pour promouvoir les réactions d'oxydo-réduction de surface avec le RuO_2 qui, auparavant, ne contribuait que par sa double couche.

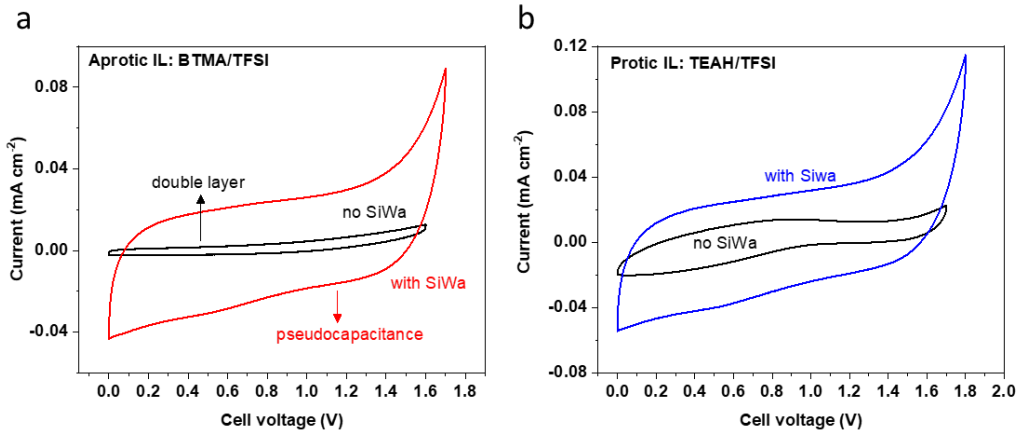

Figure 4: *Influence d'un dopage SiWa (10 % en poids) dans des IL protiques et aprotiques basés sur l'anion TFSI sur le comportement capacitif de micro-supercondensateurs RuO_2. a. CV à 100 mV/s dans un liquide ionique aprotique - le butyl-triméthyl-ammonium bis(trifluorométhylsulfonyl)imide (BTMA/TFSI) - avant et après dopage au SiWa. b. CV en utilisant le TEAH/TFSI avant et après le dopage au SiWa.*

Concernant le IL protique TEAH/TFSI (Figure 4b), le SiWa accélère le transport de charge avec une augmentation des valeurs de courant due à un transport combiné de type Grotthus du SiWa et de type véhiculaire du TEAH/TFSI. Ces résultats démontrent clairement l'importance des additifs conducteurs protoniques dans l'obtention d'une réponse améliorée du courant faradique avec les électrodes RuO_2.

Étude électrochimique du RuO_2 sur substrats poreux

Pour démontrer la viabilité pratique des micro-supercondensateurs, il est impératif de développer des collecteurs de courant à haute rugosité ayant une surface électrochimiquement active élevée tout en conservant l'espace d'encombrement limité disponible. La conception d'une architecture tridimensionnelle (3D) poreuse d'électrodes permet d'augmenter la quantité de matériaux actif par unité de surface tout en améliorant les cinétiques de diffusion des ions et le transport des électrons. Nous avons ici préparé des collecteurs de courant interdigités en or par la technique de structuration dynamique par bullage d'hydrogène (DHBT pour *Dynamic Hydrogen Bubble Template*). La figure 5 montre des électrodes en or d'environ 20 µm d'épaisseur élaboré par DHBT sur lesquelles ont été déposées du RuO_2.

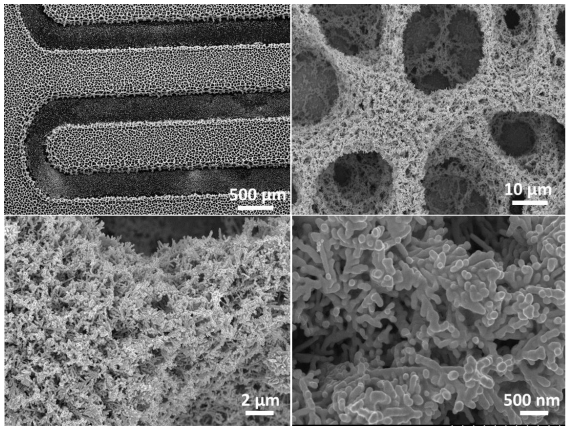

Figure 5: *Image par microscopie électronique à balayage (MEB) à différents grossissements du substrat Au DHBT après dépôt de RuO_2.*

La figure 6 montre les courbes voltampérométriques des électrodes poreuses RuO_2 testées dans les électrolytes (TEAH/TFSI) et (TEAH/TFSI + SiWa). Un gain notable de la densité de courant est observé en utilisant l'électrolyte dopé au SiWa avec l'apparition de pics d'oxydo-réduction, révèlant l'abondance de protons dans l'électrolyte favorisant le processus faradique contrôlé par la surface. Il est important de noter qu'en passant des substrats plats aux substrats en Au à forte rugosité, la tension de la cellule est plus élevée, principalement en raison d'une résistance plus élevée provenant des substrats DHBT avec une épaisseur d'électrode plus importante.

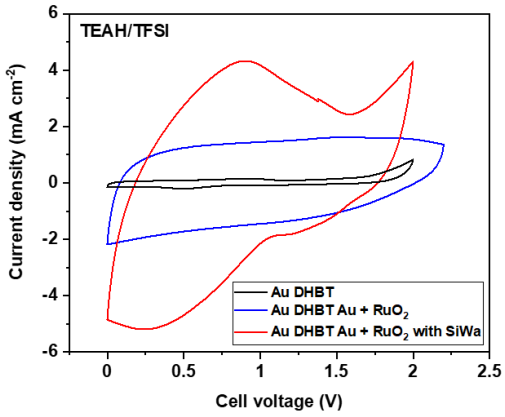

Figure 6: *CV de micro-dispositifs interdigités à 100 mV/s en milieu TEAH/TFSI de l'or poreux, après dépôt de RuO_2, et avec dopage SiWa.*

Micro-supercondensateur 3D à base d'ionogel et comparaison avec l'état de l'art

Pour d'envisager des prototypes de micro-supercondensateurs fonctionnels, il est impératif de développer des électrolytes à l'état solide ou gélifiés qui ne fuient pas et capables de fonctionner dans des conditions opérationnelles réelles. Les électrolytes liquides ne sont pas compatibles avec le processus de micro-fabrication en raison des problèmes d'évaporation et de sécurité. Étant donné que le TEAH/TFSI dopé au SiWa a montré les meilleures performances en tant qu'électrolyte pour les micro-supercondensateurs poreux de RuO_2, nous avons développé un ionogel utilisant le TEAH/TFSI + SiWa en le combinant avec un polymère à base de poly(fluorure de vinylidène) (PVDF). Pour mieux comprendre le changement de l'ESR lors de la transition de l'état liquide à l'état gelifié, nous avons effectué une mesure par spectroscopie d'impédance électrochimique (figure 7). Une valeur ESR plus élevée de 52,5 Ω cm^2 pour le dispositif à l'état solide (plus du double par rapport à l'état liquide) peut être attribuée au mouvement ionique restreint dans l'état solide.

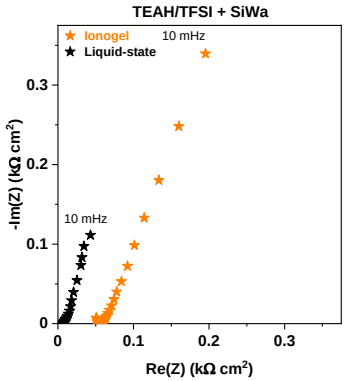

Figure 7: *Spectroscopie d'impédance électrochimique de micro-supercondensateurs poreux à base de RuO_2 utilisant un électrolyte TEAH/TFSI à l'état liquide (noir) et ionogel (orange).*

La comparaison des micro-supercondensateurs poreux RuO_2 testés dans les différents électrolytes est représentée dans un diagramme de Ragone représentant la densité d'énergie en fonction de la densité de puissance (figure 8). La tension de cellule plus élevée de la PIL par rapport à l'électrolyte aqueux 0,5 M H_2SO_4 conduit à une amélioration de la densité énergétique du micro-supercondensateur (31,8 µWh/cm^2 à 0,5 mW/cm^2) comparé à celui testé en milieu 0,5 M H_2SO_4

(7,6 µWh/cm^2 à 0,23 mW/cm^2). Le micro-supercondensateur à l'état solide présente quand à lui une valeur de densité énergétique de 17,26 µWh/cm^2 à 0,56 mW/cm^2, soit légèrement inférieure à celle de l'électrolyte liquide.

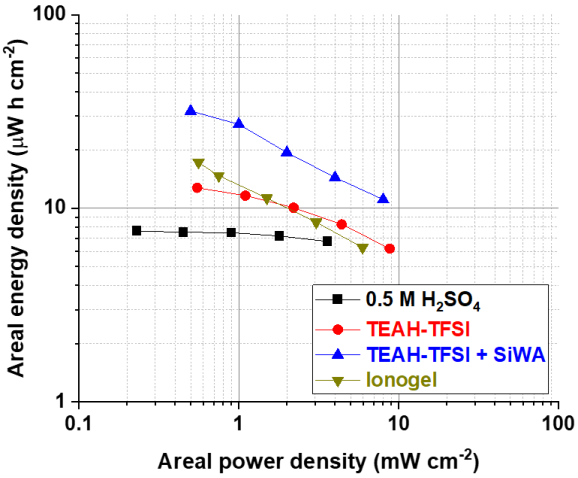

Figure 8: *Diagramme de Ragone de micro-supercondensateurs poreux RuO_2 testées dans différents électrolytes.*

Qu'il soit à l'état liquide ou solide (ionogel), les micro-supercondensateurs à base de PIL TEAH/TFSI dopé au SiWa ont affiché de bonne performance en cyclage à long terme, jusqu'à 5000 cycles. Il convient de noter que les performances (capacité surfacique, densité énergétique et durée de vie) peuvent être considérablement améliorées à l'avenir grâce à un choix rationnel de PIL et à une meilleure compréhension du mécanisme de stockage de charge. Les performances rapportées ici démontrent cependant clairement le potentiel des micro-supercondensateurs à l'état solide à base de RuO_2 pour les futures applications basées sur l'IoT.

Chapitre 3. Micro-supercondensateurs RuO_2 utilisant des PIL à base de pyrrolidinium contenant différents groupes d'anions et de substitutions alkyles

PIL à base de pyrrolidinium

Dans ce chapitre, nous étudions l'utilisation de liquides ioniques protiques (PIL) à base de pyrrolidinium contenant différentes substitutions alkyles et groupements anioniques comme électrolytes pour les micro-supercondensateurs RuO_2 (figure 9) afin de mieux comprendre comment le PIL à base de pyrrolidinium affecte le stockage de charge. Le sel conducteur fondu utilisant un cation à base de pyrrolidinium semble être le plus prometteur en raison de son coût relativement faible et de sa faible toxicité. Il permet d'augmenter la tension de fonctionnement des supercondensateurs et des batteries sans réduire la puissance et la durée de vie du cycle.

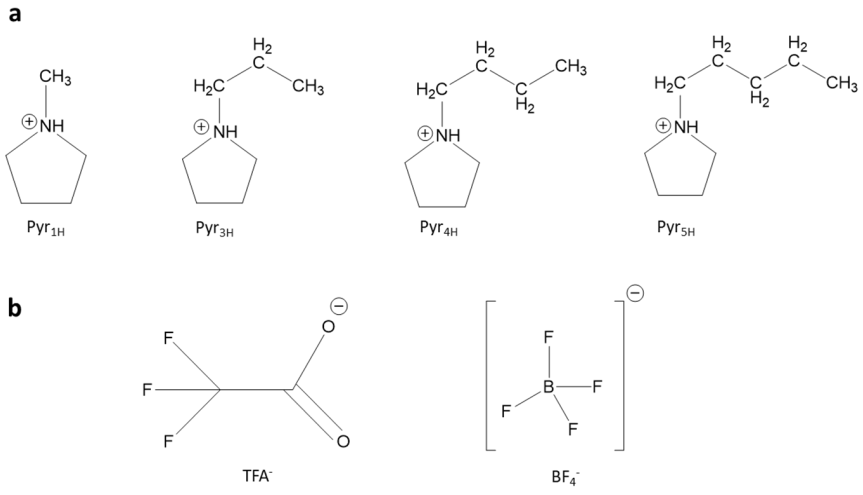

Figure 9. *Structure des cations à base de pyrrolidinium (a) et groupements anioniques correspondants (b) étudiés pour les micro-supercondensateurs RuO_2 (Pyr_{1H} = 1-méthyl pyrrolidinium, Pyr_{3H} = 1-propyl pyrrolidinium, Pyr_{4H} = 1-butyl pyrrolidinium, Pyr_{5H} = 1-pentyl pyrrolidinium, TFA = trifluoroacétate, BF_4 = tétrafluoroborate).*

Notons que lorsque le nombre d'atomes de carbone dans la longueur de la chaîne alkyle est inférieur à 3C avec l'anion TFA (cas du Pyr_{1H}-TFA), le PIL a tendance à se solidifier. Il est donc difficile de l'utiliser comme électrolyte pour tester le micro-supercondensateur. En revanche, dans le cas du Pyr_{1H}-BF_4, le PIL devient extrêmement hydrophile avec une teneur en eau d'environ 8000

ppm même après séchage. En dessous d'une certaine teneur en eau après traitement sous ultravide, le Pyr_{1H}-BF_4 ne reste plus à l'état liquide. Il est donc important de trouver le bon équilibre entre quantité d'eau et PIL utilisé afin d'exploiter leur fonction d'électrolytes pour les supercondensateurs.

Contrairement aux liquides ioniques aprotiques, la présence d'un proton sur le cation de base dans les PIL donne lieu à un réseau de liaisons hydrogène. Cette caractéristique peut être utilisée pour concevoir des PIL hydrophiles où les molécules d'eau peuvent interagir avec le PIL par le biais de ces liaisons hydrogène. Cela permet d'augmenter la conductivité de l'électrolyte en combinant une migration de protons de type Grotthuss avec un transport véhiculaire. La compréhension de l'interaction entre le PIL et l'eau présente donc un intérêt significatif pour le développement d'électrolytes pour les dispositifs de stockage de l'énergie. Dans le contexte des micro-supercondensateurs RuO_2, la conception de PIL hydrophiles est prometteuse car elle accélère le transfert de charge et le stockage de charge pseudocapacitif sans compromettre la densité de puissance.

Pour comprendre les propriétés de transport des PIL à base de pyrrolidinium, des mesures de conductivité et de viscosité ont été effectuées. Les valeurs de conductivité molaire des PIL en fonction de la température ont été représentées sur un graphique d'Arrhenius (figure 10). La nature hygroscopique du Pyr_{1H}-BF_4 se reflète par sa conductivité ionique molaire plus élevée (environ 20 mS/cm à 20 °C) avec une teneur en eau d'environ 8000 ppm. Cette valeur est nettement plus élevée que celle observée dans d'autres PIL, ce qui indique une contribution significative du transport de charge de type Grotthuss observé dans les électrolytes aqueux. Pour les PIL à base de pyrrolidinium avec des anions TFA, le PIL avec la longueur de chaîne alkyle la plus faible (Pyr_{3H}-TFA) possède la conductivité la plus élevée car un groupe de chaîne alkyle plus petit permet une migration plus rapide des ions. L'ionicité élevée de $Pyr_{1H}BF_4$ se reflète également dans le

diagramme de Walden, où il occupe une région située au-dessus de la ligne idéale (telle que décrite par Angell *et al.*), ce qui est inhabituel dans le cas des PIL, où le transport de charges non véhiculaires est prédominant.

Le comportement particulier du Pyr_{1H}-BF_4 pourrait provenir de sa teneur en eau élevée entraînant une perturbation de l'interaction ion-ion, rendant ce PIL dans un état complètement dissocié. Concernant les autres PIL (Pyr_{3H}-TFA, Pyr_{4H}-TFA, et Pyr_{5H}-TFA), ils occupent la région des "bons" liquides ioniques dans le diagramme de Walden avec un léger appariement ionique comme la plupart des PIL rapportés dans la littérature.

Dans l'ensemble, les valeurs de conductivité mesurées par les PIL sélectionnés sont prometteuses et peuvent être considérés comme électrolytes pour les micro-supercondensateurs RuO_2.

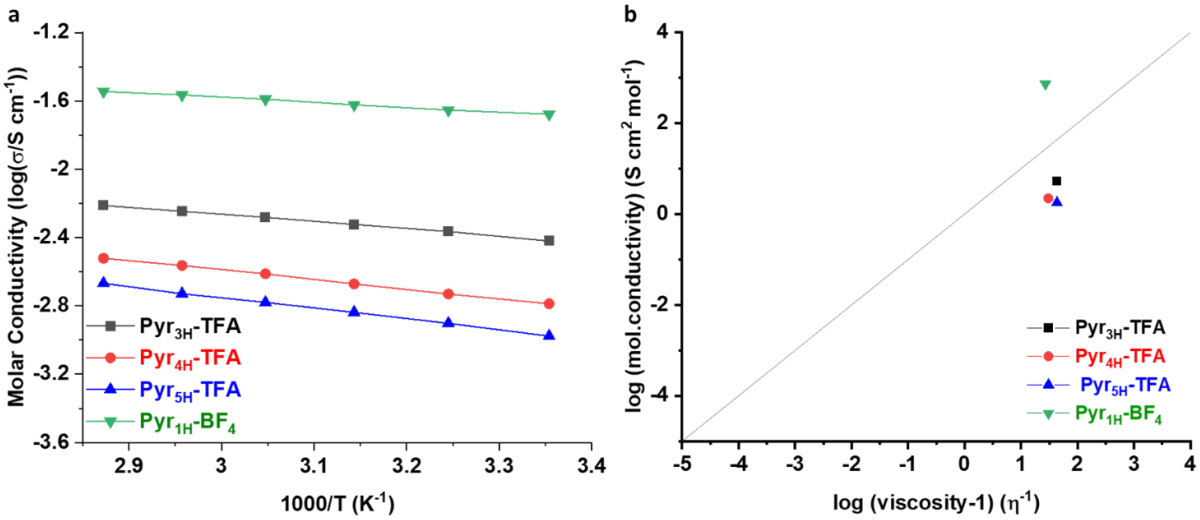

Figure 10. *Caractérisation des électrolytes. a. Diagrammes d'Arrhenius pour des PIL à base de pyrrolidinium avec des mesures effectuées à un intervalle de 10°C entre 25 et 75°C ; b. Diagramme de Walden comparant les valeurs d'ionicité et de conductivité équivalente des PIL à base de pyrrolidinium.*

Étude électrochimique de micro-supercondensateurs RuO_2 à base de PIL de pyrrolidinium

Nous avons testé les IL sur des micro-supercondensateurs RuO_2 plans et des micro-supercondensateurs RuO_2 poreux synthétisé par DHBT.

Une légère distorsion et un changement dans la forme des courbes voltampérométriques sont observés en passant des substrats plats aux substrats poreux, car la dynamique des ions et le comportement de transfert de charge deviennent complexes avec plus de matériaux actifs présents dans ces substrats à forte rugosité. La même tendance se reflète dans les mesures par spectroscopie d'impédance électrochimique (figure 11). Le Pyr_{1H}-BF_4 montre la valeur d'ESR la plus basse, suivi par le Pyr_{3H}-TFA. La conductivité ionique plus faible du Pyr_{5H}-TFA empêche aux ions d'accéder aux sites actifs plus profonds sur les pores densément connectés, ce qui entraîne une résistance plus élevée du dispositif.

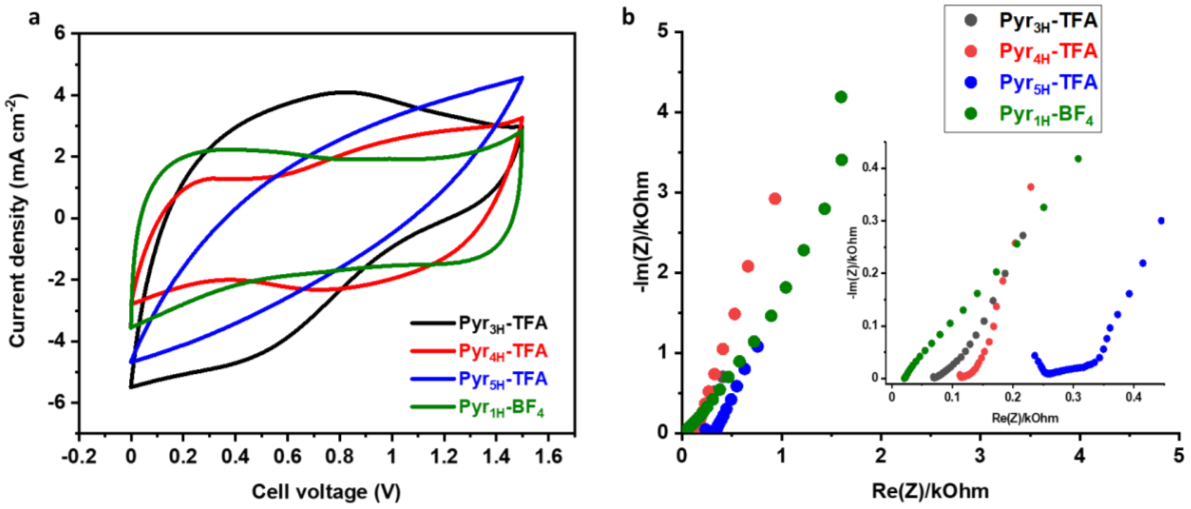

Figure 11. *Caractérisation électrochimique de micro-supercondensateurs RuO_2 sur des substrats interdigités DHBT en Au testés dans différents PIL à base de pyrrolidinium. a. Comparaison des CV à 100 mV/s. b. Diagramme de Nyquist obtenue de 100 kHz à 10 mHz.*

Parmi toutes les PIL à base de pyrrolidinium étudiés pour les micro-supercondensateurs RuO_2, le Pyr_{3H}-TFA et le Pyr_{1H}-BF_4 ont donné les résultats les plus prometteurs. Ces PIL ont donc été sélectionnés pour une étude plus poussée avec des micro-supercondensateurs RuO_2 poreux et développer des électrolytes ionogels afin de construire des micro-supercondensateurs de RuO_2 poreux tout solide.

Le tracé des courbes de CV des micro-supercondensateurs poreux de RuO_2 testées avec le Pyr_{3H}-TFA à différentes vitesses de balayage sont indiquées figure 12a. Des comportements pseudocapacitifs sont observés avec une réversibilité du processus d'oxydo-réduction. Le stockage des charges faradiques est également bien représenté dans les tracés de charge/décharge avec des courbes non linéaires à des densités de courant variables (figure 12b). Le micro-supercondensateur RuO_2 poreux utilisant le Pyr_{3H}-TFA possède une capacité surfacique élevée de 106 mF/cm^2 à 5 mV/s.

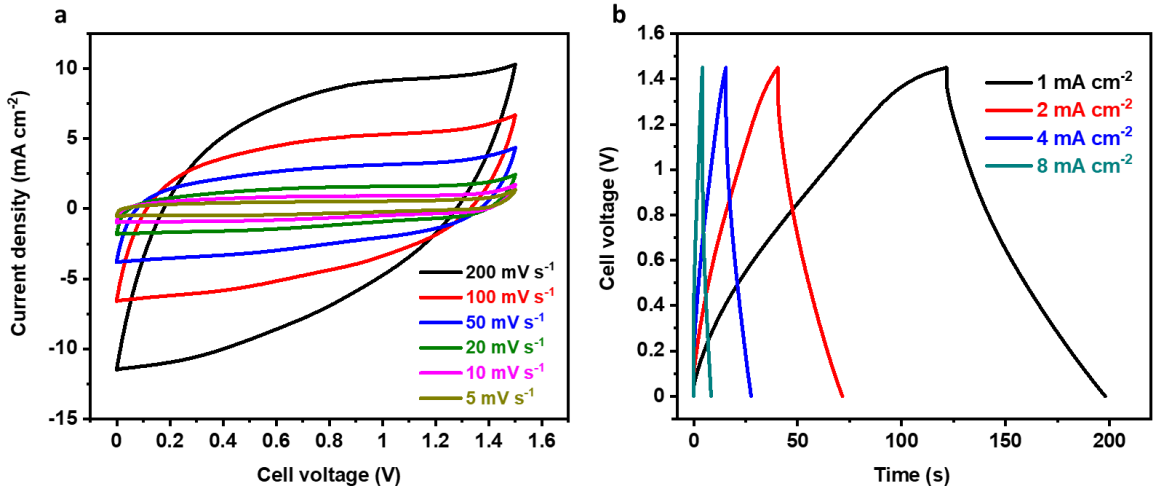

Figure 12. *Micro-supercondensateurs RuO_2 poreux testés avec le Pyr_{3H}-TFA. a. CV à différentes vitesses de balayage ; b. Courbes galvanostatiques à différentes densités de courant.*

Les CV du micro-supercondensateur RuO_2 poreux utilisant le Pyr_{1H}-BF_4 ont également montré un comportement pseudocapacitif avec une réversibilité des réactions d'oxydo-réduction à différentes vitesses de balayage (figure 13a). Par ailleurs, un comportement capacitif idéal est observé dans le diagramme de Nyquist par spectroscopie d'impédance électrochimique avec une faible ESR de 2

Ω cm^2 et une ligne presque verticale à basse fréquence parallèle à l'axe imaginaire du spectre d'impédance (figure 13b). Cette ESR extrêmement faible lors de l'utilisation de Pyr_{1H}-BF_4 pourrait être due à la teneur élevée en eau qui est uniformément distribuée dans le PIL, facilitant un transport de protons de type Grotthuss.

La figure 13c montre un diagramme de Ragone comparant nos micro-supercondensateurs RuO_2 testés avec les différents liquides ioniques électrolytes. La combinaison d'une tension de cellule et d'une capacité surfacique élevées du micro-supercondensateur RuO_2 poreux utilisant le Pyr_{3H}-TFA permet d'obtenir une énergie surfacique de 15,5 µWh/cm^2 à 0,73 mW/cm^2. Cette densité énergétique conserve une valeur de 5,9 µWh/cm^2 à une densité de puissance plus élevée de 7,2 mW/cm^2. Le micro-supercondensateur à l'état solide correspondant utilisant un ionogel dérivé du Pyr_{3H}-TFA affiche une énergie surfacique décente de 8,4 µWh/cm^2 à 0,19 mW/cm^2.

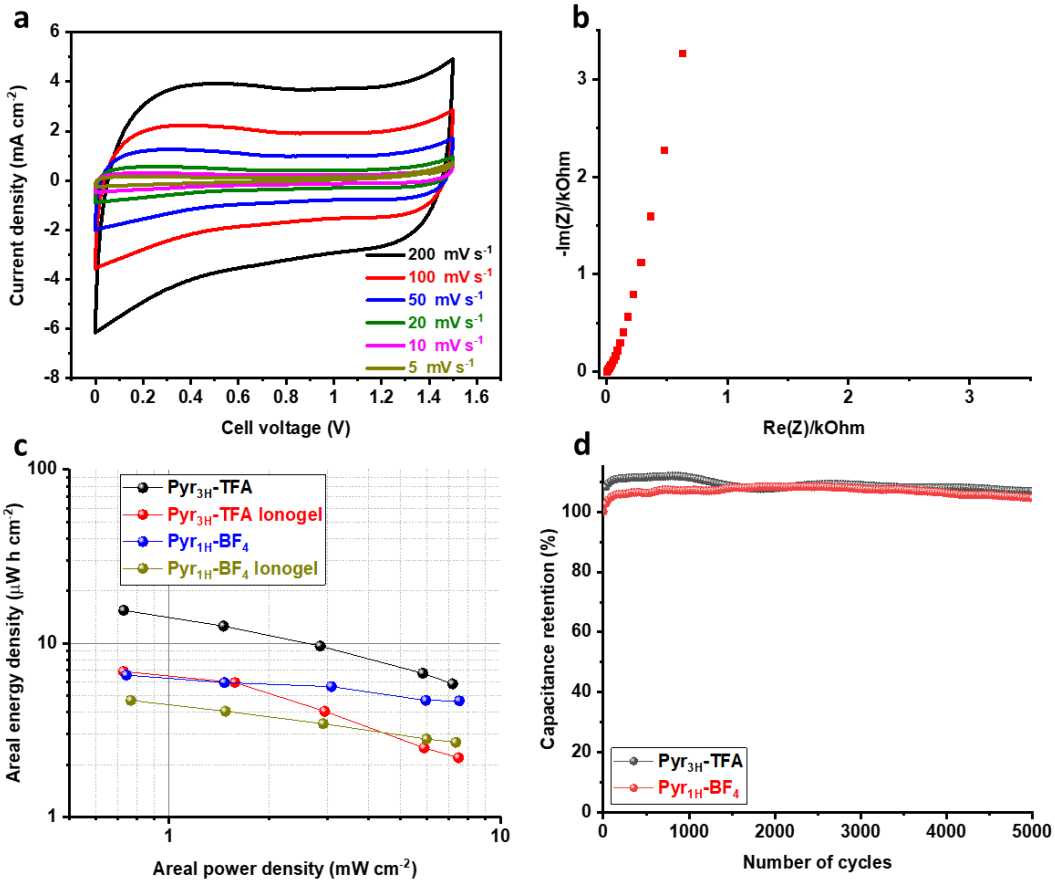

Figure 13. *a. CV à différentes vitesses de balayage et b. Diagramme de Nyquist d'un micro-supercondenteur RuO_2 poreux testé dans le Pyr_{1H}-BF_4 ; c. Diagramme de Ragone de micro-supercondensateur RuO_2 poreux testés dans les électrolytes à base de Pyr_{3H}-TFA et de Pyr_{1H}-BF_4 et d. Stabilité en cyclage.*

Concernant les micro-supercondensateurs RuO_2 testés avec le Pyr_{1H}-BF_4, il présente une densité d'énergie raisonnable de 6,5 µWh/cm^2 à 0,74 mW/cm^2 à l'état liquide et une énergie de 4,7 µWh/cm^2 à 0,76 mW/cm^2. Les densités de puissance obtenues pour ces micro-supercondensateurs sont comparables à celles obtenues avec des électrolytes aqueux.

Les performances en cyclage de ces micro-dispositifs de stockage d'énergie utilisant le Pyr_{3H}-TFA et le Pyr_{1H}-BF_4 démontrent une excellente stabilité à long terme (figure 13d) indiquant un emploi pratique de ces micro-supercondensateurs. Bien qu'il soit possible d'améliorer encore ces performances, notamment par une meilleure conception du collecteur de courant et un dépôt plus conforme du RuO_2 pour une meilleure accessibilité des charges avec les PIL, les excellentes caractéristiques électrochimiques utilisant ces PIL à base de pyrrolidinium sont prometteuses pour l'utilisation de micro-supercondensateurs à base de RuO_2 dans les futures technologies basées sur l'IoT.

Chapitre 4 : Électrolytes à base de liquides ioniques pour les micro-supercondensateurs à base de $RuO_xN_yS_z$ et de MnO_2 poreux

Dans ce chapitre, nous avons étudié des liquides ioniques adaptés à d'autres matériaux pseudocapacitifs de micro-supercondensateurs, à base d'oxydes métalliques alternatifs, développés au sein de notre équipe. Le $RuO_xN_yS_z$ et le MnO_2 ont été choisis comme matériaux actifs car ils présentent de très bonnes performances en milieu aqueux H_2SO_4 et Na_2SO_4. L'électrode $RuO_xN_yS_z$ est une électrode d'oxyde de ruthénium dopé N et S, tandis que l'électrode MnO_2 est une électrode pseudocapacitive bien connue de la famille des oxydes métalliques. Afin de maximiser la capacité de stockage d'énergie, étendre leur fenêtre de potentiel et réaliser des électrolytes solides, nous avons synthétiser des électrolytes appropriés à base de liquide ionique.

Sur la base des caractéristiques de l'électrode, les solvants IL et les sels appropriés contenant les ions porteurs de charge ont été développés de manière rationnelle. L'électrode $RuO_xN_yS_z$ est plus proche de l'électrode RuO_2 en ce sens que les protons H^+ peuvent permettre le transfert de charge, tandis que les solvants contenant des ions Na^+ sont le meilleur choix pour le stockage de la charge dans l'électrode MnO_2.

Liquides ioniques pour micro-supercondensateurs $RuO_xN_yS_z$ poreux solides

Nous avons choisi pour ce type de micro-supercondensateur un solvant liquide ionique aprotique (1-éthyl-3-méthylimidazolium bis(trifluorométhylsulfonyl)imide (EMIM-TFSI)) dopé avec un additif SiWa conducteur de protons pour développer des micro-supercondensateurs $RuO_xN_yS_z$ avec une tension de cellule plus large (figure 14). Alors que les ions H^+ du SiWa peuvent favoriser les réactions d'oxydo-réduction de surface via le transfert d'électrons couplé à un proton, l'EMIM-TFSI permet au processus d'oxydoréduction d'avoir une fenêtre de stabilité plus large.

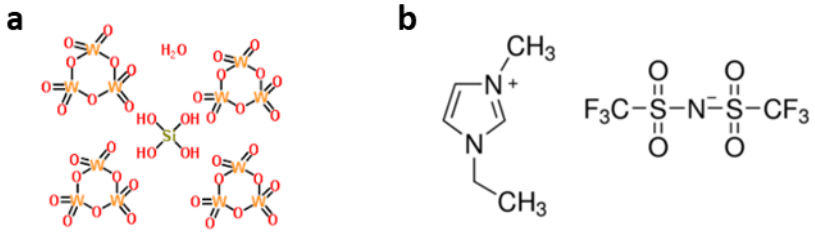

Figure 14. *Structures des groupements cationiques et anioniques des liquides ioniques explorés pour les micro-supercondensateurs $RuO_xN_yS_z$. (a) Sel conducteur de protons, SiWa. (b) Électrolyte liquide ionique.*

En nous basant sur le savoir-faire de de notre équipe, un micro-supercondensateur interdigité à base de matériau d'électrode $RuO_xN_yS_z$ poreux a été préalablement réalisé sur plaquette de silicium (figure 15a). Nous avons étudié le comportement électrochimique du micro-supercondensateur $RuO_xN_yS_z$ en utilisant le liquide ionique [EMIM][TFSI] (1-éthyl-3-méthylimidazolium bis(trifluorométhylsulfonyl)imide) dopé avec du SiWa, et comparer ses performances avec l'électrolyte gelifié à base d'alcool polyvinylique (PVA pour *Poly(Vinyl Alcohol)*) utilisé jusqu'ici.

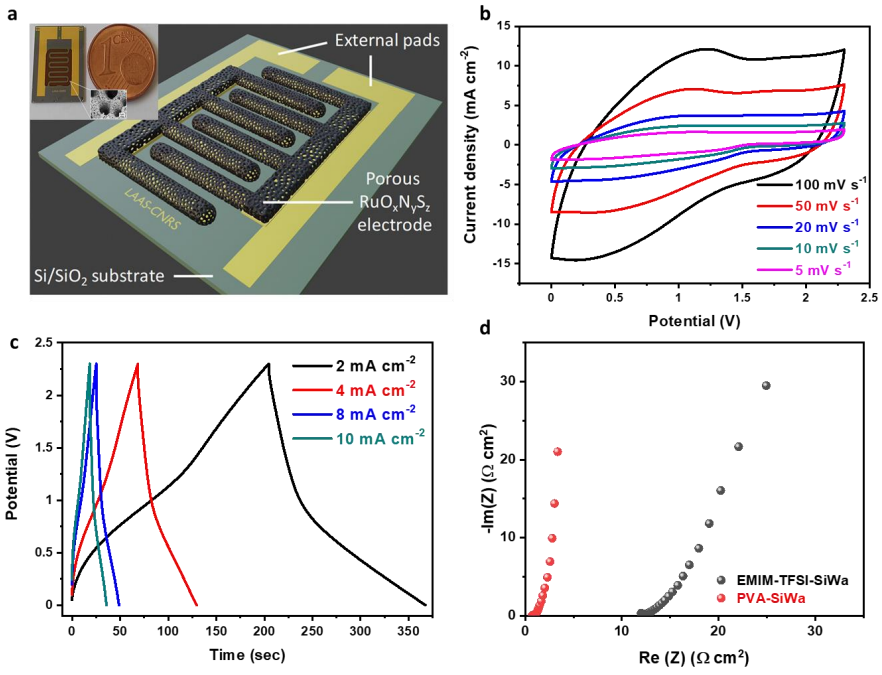

Figure 15. Caractérisations électrochimiques d'un micro-supercondensateur poreux interdigité $RuO_xN_yS_z$ testé avec un électrolyte EMIM-TFSI dopé au SiWa. (a) Schéma et photographie d'un micro-supercondensateur poreux

interdigité avant encapsulation. CV à différentes vitesses de balayage (b) et courbes galvanostatiques à différentes densités de courant (c) testés dans l'électrolyte [EMIM][TFSI] dopé. (d) Diagramme de Nyquist des micro-supercondensateurs poreux interdigités $RuO_xN_yS_z$ basés sur des électrolytes PVA et EMIM-TFSI dopés.

Les courbes de CV à différentes vitesses de balayage pour le micro-supercondensateur poreux interdigité $RuO_xN_yS_z$ testé avec le [EMIM][TFSI] dopé ont révélé une tension de cellule pouvant atteindre 2,3 V (comparé à 1,1 V avec le PVA) sans dégradation visible de l'électrolyte ou de l'électrode (figure 15b). Sur cette fenêtre de tension, les courbes de charge/décharge galvanostatiques à différentes densités de courant présentent la forme triangulaire attendue d'un comportement pseudocapacitif (figure 15c). Sur le diagramme de Nyquist obtenue par spectroscopie d'impédance électrochimique (figure 15d), le micro-supercondensateur poreux interdigité à l'état solide $RuO_xN_yS_z$ avec un électrolyte gélifié à base de PVA présente une résistance série équivalente (ESR) très faible de 0,7 Ω cm^2. Aucun courant de fuite n'est observé, avec une ligne droite presque verticale dans la région des basses fréquences indiquant le caractère pseudocapacitif. La densité d'énergie spécifique atteint une valeur de 432 mJ/cm^2 et une densité de puissance maximale de 421 mW/cm^2. Pour le micro-supercondensateur $RuO_xN_yS_z$ testé avec l'électrolyte EMIM-TFSI dopé au SiWa, l'augmentation de la tension est corrélé à une capacité de cellule plus faible et un ESR plus élevé. Dans ce cas, l'énergie et la densité de puissance atteintes sont respectivement de 460 mJ/cm^2 et 110 mW/cm^2.

Étude électrochimique de micro-supercondensateurs MnO_2 poreux à l'aide d'ILs

Les électrolytes aqueux à base de Na_2SO_4 couramment utilisés pour le MnO_2 limitent la tension de fonctionnement de la cellule en raison de la décomposition de l'eau et de la dissolution partielle de MnO_2 en espèces solubles de MnOOH au-delà d'environ 1 volt. Bien que l'énergie stockée soit directement proportionnelle au carré de la tension de la cellule, le développement d'électrolytes à l'état solide ayant une fenêtre de stabilité électrochimique élargie pour le stockage de charge Na^+ est un défi important. Dans ce travail, nous avons développé et testé quelques électrolytes pour des

micro-supercondensateurs poreux MnO_2 en utilisant des sels de sodium (Na-FSI et Na-TFSI) dilués dans des solvants liquides ioniques aprotiques à base de pyrrolidinium et d'imidazolium (Pyr_{13}-FSI et EMIM-FSI))

Les courbes de CV et d'impédance électrochimiques sont présentées figure 16. Nous n'avons observé aucune différence majeure dans les performances du micro-supercondensateur MnO_2 avec les différents liquides ioniques investigués. Nous pensons donc que, plutôt que le transport ionique de l'électrolyte lui-même, les restrictions semblent être causées par des interactions interfaciales et/ou de transport ionique à l'intérieur du matériau actif. Ces résultats démontrent clairement que les électrolytes liquides ioniques à base de sel de sodium sélectionnés ont le potentiel d'améliorer la densité énergétique des micro-supercondensateurs MnO_2.

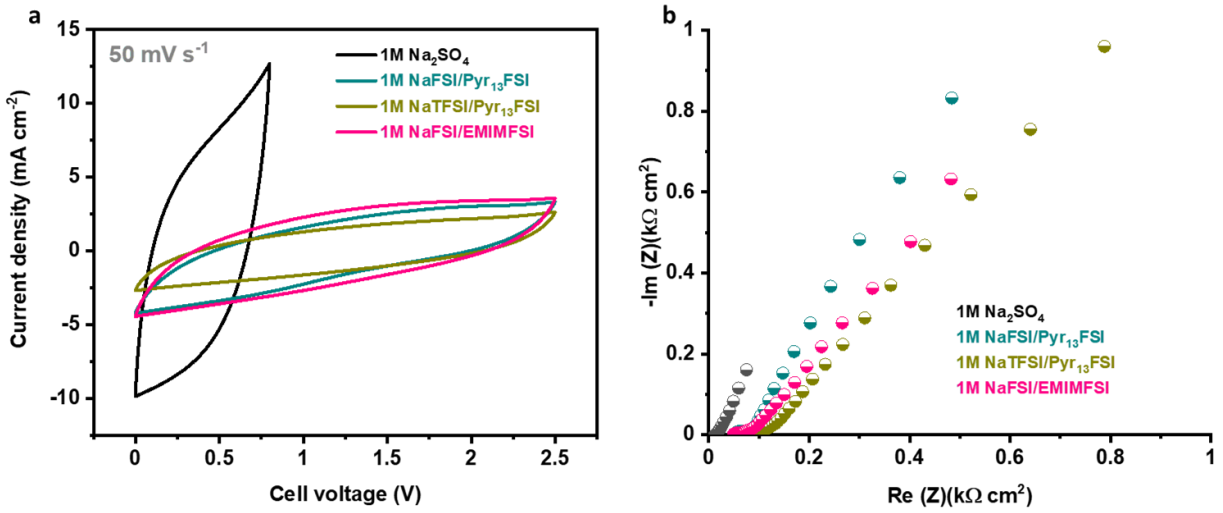

Figure 16. *Performance électrochimique d'un micro-supercondensateur à base de Ni / MnO_2. (a) CV à 50 mV/s testées en milieu 1M Na_2SO_4 et avec des liquides ioniques à base de Na. (b) Diagramme de Nyquist correspondant obtenu de 100 kHz à 10 mHz.*

La figure 17 montre les performances en cyclage de ces micro-supercondensateurs jusqu'à 2000 cycles avec le IL NaFSI/Pyr_{13}FSI comparé avec un électrolyte liquide Na_2SO_4. Avec le NaFSI/Pyr_{13}FSI, une très bonne stabilité est obtenue avec une légère augmentation de capacité attribuée à une lente pénétration de l'électrolyte visqueux dans l'électrode poreuse. Dans

l'ensemble, les performances électrochimiques des micro-supercondensateurs MnO_2 sont prometteuses pour leurs futures applications potentielles.

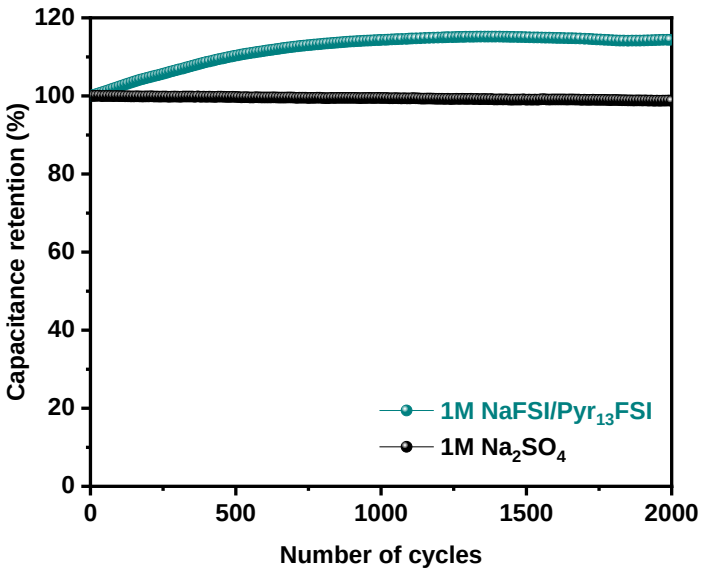

Figure 17. *Stabilité en cyclage (à 2 mA cm^{-2}) des micro-supercondensateurs MnO_2 poreux testés avec 1M Na_2SO_4 et NaFSI /Pyr_{13}FSI.*

Conclusion générale et Perspectives

Nous avons dans cette thèse développé de nouveaux électrolytes liquides ioniques adaptés aux micro-supercondensateurs basés sur des électrodes pseudocapacitives. Les électrolytes liquides ioniques protiques et aprotiques ont été conçus de manière rationnelle sur la base des propriétés des matériaux d'électrodes. La relation structure-propriété des matériaux, y compris les électrolytes, a été méticuleusement étudiée avant de procéder à des caractérisations électrochimiques.

Dans une première partie, nous avons démontré avec succès l'utilisation de divers liquides ioniques protiques comme nouveaux électrolytes pour les micro-supercondensateurs RuO_2. Nous avons sélectionné les cations et les anions des PIL de manière rationnelle en fonction de leurs propriétés physico-chimiques telles que la viscosité, la conductivité, etc. La réaction de transfert d'électrons couplés à des protons contrôlée par la surface est réalisée par le transfert de protons (H^+) à partir

du cation du PIL avec une tension de cellule opérationnelle étendue. Lorsque le PIL est dopée avec du SiWa conducteur de protons, la concentration d'ions H^+ libres augmente, ce qui améliore le stockage de charge pseudocapacitif. Par ailleurs, nous avons obtenu d'excellentes performances en utilisant ces PIL avec des micro-supercondensateurs poreux possédant une grande quantité de matériaux actifs. Ce niveau de performance a pu être transposé aux micro-supercondensateurs à l'état solide à base de gel ionique, révélant l'intégration potentielle des micro-supercondensateurs RuO_2 à base de PIL dans les applications microélectroniques.

Nous avons conclu que les liquides ioniques permettaient, comparés aux électrolytes aqueux traditionnels, d'élargir la fenêtre de stabilité électrochimique tout en permettant un stockage de charge pseudocapacitif de surface dans les électrodes pseudocapacitives de micro-supercondensateurs. Par ailleurs, ces électrolytes liquides ioniques surmontent les inconvénients liés aux électrolytes liquides conventionnels liés à l'encapsulation et les problèmes de fuite lors de leur intégration via les procédés de microfabrication.

Ces liquides ioniques pour micro-supercondensateurs sont ainsi prometteurs pour le microstockage de l'énergie électrique pour des des microsystèmes nécessitant une autonomie énergétique à l'ère de l'Internet des objets.

Perspectives

Grâce à ce travail, nous avons mis au point des micro-supercondensateurs exhibant de très bonnes performances en énergie et en tension en utilisant des matériaux pseudocapacitifs associés à des électrolytes à base de liquide ionique facilitant leur encapsulation (confinement ionique). Parmi les microélectrodes à base d'oxyde métallique à couche mince/épaisse, les liquides ioniques utilisant une architecture 3D confèrent simultanément aux micro-supercondensateurs sur puce une densité d'énergie élevée, une grande densité de puissance et une longue durée de vie. Bien que de

grands progrès ont été réalisées pour obtenir un stockage élevée de l'énergie, de nombreux défis restent encore à aborder. Nous présentons ci-dessous quelques orientations clefs pour l'avenir :

- En ce qui concerne les matériaux d'électrode, il est possible de développer des matériaux avec des performances améliorées pour les micro-supercondensateurs (dopage par hétéroatomes, création de pores, transformation de phase, ingénierie de l'interface etc.) afin d'adapter les propriétés telles que la conductivité électrique, la surface spécifique ou les sites d'oxydo-réduction.

- Bien que de larges fenêtres de stabilité électrochimique ont été atteintes avec nos micro-supercondensateurs, d'autres aspects clefs tels que la plage de température de fonctionnement, la sécurité et le coût doivent être pris en compte afin d'utiliser pleinement leur potentiel pour des futures applications. En ce qui concerne les PIL, il est impératif d'étudier plus avant les propriétés telles que l'ionicité et/ou la super-ionicité pour concevoir des PIL avancées présentant une conductivité élevée et des protons "facilement disponibles" à utiliser efficacement dans le stockage électrochimique de l'énergie, ce qui permettrait un stockage d'énergie rapide et hautement réversible. En outre, la compréhension de l'interaction entre les PIL et l'eau apparaît comme l'une des directions les plus intrigantes en termes d'expansion de la fenêtre de stabilité. L'étude de la possibilité de contrôler et d'accorder la mobilité du proton dans les PIL peut potentiellement aider à réaliser de nouveaux PIL avec une plus grande stabilité électrochimique que les électrolytes aqueux. Les électrolytes à base de gel à l'état solide sont plus favorables aux applications de la microélectronique moderne portable et flexible, mais leur viscosité élevée est un inconvénient qui limite la cinétique du transport des ions. Par conséquent, des efforts supplémentaires devraient être consacrés à une meilleure compréhension des interactions LI-polymère et au développement d'électrolytes à base de gel ionique. En outre, l'ajout d'additifs pour l'électrolyte peut contribuer à

la formation d'une interface solide-électrolyte stable et augmenter la mouillabilité et la stabilité en cyclage.

- Pour les microélectrodes tridimensionneles (3D), une structuration adaptée du collecteur de courant avec des pores ouvertement accessibles et un dépôt conforme du matériau actif amélioreraient les problèmes d'accessibilité aux ions de l'électrolyte et contribueraient à une meilleure utilisation du matériau actif. La structure suffisamment poreuse peut s'adapter à tout changement de volume au cours du processus de charge/décharge, prolongeant ainsi la durée de vie des micro-supercondensateurs 3D. Par ailleurs, des outils de caractérisation théoriques et expérimentaux de pointe permettraient d'étudier comment la taille, la distribution et l'épaisseur de la paroi des pores affectent le comportement du transport des ions et du stockage des charges dans les microélectrodes poreuses. En combinant les techniques d'analyse in situ avec les caractérisations spectroscopiques operando, il serait possible de visualiser en temps réel les processus électrochimiques et comprendre l'évolution de la morphologie, de la structure et des composants au cours du processus de charge/décharge. Ceci, combiné à des études de modélisation théorique, permettrait sans aucun doute d'obtenir de nouvelles informations sur les mécanismes de stockage de charge sous-jacents.

En résumé, des technologies de microfabrication avancées, une conception optimale de l'architecture des électrodes, et le développement de matériaux actifs et d'électrolytes innovants seraient nécessaires pour réaliser des micro-supercondensateurs 3D ayant une fote densité d'énergie et de puissance, ainsi qu'une longue durée de vie. En outre, la recherche de solutions rentables pour réaliser cette technologie avec une meilleure encapsulation des dispositifs contribuerait à l'augmentation de la production de micro-supercondensateurs sur puce et à l'avancement de la technologie IoT.